

# Magnetic-field-induced Antiferromagnetism in the Kondo Lattice

by

Kevin Stuart David Beach

B.Sc.H. Theoretical Physics, 1997

M.Sc. Physics, 1999

Queen's University at Kingston

Submitted to the Department of Physics  
in partial fulfillment of the requirements for the degree of

Doctor of Philosophy in Physics

at the

MASSACHUSETTS INSTITUTE OF TECHNOLOGY

[Solemnly 2004]  
August 2004

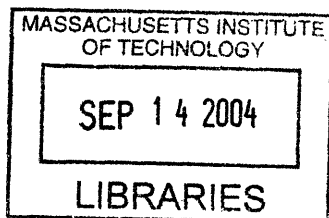
© Kevin Stuart David Beach, MMIV. All rights reserved.

The author hereby grants to MIT permission to reproduce and  
distribute publicly paper and electronic copies of this thesis document  
in whole or in part.

Author .....  
Department of Physics  
August 6, 2004

Certified by .....  
Professor Patrick A. Lee  
William & Emma Rogers Professor  
Thesis Supervisor

Accepted by .....  
Professor Thomas J. Greytak  
Associate Department Head for Education



ARCHIVES



**Magnetic-field-induced  
Antiferromagnetism in the  
Kondo Lattice**

by  
Kevin Stuart David Beach

Submitted to the Department of Physics  
on August 6, 2004, in partial fulfillment of the  
requirements for the degree of  
Doctor of Philosophy in Physics

**Abstract**

The half-filled Kondo lattice model, augmented by a Zeeman term, serves as a useful model of a Kondo insulator in an applied magnetic field. A variational mean field analysis of this system on a square lattice, backed up by quantum Monte Carlo calculations, reveals an interesting separation of magnetic field scales. For Zeeman energy comparable to the Kondo energy, the spin gap closes and the system develops transverse staggered magnetic order. The charge gap, however, remains robust up to a higher hybridization energy scale, at which point the canted antiferromagnetism is exponentially suppressed and the system crosses over to a nearly-metallic regime.

The quantum Monte Carlo simulations are performed using a determinant Monte Carlo method that has been extended to handle mixed spin and fermionic degrees of freedom. The formulation is sign-problem-free for all values of the Kondo coupling and magnetic field strength. The matrix operations are specially organized to maintain numerical stability down to arbitrarily low temperatures.

Spectral data is extracted from the imaginary-time correlation functions using an improved analytic continuation technique. The weak, secondary peaks of the single-electron spectral function are resolvable, and their response to the magnetic field is carefully tracked. An unusual rearrangement of spectral weight is found at the onset of the antiferromagnetism.

Thesis Supervisor: Professor Patrick A. Lee  
Title: William & Emma Rogers Professor



## Acknowledgements

Graduate school is an accomplishment that can't easily go to one's head. Even the most brash, cocksure young student quickly comes to realize how limited his own knowledge and abilities are—and to recognize that whatever success comes his way is due in no small part to his colleagues and peers. Physics at MIT breeds humility. In that spirit, for whatever success I've had, let me thank all those who've had a hand in it.

First and foremost, I must thank my supervisor, Patrick Lee, who has only ever shown me generosity and goodwill, and who has suffered patiently through five years of me and my many missteps and dead ends. In that time, I've had the good fortune to benefit from his guidance and insight and to see first-hand his world-famous “physical intuition,” of which I'd heard spoken long before I came to MIT. Patrick, you see, has the uncanny ability to discern, on a few minutes' reflection, the answer to any physical problem he's given. There was rarely a time when I could not resolve weeks of speculation, indecision, and confusion with a short visit to his office.

I also owe an enormous debt of gratitude to Philippe Monthoux, who taught me everything I know about quantum Monte Carlo. A doubly enormous debt, in fact, because most computational physicists, like magicians, swear an oath never to reveal their tricks. This project would have been impossible without his help. I would also like to acknowledge Anders Sandvik, who was an enthusiastic early supporter of my analytic continuation work and who had the good judgement to hire me as a postdoc.

Let me express my appreciation to the members of my thesis committee, Patrick, John Negele, and Senthil, for their advice and support and for giving so freely of their time. As the only three people who will likely ever read this document in full, they deserve my overflowing, unstinting, exalting praise. In the category of good-natured, jovial geniuses, I give a tip of the hat to John Joannopoulos, Xiao-Gang Wen, and Senthil, who taught some of the best classes at MIT and who laughed loudest and freest. I also give heartfelt thanks to my Master's supervisor, Robert Gooding, who has continued to keep tabs on me and to offer his advice and encouragement.

Lest you think I've unduly emphasized mentorship over camaraderie, let me salute my officemates, current and former: Bernd Braunecker, Walter Hofstetter, Ashvin Vishwanath, Carsten Honer camp, Jun-ichiro Kishine, Adam Durst, my long-time officemate and consigliere, who deserves special thanks for getting me through those first three years, . . . and in the distant mists of time, Catherine Pépin, who had my desk before me and who, in the French spirit of *Fraternité*, left it fully stocked with liquor. On that note, let me also raise a glass of Catherine's best bourbon to my fellow graduate students, Sami Amasha, J.T. Shen, Michelle Povinelli, Alexander Seidel, Tiago Ribeiro, and Walter Rantner, and especially to my friends Ghislain Granger and K.C. Huang, who, having gone up the ranks with me, occupy a special place in the pantheon.

Most important, I'd like to thank my caring family for their unconditional support and Sarah Ligon, my friend, partner, and love, for being with me joyfully through it all.



# Contents

<b>1</b>	<b>Introduction</b>	<b>9</b>
1.1	Background . . . . .	9
1.2	Physical Model . . . . .	11
1.3	Motivation and Objectives . . . . .	13
1.4	Organization . . . . .	15
<b>2</b>	<b>Hybridization Mean Field</b>	<b>17</b>
2.1	Outline . . . . .	17
2.2	Mean Field Formalism . . . . .	18
2.2.1	Hybridization Field . . . . .	18
2.2.2	Quasiparticle Dispersion Relation . . . . .	19
2.2.3	Spectral Properties . . . . .	20
2.2.4	Fixing the Mean Field Parameters . . . . .	22
2.3	Thermodynamic Limit . . . . .	23
2.4	Heavy Fermion Metal . . . . .	26
2.4.1	Characterizing the Ground State . . . . .	26
2.4.2	Detailed Mean Field Solution . . . . .	27
2.5	Kondo Insulator . . . . .	29
2.5.1	Zero-field Ground State . . . . .	29
2.5.2	Field-induced Metal-insulator Transition . . . . .	30
<b>3</b>	<b>RKKY Antiferromagnetism</b>	<b>33</b>
3.1	Outline . . . . .	33
3.2	Effective Kondo and RKKY Couplings . . . . .	35
3.3	What Physics Wins Out Where . . . . .	38
3.4	Spin Wave Theory . . . . .	40
<b>4</b>	<b>Numerical Results</b>	<b>45</b>
4.1	Outline . . . . .	45
4.2	Variational Mean Field . . . . .	46
4.3	Quantum Monte Carlo . . . . .	49
<b>5</b>	<b>Constrained Quantum Monte Carlo</b>	<b>57</b>
5.1	Outline . . . . .	57
5.2	Formulation of the Constrained Action . . . . .	58

5.3	Monte Carlo Sampling . . . . .	61
5.3.1	Generating the Markov Chain . . . . .	61
5.3.2	Update Scheme . . . . .	63
5.3.3	Accounting for Autocorrelation Effects . . . . .	65
5.4	Computing Physical Observables . . . . .	66
5.5	Numerical Stabilization . . . . .	69
5.6	Kondo Lattice Model . . . . .	72
<b>6</b>	<b>Stochastic Analytic Continuation</b>	<b>77</b>
6.1	Outline . . . . .	77
6.2	Analytic Continuation . . . . .	78
6.3	Maximum Entropy Method . . . . .	80
6.4	The Stochastic Approach . . . . .	81
6.5	Approximate Solutions . . . . .	83
6.6	Monte Carlo Evaluation . . . . .	84
6.6.1	Configurations and Update Scheme . . . . .	84
6.6.2	Parallel Tempering . . . . .	87
6.7	Critical Temperature . . . . .	88
6.8	BCS Test Case . . . . .	90
6.9	Summary . . . . .	91
<b>7</b>	<b>Conclusions</b>	<b>93</b>
<b>A</b>	<b>Appendices</b>	<b>95</b>
A.1	Effective Spin Hamiltonian . . . . .	95
A.2	Hubbard-Stratonovich Transformation . . . . .	98
A.3	Coherent State Representation of Operators . . . . .	99
A.4	Even-occupation Constraint Field . . . . .	101
A.5	Continuous-time Limit of the Action . . . . .	101
A.6	Statistical Error and Discretization . . . . .	102
A.7	Maximum Entropy Formal Solution . . . . .	104
A.8	Configurational Entropy . . . . .	105
A.9	Discretization over a Logarithmic Mesh . . . . .	106

# Chapter 1

## Introduction

### 1.1 Background

There are many physical systems in which localized quantum spins and itinerant electrons coexist. These include simple metals doped with magnetic ions (*e.g.*, Fe impurities in Cu); bulk intermetallic compounds containing unpaired electrons in inner shells (*e.g.*, UPt<sub>3</sub>); and odd-populated quantum dots coupled to conduction leads. In cases where the interaction between the local and itinerant magnetic moments favours singlet pairing, the so-called *Kondo effect* dominates: below the characteristic Kondo temperature  $T_K$ , a complicated many-body state emerges in which the local moments are completely or partially compensated. The transport and thermodynamic properties of such systems are often marked by low-temperature anomalies.

The classic Kondo problem is that of a small concentration of magnetic impurities embedded in a normal metal. At high temperatures, the impurities and electrons interact only weakly, and the impurity spins behave as isolated local moments. This is evident from spin susceptibility measurements, which reveal—superimposed over the Pauli susceptibility of the host metal—a Curie-Weiss response proportional to the doping concentration. Below  $T_K$ , however, the contribution from the local moments is radically suppressed. The mechanism at work is the formation of virtual bound states in which the electrons are almost localized by resonant scattering at the impurity sites. The electrons in the vicinity of each impurity form a cloud that screens the local moment.

The earliest evidence of unusual behaviour in impurity-doped metals was the observation that, as these materials are cooled, their electrical resistance eventually bottoms out and begins to increase—unlike normal metals, whose resistance decreases monotonically. Kondo's explanation [1] of the resistance minimum in 1964 was a major triumph and set the stage for the theoretical developments that followed. Starting from a model of a single  $S = 1/2$  spin interacting with a conduction band via exchange, Kondo computed the resistance to third order in the interaction strength  $J$ . He found that singular scattering of the conduction electrons near the Fermi level produces a  $\ln T$

contribution. This, combined with the usual contribution from phonons, could account for the experimental observations around the minimum.

It was clear, however, that Kondo's result was not valid down to zero temperature, where it diverged. A full understanding of the low-temperature regime would have to await the development of scaling [2] and renormalization group [3] ideas. It came to be understood that Kondo's perturbation theory failed because the temperature range  $T \ll T_K$  amounts to a strong-coupling limit in which  $J$  is renormalized to large values. In the Kondo ground state ( $J \rightarrow \infty$ ), each impurity spin binds with a conduction electron to form a singlet. The low-energy behaviour of the system is governed by the residual interactions that arise from virtual singlet-breaking transitions. The spectral signature for this effect is the formation of a very narrow many-body resonance at the Fermi level, which makes an anomalous power-law contribution to many physical properties. This general picture was confirmed in 1980, when Andrei and Wiegman discovered a Bethe Ansatz solution to the single-impurity Kondo model [4, 5].

The ongoing challenge is to understand Kondo physics beyond the dilute limit. There is currently a great deal of interest in so-called *Kondo lattices*—typically intermetallic compounds of Ce or U. These belong to a generation of materials that first appeared in the 1970s in which transition-metal or rare-earth ions interact with conduction electrons at many sites in an alloy or regular array. Kondo lattices represent the concentrated limit of the Kondo problem. The number of local moments is comparable to the number of conduction electrons, and there are simply not enough electrons to screen all the moments in a single-impurity-like way [6]. Moreover, the local moments are packed densely enough that each one lives in a local electronic environment heavily influenced by its neighbours. This raises the possibility of collective magnetic ordering.

From the single-impurity problem, we know that electrons up to a distance  $l \sim v_F/k_B T_K$  away from the impurity site participate in the screening. In the dilute Kondo problem, where the distance between local moments is considerably larger than  $l$ , it is appropriate to treat the local moments as mutually independent. For periodic systems, however, the distance between local moments is on the order of the lattice spacing. In this case, the screening clouds overlap significantly, and the indirect Ruderman-Kittel-Kasuya-Yosida (RKKY) interaction [7, 8, 9] induced between the local moments must be accounted for.

The competition between Kondo singlet formation and RKKY magnetism determines the ground state of a Kondo lattice compound. The outcome depends sensitively on the detailed structure of the material and on its chemical composition. For example,  $\text{CeAl}_3$  ( $\text{Ce}^{3+}$  configuration,  $\text{Ni}_3\text{Sn}$ -type hexagonal close-packed structure) remains paramagnetic down to low temperatures, whereas  $\text{CeAl}_2$  ( $\text{Ce}^{3+}$  configuration,  $\text{Cu}_2\text{Mg}$ -type cubic Laves structure) develops antiferromagnetic order. Because of the oscillatory nature of the RKKY interaction, various kinds of magnetism can be realized.

NpBe<sub>13</sub>, U<sub>2</sub>Zn<sub>17</sub>, UCd<sub>11</sub>, and NpSn<sub>3</sub> are antiferromagnets. CeSi<sub>x</sub> ( $x < 1.85$ ), CeCu<sub>2</sub>, and CeRu<sub>2</sub>Ge<sub>2</sub> are ferromagnets. Some systems with structural disorder, such as CeRuGe<sub>3</sub> and U<sub>2</sub>PdSi<sub>3</sub>, exhibit spin glass behaviour.

When the Kondo effect overpowers the inter-site interactions, the resulting ground state is nonmagnetic. Of the materials in this class, many do not conduct at all. These are referred to as *Kondo insulators*. Examples include CeNiSn, CePdSn, CePdGa, and Ce<sub>3</sub>Bi<sub>4</sub>Pt<sub>3</sub>. Others, such as CeAl<sub>3</sub> and CeCu<sub>6</sub>, are metallic and go by the name *heavy fermions*. The origin of the insulating behaviour is the tendency of the conduction electrons to bind in singlet pairs with the core electrons. Like Mott insulators, Kondo insulators are materials that should—according to traditional band theory—have a half-filled metallic band. Instead, the strong interactions localize the conduction electrons and open up a gap at the chemical potential. The heavy fermion materials, on the other hand, have low-temperature properties consistent with Fermi-liquid theory [10, 11], but have effective masses two to three orders of magnitude larger than the bare-electron mass.

Heavy fermion physics is markedly different from the familiar Kondo effect of the dilute limit. As the temperature drops below  $T_K$ , the local moments are compensated, and their magnetic degrees of freedom are gradually incorporated into the itinerant states. These new states are coherent across the system and respect the translational invariance of the lattice (in contrast with the symmetry-breaking screening states of the dilute limit). As a result of the participation of the core electrons in forming the heavy quasiparticles, the system develops an enlarged Fermi sea that includes both the conduction and core electrons. Strong renormalization of the bands at the Fermi surface is responsible for the unusually large effective mass.

## 1.2 Physical Model

As depicted in Fig. 1-1, the basic physics of the Kondo lattice materials is that of valence electrons in extended orbitals and strongly correlated core electrons in localized orbitals. Outer-shell  $s$ ,  $p$ , or  $d$  electrons are released from their host ions into the bulk and move through the lattice in a broad conduction band. Inner-shell  $f$  electrons retain their ionic character and remain bound.

The canonical description of such systems is the periodic Anderson model (PAM) [12]. The model treats the conduction electrons in the tight-binding approximation and allows for transitions between the core levels and the conduction band; electrons localized in the core levels are subject to a strong onsite Coulomb repulsion. The Hamiltonian has the form

$$\begin{aligned} \hat{H}_{\text{PAM}} = & -t \sum_{\langle ij \rangle} (c_i^\dagger c_j + c_j^\dagger c_i) + \sum_i \left[ \epsilon_f f_i^\dagger f_i + U (f_i^\dagger f_i - 1)^2 \right] \\ & + \sum_i (V^* f_i^\dagger c_i + V c_i^\dagger f_i). \end{aligned} \quad (1.1)$$

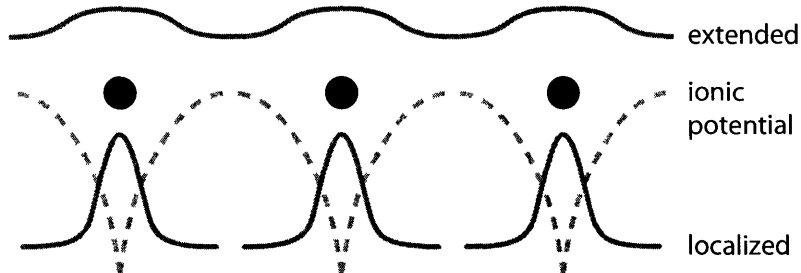


Figure 1-1: Kondo lattice materials are rare-earth crystals containing both mobile electrons in extended orbitals and tightly bound electrons in localized orbitals.

Here,  $c^\dagger$  ( $c$ ) is the creation (annihilation) operator for the conduction electrons;  $f^\dagger$  ( $f$ ) plays the analogous role for the core electrons.  $t$  is the hopping integral between nearest neighbour lattice sites,  $\epsilon_f$  is the binding energy of an electron in a core level, and  $U$  is the strength of the Coulomb repulsion.

The parameter values  $|V| \ll t \ll U$  and  $|\epsilon_f| \ll U$  are appropriate to the Kondo lattice materials. In this regime, the  $c$  and  $f$  electrons hybridize only weakly, and the Coulomb repulsion is the largest energy scale in the problem. Most important, the  $f$  levels are populated with one electron per site. Since charge fluctuations are heavily suppressed by the large  $U$ , these unpaired core electrons behave as localized magnetic moments.

In the extreme Coulomb limit  $U \rightarrow \infty$ , the suppression of the charge fluctuations is total, and the core electrons can be mapped onto pure  $S = 1/2$  quantum spins. As shown by Schrieffer and Wolf [13], virtual excitations of the core electrons into the conduction band induce an antiferromagnetic exchange interaction of strength  $J \sim |V|^2/U$ . The resulting Hamiltonian

$$\hat{H}_{\text{KLM}} = -t \sum_{\langle ij \rangle} (c_i^\dagger c_j + c_j^\dagger c_i) + J \sum_i \frac{1}{2} c_i^\dagger \boldsymbol{\sigma} c_i \cdot \hat{S}_i \quad (1.2)$$

describes a periodic arrangement of quantum spins  $\hat{S}_i$  immersed in a conduction sea. This so-called *Kondo lattice model* (KLM), shown schematically in Fig. 1-2, is the lattice generalization of Kondo's original single-impurity model.

When the conduction band of the KLM is half-filled, there are equal numbers of electrons and spins. The strong-coupling ground state consists of a singlet pair localized at each site; excitations involve breaking one of the singlets at finite energy cost. This spin- and charge-gapped state is a Kondo insulator. In the weak coupling limit, however, the conduction electrons mediate an effective interaction between the spins that causes them to order magnetically. In general, local singlet formation dominates whenever the

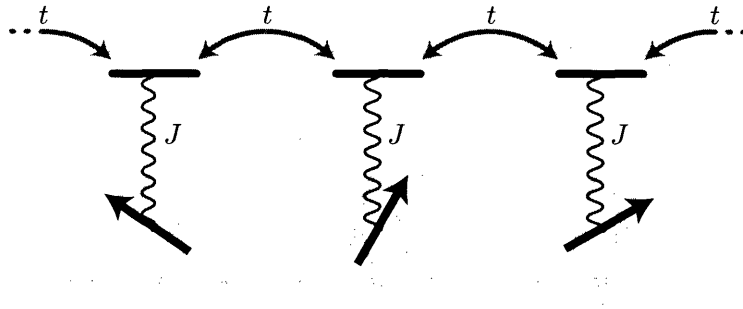


Figure 1-2: In the Kondo lattice model, conduction electrons hop from site to site with amplitude  $t$ . The localized magnetic moments in the core states function as pure quantum spins. An onsite exchange interaction of strength  $J$  couples the spin and electronic degrees of freedom.

Kondo coupling exceeds some critical value  $J_c$ , and RKKY magnetism wins out otherwise. The nature of the magnetic order depends on the structure of the lattice and the shape of the Fermi surface. On a square or cubic lattice, the RKKY interaction is antiferromagnetic.

Away from half-filling, the  $J > J_c$  KLM describes a heavy metal. The additional electrons or holes introduced into the system—dressed by their interaction with the strongly-correlated electronic background—propagate freely. Their motion is considerably more sluggish than that of a bare electron because it entails a disruption to the local environment through the repeated breaking and reforming of singlet pairs.

### 1.3 Motivation and Objectives

Enthusiasm for Kondo lattice physics waned significantly in the mid-1980s. The basic physical picture was believed to be well understood, and it was not clear that there was much new to measure or explain. Moreover, the discovery of high-temperature superconductivity in the cuprates had presented the condensed matter community with an exciting and important new problem to pursue. In recent years, however, there has been a resurgence of interest in Kondo phenomena, especially in connection with quantum phase transitions.

Our traditional understanding of phase transitions, even in quantum mechanical systems, is essentially classical: fluctuations in some low temperature ordered phase are enhanced with heating and eventually become critical at some temperature  $T_c$ . In the disordered phase above  $T_c$ , thermal randomization restores the symmetry that is broken at low temperatures. Some materials, however, can be made to pass from one phase to another at zero temperature by applying chemical or hydrostatic pressure

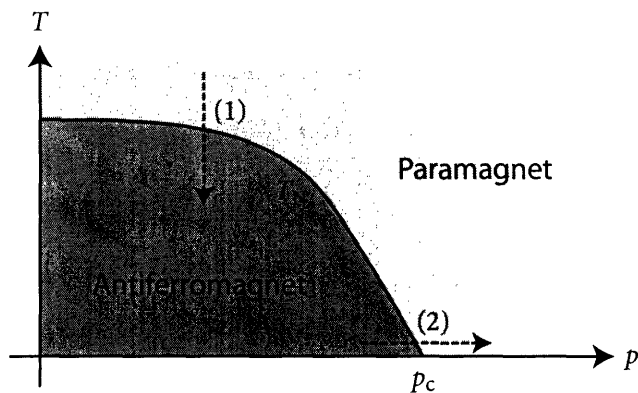


Figure 1-3: The numbered paths indicate (1) a transition to the antiferromagnetic state by cooling and (2) a transition to the paramagnetic state by application of pressure. Path (1) constitutes a thermal phase transition (at  $T = T_N$ ,  $p < p_c$ ), and path (2) a quantum phase transition (at  $p = p_c$ ,  $T = 0$ ).

or an external magnetic field. There is now a growing appreciation for the sometimes dramatic effect these so-called quantum phase transitions have on low-temperature properties in the vicinity of the quantum critical point.

Many Kondo lattices are prized for their proximity to a magnetically ordered phase. A typical example is the heavy fermion material  $\text{CeCu}_6$ . Alloying this material with Au causes the lattice to expand. Unlike its parent compound, which is nonmagnetic,  $\text{CeCu}_{6-x}\text{Au}_x$  exhibits antiferromagnetic order above a critical concentration  $x_c \approx 0.1$ . The antiferromagnetism can be banished by recompressing the lattice. Bogenberger and Löhneysen have shown that the Néel temperature of  $\text{CeCu}_{5.7}\text{Au}_{0.3}$  can be continuously tuned to zero with increasing hydrostatic pressure [14]. At the critical value of the pressure, a  $T = 0$  quantum critical point separates the magnetic and nonmagnetic ground states. See Fig. 1-3.

In the case of Kondo insulators, which will be the focus of this thesis, one of the interesting possibilities is a field-driven transition to a metallic state. For example, transport measurements of  $\text{Ce}_3\text{Bi}_4\text{Pt}_3$  in high magnetic fields [15, 16] indicate that its resistivity plummets to a low, impurity-dominated value at a critical field on the order of 50 T. The data are consistent with a transition from an insulator to a dirty metal. Nonetheless, the detailed evolution of the charge gap with applied field and the nature of the quantum insulator-to-metal transition are not yet understood.

There are likely two mechanisms at work here. First, the magnetic field tends to suppress singlet formation and thus works against the Kondo effect. Second, the field lifts the degeneracy of the spin up and spin down bands, shifting them with respect to one another. Both of these effects should help

to drive the system metallic—although which effect predominates and what role the competing magnetic order plays are open questions.

How might magnetism complicate matters? Recall that in zero field a critical value of the Kondo coupling  $J_c$  separates the antiferromagnetic and Kondo singlet phases. A magnetic field will bias the competition between them and shift the phase boundary—presumably toward higher  $J$ . As the critical point evolves with magnetic field, it traces out a line of transitions that impinges on the Kondo side of the phase diagram. This line marks the critical value of the field strength at which the spin gap closes and staggered order (perpendicular to the field direction) sets in. Thus, by weakening the Kondo effect, the applied field may end up stabilizing a  $J > J_c$  canted antiferromagnetic phase.

If this picture is correct, the closing of the spin and charge gaps cannot coincide: the canted antiferromagnetic state is itself insulating, so the onset of metallicity must be postponed to still higher fields. The extent of the intervening antiferromagnetic phase determines what sort of metal—heavy or normal—is eventually obtained. If the antiferromagnetic phase is small, the heavy quasiparticles may persist all the way into the metallic phase. Otherwise, the metal is well-separated from the Kondo insulator and likely to be normal.

**The goal of this thesis is to investigate the effect of an applied magnetic field on the Kondo insulator ground state and to clarify the role of antiferromagnetism in the Kondo-insulator-to-metal transition.**

## 1.4 Organization

The appropriate model for a Kondo insulator in an applied magnetic field is the half-filled KLM, augmented by a Zeeman term of the form

$$\hat{H}_B = -\mathbf{B} \cdot \sum_i \left( \frac{1}{2} c_i^\dagger \boldsymbol{\sigma} c_i + \hat{\mathbf{S}}_i \right). \quad (1.3)$$

We investigate this model on the square lattice using a variety of analytical and numerical techniques and develop a consistent picture of its behaviour as a function of the field strength  $B$ .

In Chapters 2 and 3, we present some simple analytical calculations. The hybridization mean field theory—the standard framework for describing the Kondo insulator and heavy fermion states—predicts that the Kondo insulator turns directly into a normal metal when the energy scale of the applied field is comparable to the Kondo energy. The transition is first order and marked by the sudden disappearance of the Kondo effect at the critical field. This naive result does not survive the inclusion of RKKY magnetism. A diagrammatic analysis suggests that, in response to the applied field, the

Kondo insulator first gives way to a canted antiferromagnetic state. The emergence of the antiferromagnetism can be understood as an instability of the transverse spin wave excitations above the singlet ground state.

Chapter 4, based on Ref. [17], is a relatively self-contained exposition of our important numerical results. The starting point is a variational mean field treatment of the KLM that is designed to address the competition between the Kondo singlet formation and RKKY magnetism. According to this calculation, the Kondo insulator state responds to small applied fields in a trivial way: its bands are spin split by  $|B|$  and thus its charge gap decreases linearly with the field. At intermediate field strength, just before the charge gap vanishes completely, the system undergoes a continuous transition to a canted antiferromagnetic state. The charge gap increases in step with the growing staggered moment. Over a small range above this critical field, magnetism coexists with the Kondo effect. The composite heavy quasiparticles have not yet disintegrated. They are still bound in singlet-like pairs with the  $c$  and  $f$  electrons canting in opposite directions. As the field strength increases, the Kondo effect disappears, the  $c$  and  $f$  electrons begin to cant in the same direction, and the staggered order slowly dies out. The vanishing of the staggered moment coincides with the closing of the charge gap. We use the quantum Monte Carlo simulations to confirm this mean field scenario.

The next two chapters describe in detail the numerical methods we used to generate and interpret the quantum Monte Carlo data. In Chapter 5, we explain how the determinant quantum Monte Carlo method—a standard lattice fermion algorithm—can be extended to treat the KLM, which contains both spin and fermion degrees of freedom. We present a numerical stabilization scheme that keeps the simulation well-behaved at arbitrarily low temperatures. We show that, by exploiting the particle-hole symmetry of the half-filled KLM and the bipartite nature of the square lattice, the simulation can be formulated in such a way as to be free of the fermion sign problem for all values of the Kondo coupling and magnetic field.

In Chapter 6, we present a non-standard stochastic method for extracting spectral functions from noisy quantum Monte Carlo data. We relate the spectral extraction problem to a system of interacting classical fields whose Hamiltonian is chosen such that the determination of its ground state field configuration corresponds to an unregularized inversion of the input data. The regularization is effected by performing a thermal average over the field configurations at a small fictitious temperature using Monte Carlo sampling. We prove that this method is a natural dynamical generalization of the maximum entropy method, the currently accepted state of the art.

## Chapter 2

# Hybridization Mean Field

### 2.1 Outline

The KLM is thought to provide an approximate description of the heavy fermion and Kondo insulator materials. It describes a band of free conduction electrons moving in a periodic array of magnetic impurities  $\hat{S}_i$ . The only interaction is the onsite Heisenberg exchange between the electron spin density and the magnetic moment of the impurities. The model can be extended to include a Zeeman term, which consists of a magnetic field  $\mathbf{B}$  coupled to the total magnetic moment at each site:

$$\hat{H} = -t \sum_{\langle ij \rangle} (c_i^\dagger c_j + c_j^\dagger c_i) + J \sum_i \frac{1}{2} c_i^\dagger \boldsymbol{\sigma} c_i \cdot \hat{S}_i - \mathbf{B} \cdot \sum_i (\frac{1}{2} c_i^\dagger \boldsymbol{\sigma} c_i + \hat{S}_i). \quad (2.1)$$

Here,  $t$  and  $J$  are the hopping and exchange integrals, respectively, and  $c^\dagger$  ( $c$ ) is the creation (annihilation) operator for the conduction electrons; the impurity spins are  $S = 1/2$ .

When the Kondo lattice is populated with exactly one electron per site, the system develops a gap in its excitation spectrum and ceases to conduct. The magnitude of this gap is equal to the Kondo energy  $2\Delta_K$ . Away from half-filling, the system is a Fermi liquid with an usually large effective mass. In this chapter, we describe the Kondo insulator and heavy fermion ground states at the mean field level and investigate how the Kondo insulator reacts to an applied magnetic field.

Our approach is to construct a mean-field Hamiltonian by decomposing the exchange interaction in the hybridization channel [18]. When the hybridization order parameter condenses, mixing between the local and itinerant degrees of freedom causes the conduction band to break into upper and lower quasiparticle bands. The properties of the heavy fermion materials can be understood in terms of the very shallow dispersion near the hybridization gap edge. The Kondo insulator, on the other hand, corresponds to the situation in which the lower band is completely filled. In that case, both the charge and spin excitations are cut off by the hybridization gap.

The Kondo insulator state is continuously connected to the  $J = \infty$  ground state in which a conduction electron and a local spin are bound together in a singlet pair at each site. Within the hybridization mean field picture, a small magnetic field has no effect on the Kondo insulator other than to Zeeman split its spin up and spin down bands. When the field is large enough to break the singlet pairs, the system makes a first order transition to a normal metallic state in which the local spins are polarized along the direction of the field.

## 2.2 Mean Field Formalism

### 2.2.1 Hybridization Field

A useful formal trick is to represent the local spins in terms of fermions, which puts the local and itinerant degrees of freedom on the same footing. Specifically, we take  $\hat{S} = \frac{1}{2}f^\dagger\sigma f$  subject to the constraint  $f^\dagger f = 1$ . Here,  $f^\dagger$  ( $f$ ) is the creation (annihilation) operator of a fictitious, dispersionless  $f$  band. The constraint suppresses all  $f$ -charge fluctuations and has the effect of projecting out the singlet states that are not a part of the Hilbert space of the original SU(2) spin. We shall assume that it is sufficient to enforce the constraint on average and require only that  $\langle f^\dagger f \rangle = 1$ .

The operators  $\hat{\chi}^\mu = \frac{1}{\sqrt{2}}f^\dagger\sigma^\mu c$ , defined in terms of the unit and Pauli matrices  $\sigma^\mu = (\mathbf{1}, \boldsymbol{\sigma})$ , describe the spin degrees of freedom at each site. They can be used to express the exchange term in the Hamiltonian as

$$\frac{1}{4}c^\dagger\boldsymbol{\sigma}c \cdot f^\dagger\boldsymbol{\sigma}f = -\frac{3}{4}\hat{\chi}^{0\dagger}\hat{\chi}^0 + \frac{1}{4}\hat{\boldsymbol{\chi}}^\dagger \cdot \hat{\boldsymbol{\chi}}. \quad (2.2)$$

$\hat{\chi}^0$  and  $\hat{\boldsymbol{\chi}}$  act in the singlet and triplet channels, respectively. In the heavy fermion state, the singlet amplitude condenses  $\langle \hat{\chi}^0 \rangle \neq 0$ , leading to hybridization of the  $c$  and  $f$  bands. Neglecting second order fluctuations about the mean hybridization field gives

$$\hat{\chi}^{0\dagger}\hat{\chi}^0 = \langle \hat{\chi}^0 \rangle^* \hat{\chi}^0 + \hat{\chi}^{0\dagger} \langle \hat{\chi}^0 \rangle - |\langle \hat{\chi}^0 \rangle|^2, \quad (2.3)$$

from which follows—combining Eqs. (2.1), (2.2), and (2.3)—the mean field Hamiltonian

$$\begin{aligned} \hat{H}_{\text{MF}} = & -t \sum_{\langle ij \rangle} (c_i^\dagger c_j + c_j^\dagger c_i) - \sum_i (V_i^* f_i^\dagger c_i + V_i c_i^\dagger f_i) + \frac{8}{3J} \sum_i |V_i|^2 \\ & - \frac{B}{2} \cdot \sum_i (c_i^\dagger \boldsymbol{\sigma} c_i + f_i^\dagger \boldsymbol{\sigma} f_i) - \mu_c \sum_i c_i^\dagger c_i - \mu_f \sum_i f_i^\dagger f_i. \end{aligned} \quad (2.4)$$

We have expressed the Hamiltonian in terms of a hybridization field

$$V = \frac{3J}{4\sqrt{2}}\langle \hat{\chi}^0 \rangle = \frac{3J}{8}\langle f^\dagger c \rangle \quad (2.5)$$

having units of energy. We have also included two chemical potentials  $\mu_c$  and  $\mu_f$  that couple to the  $c$ - and  $f$ -electron densities. These allow us to control the conduction band filling and the  $f$ -level occupancy.

### 2.2.2 Quasiparticle Dispersion Relation

The minimum-energy hybridization field configuration is translationally invariant. Thus, we can write  $V_i = V = |V|e^{i\theta}$ . Moreover, although the hybridization  $\langle f^\dagger c \rangle$  is in general complex, we may safely take  $V$  to be real and positive. There is a U(1) gauge freedom associated with the invariance of  $\hat{S} = \frac{1}{2}f^\dagger \boldsymbol{\sigma} f$  under the phase rotation  $f \mapsto e^{i\phi} f$ . Accordingly, by fixing  $\phi = -\theta$ , we can gauge away the phase of  $V$ .

Equation (2.4) has a particularly simple wavevector representation,

$$H_{\text{MF}} = \sum_{\mathbf{k}s} \begin{pmatrix} c_{\mathbf{k}s}^\dagger & f_{\mathbf{k}s}^\dagger \end{pmatrix} M_{\mathbf{k}s} \begin{pmatrix} c_{\mathbf{k}s} \\ f_{\mathbf{k}s} \end{pmatrix} + \frac{8NV^2}{3J}. \quad (2.6)$$

In the summation,  $\mathbf{k}$  ranges over all wavevectors in the Brillouin zone and  $s$  over the two fermion spin projections.  $N$  denotes the number of lattice sites. The coefficient matrix

$$M_{\mathbf{k}s} = \begin{pmatrix} \epsilon_{\mathbf{k}} - \mu_c - sB/2 & -V \\ -V & -\mu_f - sB/2 \end{pmatrix} \quad (2.7)$$

is a function of the free conduction-electron dispersion  $\epsilon_{\mathbf{k}} = -2t \sum_{l=1}^d \cos k^l$ , the physical parameters  $J$  and  $B$ , and the mean field parameters  $\mu_c$ ,  $\mu_f$ , and  $V$ . By writing  $\mathbf{B} \cdot \boldsymbol{\sigma}_{ss'} = B\sigma_{ss'}^3 = sB\delta_{ss'}$ , we have chosen to direct the applied magnetic field along the 3 axis.

In order to diagonalize Eq. (2.7), we construct a unitary transformation  $U_{\mathbf{k}}$ , whose columns are populated with the normalized eigenvectors of  $M_{\mathbf{k}s}$ :

$$U = \begin{pmatrix} U^{c+} & U^{c-} \\ U^{f+} & U^{f-} \end{pmatrix} = \begin{pmatrix} \frac{-I^+}{\sqrt{(I^+)^2 + V^2}} & \frac{-I^-}{\sqrt{(I^-)^2 + V^2}} \\ \frac{V}{\sqrt{(I^+)^2 + V^2}} & \frac{V}{\sqrt{(I^-)^2 + V^2}} \end{pmatrix}. \quad (2.8)$$

Note that all the  $\mathbf{k}$  dependence of  $U_{\mathbf{k}}$  resides in the function

$$I_{\mathbf{k}}^n = \frac{1}{2} \left[ \epsilon_{\mathbf{k}} - b + n \sqrt{(\epsilon_{\mathbf{k}} - b)^2 + 4V^2} \right] \quad (2.9)$$

and that both  $I_{\mathbf{k}}^n$  and  $U_{\mathbf{k}}$  are independent of the magnetic field. In Eq. (2.9), we have introduced the quantities

$$2\mu = \mu_c + \mu_f \quad \text{and} \quad b = \mu_c - \mu_f, \quad (2.10)$$

which serve as an alternate set of Lagrange multipliers (rotated 45 degrees with respect to the original set).  $\mu$  is the energy required to remove a dressed quasiparticle from the top of the Fermi sea, whereas  $b/2$  is the energy

to remove a bare conduction electron. We can think of  $\mu$  as the chemical potential of the fully interacting system. The parameter  $b$  controls how many electrons are available to compensate each local spin.

One can easily verify that Eq. (2.8) is unitary and that it diagonalizes the coefficient matrix:  $(U_{\mathbf{k}}^\dagger U_{\mathbf{k}})^{nn'} = \delta^{nn'}$  and  $(U_{\mathbf{k}}^\dagger M_{\mathbf{k}s} U_{\mathbf{k}})^{nn'} = E_{\mathbf{k}s}^n \delta^{nn'}$ , with eigenvalues given by

$$E_{\mathbf{k}s}^n = \frac{1}{2} \left[ \epsilon_{\mathbf{k}} - 2\mu - sB + n\sqrt{(\epsilon_{\mathbf{k}} - b)^2 + 4V^2} \right]. \quad (2.11)$$

When  $V \neq 0$ , the  $c$  and  $f$  electrons admix to produce the quasiparticles of the interacting system. Their dispersion is given by Eq. (2.11). Note that hybridization splits the band structure into two disjoint pieces. The quantum number  $n$  labels quasiparticles in the upper ( $n = +$ ) and lower ( $n = -$ ) bands.

In zero field, the direct band gap—which varies significantly across the Brillouin zone—takes its minimum value,  $E_{\mathbf{k}}^+ - E_{\mathbf{k}}^- = 2V$ , along the surface of  $\mathbf{k}$  points satisfying  $\epsilon_{\mathbf{k}} = b$ . The smallest indirect gap, measured from the top of the lower band to the bottom of the upper band, corresponds to the Kondo energy,  $E_{\mathbf{k}_{\min}}^+ - E_{\mathbf{k}_{\max}}^- = 2\Delta_K$ . For the  $d$ -dimensional hypercubic lattice,  $\mathbf{k}_{\max} = (\pi, \dots, \pi)$  and  $\mathbf{k}_{\min} = (0, \dots, 0)$ . More generally,  $\mathbf{k}_{\max}$  and  $\mathbf{k}_{\min}$  are the wavevectors that satisfy  $\epsilon_{\mathbf{k}_{\max}} = W/2$  and  $\epsilon_{\mathbf{k}_{\min}} = -W/2$ , where  $W$  denotes the width of the noninteracting conduction band. Thus,

$$2\Delta_K = -W/2 + \sqrt{(W/2)^2 + 4V^2} + O(b^2/W). \quad (2.12)$$

When the conduction band is near half-filling,  $b$  is a small quantity. In that case, Eq. (2.12) can be inverted, and the hybridization energy is related to the Kondo energy by

$$(2V)^2 = 2\Delta_K(2\Delta_K + W). \quad (2.13)$$

### 2.2.3 Spectral Properties

The single-particle Green's function  $G_{\mathbf{k}s}(\tau) = \langle T[c_{\mathbf{k}s}(0)c_{\mathbf{k}s}^\dagger(\tau)] \rangle$  describes the motion of a conduction electron as it propagates through the lattice. Its Fourier transform, analytically continued to the complex energy plane, has the form

$$\mathcal{G}_{\mathbf{k}s}(z) = - \sum_n \frac{|U_{\mathbf{k}}^{cn}|^2}{z - E_{\mathbf{k}s}^n}. \quad (2.14)$$

Equation (2.14) consists of two poles, at  $E_{\mathbf{k}s}^+$  and  $E_{\mathbf{k}s}^-$ , with residues  $|U_{\mathbf{k}}^{c+}|^2$  and  $|U_{\mathbf{k}}^{c-}|^2$ . The corresponding spectral function is

$$A_{\mathbf{k}s}^c(\omega) = \frac{1}{\pi} \text{Im} \mathcal{G}_{\mathbf{k}s}(\omega + i0^+) = \sum_n |U_{\mathbf{k}}^{cn}|^2 \delta(\omega - E_{\mathbf{k}s}^n). \quad (2.15)$$

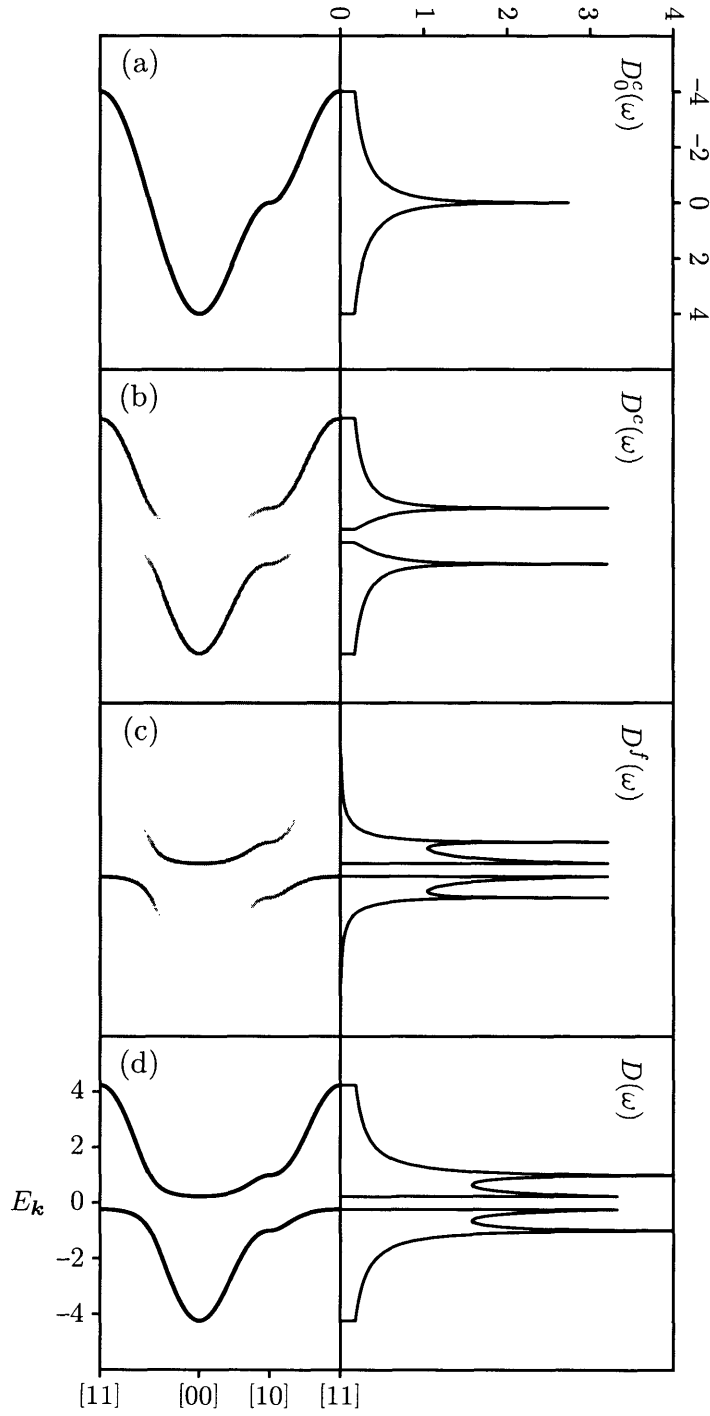


Figure 2-1: The  $\mu_c = \mu_f = B = 0$  band structure is plotted along high-symmetry lines in the Brillouin zone with the corresponding  $\mathbf{k}$ -integrated spectral weight to the right. Shown are (a) the noninteracting conduction band; hybridized bands with the (b)  $c$ -electron and (c)  $f$ -electron weight indicated in greyscale; and (d) the quasiparticle dispersion. All quantities are measured in units of  $t$ .

Similarly, the spectral function for the  $f$  fermions is

$$A_{\mathbf{k}s}^f(\omega) = \sum_n |U_{\mathbf{k}}^{fn}|^2 \delta(\omega - E_{\mathbf{k}s}^n). \quad (2.16)$$

Equations (2.15) and (2.16) have the same two-peak structure, but their spectral weights are complementary:

$$|U_{\mathbf{k}}^{cn}|^2 = \frac{(I_{\mathbf{k}}^n)^2}{(I_{\mathbf{k}}^n)^2 + V^2} = 1 - \frac{V^2}{(I_{\mathbf{k}}^n)^2 + V^2} = 1 - |U_{\mathbf{k}}^{fn}|^2. \quad (2.17)$$

The spectral weight of the conduction electrons is strong away from the hybridization gap—in those regions where the quasiparticle dispersion is close to the old noninteracting conduction band. The  $f$ -electron spectral weight, on the other hand, is concentrated in the vicinity of the hybridization gap. See Fig. 2-1. The weight is apportioned between the  $c$  and  $f$  components in such a way that the overall normalization is preserved. The conservation relation  $|U_{\mathbf{k}}^{cn}|^2 + |U_{\mathbf{k}}^{fn}|^2 = 1$  ensures that the total spectral function is given by the usual formula

$$A_{\mathbf{k}s}(\omega) = A_{\mathbf{k}s}^c(\omega) + A_{\mathbf{k}s}^f(\omega) = \sum_n \delta(\omega - E_{\mathbf{k}s}^n). \quad (2.18)$$

## 2.2.4 Fixing the Mean Field Parameters

The physics of the hybridization mean field theory depends on how the parameters  $\mu_c$ ,  $\mu_f$ , and  $V$  vary as a function of the Kondo coupling and the magnetic field. The optimal value of the hybridization strength is the one that minimizes the free energy density

$$\mathcal{F} = -\frac{1}{\beta N} \ln \text{Tr} e^{-\beta \hat{H}_{\text{MF}}} = \frac{8V^2}{3J} - \frac{1}{\beta N} \sum_{\mathbf{k}sn} \ln(1 + e^{-\beta E_{\mathbf{k}s}^n}). \quad (2.19)$$

The Lagrange multipliers are chosen to satisfy  $\langle c^\dagger c \rangle = -\partial \mathcal{F} / \partial \mu_c = n_c$ , where  $n_c$  is the conduction band filling, and  $\langle f^\dagger f \rangle = -\partial \mathcal{F} / \partial \mu_f = 1$ . Expressing these conditions in terms of the rotated Lagrange multipliers of Eq. (2.10), we find that

$$-\frac{\partial \mathcal{F}}{\partial \mu} = n_c + 1, \quad -2\frac{\partial \mathcal{F}}{\partial b} = n_c - 1, \quad \text{and} \quad \frac{\partial \mathcal{F}}{\partial V} = 0. \quad (2.20)$$

The generic result for the partial derivative of the free energy is

$$\frac{\partial \mathcal{F}}{\partial v} = \frac{16V}{3J} \frac{\partial V}{\partial v} + \frac{1}{N} \sum_{\mathbf{k}sn} f(E_{\mathbf{k}s}^n) \frac{\partial E_{\mathbf{k}s}^n}{\partial v}. \quad (2.21)$$

Differentiating Eq. (2.11) with respect to  $v = \mu, b, V$  and putting these results

into Eq. (2.21) yields

$$\frac{1}{N} \sum_{\mathbf{k}sn} f(E_{\mathbf{k}s}^n) = n_c + 1 \quad (2.22a)$$

$$\frac{1}{N} \sum_{\mathbf{k}sn} \frac{n(\epsilon_{\mathbf{k}} - b)f(E_{\mathbf{k}s}^n)}{\sqrt{(\epsilon_{\mathbf{k}} - b)^2 + 4V^2}} = n_c - 1 \quad (2.22b)$$

$$\frac{8}{3J} + \frac{1}{N} \sum_{\mathbf{k}sn} \frac{nf(E_{\mathbf{k}s}^n)}{\sqrt{(\epsilon_{\mathbf{k}} - b)^2 + 4V^2}} = 0. \quad (2.22c)$$

Note that Eq. (2.22a) defines the Luttinger volume as  $n_c + 1$ , with both the  $c$  and  $f$  electrons counted in an enlarged Fermi sea. Equation (2.22c) is the gap equation that determines  $V$ .

When either  $J$  or  $B$  is much larger than the bandwidth, the resulting gap equation

$$\frac{3J}{8} \sum_{sn} \frac{(-n)f(-\mu_f - sB/2 + nV)}{2V} = 1 \quad (2.23)$$

can be solved exactly. We find that  $2V = 3J/4$  when  $J \gg |B|$  and that  $2V = 0$  when  $|B| \gg J$ . In small fields, the hybridization energy is equal to the singlet binding energy. When the applied field is strong enough to break apart a singlet pair, the hybridization vanishes. We can verify this behaviour by considering the exact strong-coupling result

$$4V^2 = \langle \{ [[c, \hat{H}], \hat{H}], c^\dagger \} \rangle - \langle \{ [c, \hat{H}], c^\dagger \} \rangle^2, \quad (2.24)$$

which evaluates to  $2V = \frac{3J}{4} \sqrt{1 - \frac{4}{3} |\langle \hat{S}^3 \rangle| (|\langle \hat{S}^3 \rangle| + 1)}$ . Here, the hybridization energy decreases from  $3J/4$  to 0 as the magnetic field polarizes the local spins ( $|\langle \hat{S}^3 \rangle| \rightarrow 1/2$ ). This suggests that hybridization and uniform magnetization are in competition and do not coexist happily in the KLM.

## 2.3 Thermodynamic Limit

In Eqs. (2.22), it is profitable to eliminate the  $\mathbf{k}$  summations in favour of energy integrals weighted by the density of states (DOS)

$$D(\omega) = \frac{1}{N} \sum_{\mathbf{k}n} \delta(\omega - I_{\mathbf{k}}^n). \quad (2.25)$$

In the thermodynamic limit ( $N \rightarrow \infty$ ), the set of  $I_{\mathbf{k}}^n$  values is dense, and Eq. (2.25) is a smooth function of  $\omega$ . [As a convenience, we have defined the DOS as the spectrum of  $I_{\mathbf{k}}^n$  rather than  $E_{\mathbf{k}s}^n$ , which makes the function independent of the magnetic field. The true DOS is offset from Eq. (2.25)

wavevector sum	DOS integral
$E_{\mathbf{k}s}^n$	$\omega + b/2 - \mu - sB/2$
$I_{\mathbf{k}}^n$	$\omega$
$I_{\mathbf{k}}^{-n}$	$-V^2/\omega$
$\epsilon_{\mathbf{k}} - b$	$(\omega^2 - V^2)/\omega$
$n$	$\text{sgn}(\omega)$
$\sum_{\mathbf{k}n}$	$\int d\omega D(\omega)$

Table 2.1: A wavevector sum is transformed to a density of states integral by making the substitutions listed in this conversion chart.

by  $-b/2 + \mu + sB/2 = \mu_f + sB/2$ .] Applying the delta function identity

$$\sum_{n=\pm 1} \delta\left(x - 2\omega + n\sqrt{x^2 + 4V^2}\right) = \frac{1}{2} \left(1 + \frac{V^2}{\omega^2}\right) \delta\left(x - \omega\left(1 - \frac{V^2}{\omega^2}\right)\right) \quad (2.26)$$

(with  $x = \epsilon_{\mathbf{k}} - b$ ) to Eq. (2.25), we can show that  $D(\omega) \sim 1 + V^2/\omega^2$ . The correspondence between quantities in the wavevector and energy representations is summarized in Table 2.1.

The most important feature of the DOS is that it develops a band gap centred on  $\omega = 0$  as  $V$  increases from zero. The DOS of the noninteracting conduction electrons can be written as the product of a line-shape function  $g(\omega)$  and a heaviside function that ensures that the density of states vanishes outside the band:

$$D_0^c(\omega) = \frac{1}{N} \sum_{\mathbf{k}} \delta(\omega - \epsilon_{\mathbf{k}}) = g(\omega)\theta(W^2 - 4\omega^2). \quad (2.27)$$

In the interacting system, the conduction-electron DOS has the same basic form,

$$D^c(\omega) = \frac{1}{N} \sum_{\mathbf{k}n} |U_{\mathbf{k}}^{cn}|^2 \delta(\omega - I_{\mathbf{k}}^n) = g(\lambda(\omega))\theta(W^2 - 4\lambda(\omega)^2), \quad (2.28)$$

but its energy scale is renormalized by the function  $\lambda(\omega) = \omega(1 - V^2/\omega^2) + b$ , which comes from the delta function on the right-hand side of Eq. (2.26). As a result, the argument of the heaviside function in Eq. (2.28) is a fourth degree polynomial whose roots

$$\begin{aligned} \omega_1 &= -\sqrt{(W/4 + b/2)^2 + V^2} - W/4 - b/2 \\ \omega_2 &= -\sqrt{(W/4 - b/2)^2 + V^2} + W/4 - b/2 \\ \omega_3 &= +\sqrt{(W/4 + b/2)^2 + V^2} - W/4 - b/2 \\ \omega_4 &= +\sqrt{(W/4 - b/2)^2 + V^2} + W/4 - b/2 \end{aligned} \quad (2.29)$$

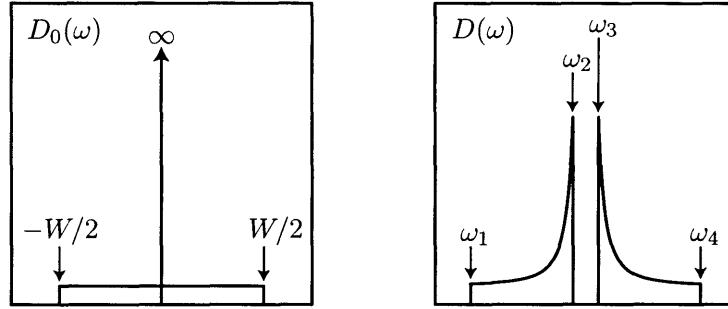


Figure 2-2: The total density of states for the noninteracting system  $D_0(\omega)$  consists of an  $f$ -level delta-function peak at  $\omega = 0$  superimposed over a conduction band of width  $W$ . When  $V \neq 0$ , hybridization breaks the spectral weight into lower ( $\omega_1 < \omega < \omega_2$ ) and upper ( $\omega_3 < \omega < \omega_4$ ) bands.

delineate the band edges:

$$\theta(W^2 - 4\lambda(\omega)^2) = \sum_{i=1}^4 (-1)^{i+1} \theta(\omega - \omega_i). \quad (2.30)$$

Spectral weight exists only at energies in a lower band from  $\omega_1$  to  $\omega_2$  and in an upper band from  $\omega_3$  to  $\omega_4$ . The two bands are separated by a gap of width  $2\Delta = \omega_3 - \omega_2$ . See Fig. 2-2.

A similar analysis shows that the DOS for the  $f$  electrons differs from  $D^c(\omega)$  by a factor of  $V^2/\omega^2$ . Hence,  $D(\omega) = D^c(\omega) + D^f(\omega)$ , the total DOS, is equal to

$$D(\omega) = \left(1 + \frac{V^2}{\omega^2}\right) g(\lambda(\omega)) \sum_{i=1}^4 (-1)^{i+1} \theta(\omega - \omega_i). \quad (2.31)$$

Then, using the conversion chart in Table 2.1, we can re-express the free energy density [from Eq. (2.19)] as

$$\mathcal{F} = \frac{8V^2}{3J} - \frac{1}{\beta} \sum_s \int d\omega D(\omega) \ln\left(1 + e^{-\beta(\omega - \mu_f - sB/2)}\right). \quad (2.32)$$

The constituent equations of the mean field theory [from Eqs. (2.22)] can be written compactly as

$$\sum_s \int d\omega f(\omega - \mu_f - sB/2) \begin{Bmatrix} D^c(\omega) \\ D^f(\omega) \\ -\frac{3J}{8\omega} D^c(\omega) \end{Bmatrix} = \begin{Bmatrix} n_c \\ 1 \\ 1 \end{Bmatrix}. \quad (2.33)$$

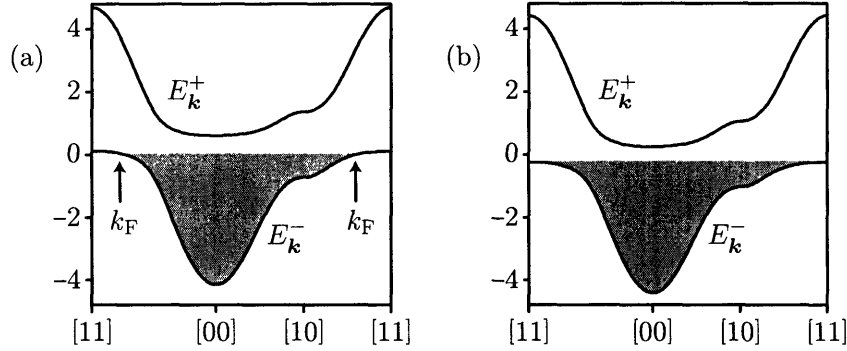


Figure 2-3: (a) The heavy metal has a partially filled lower band. The quasi-particle states are occupied up to the Fermi wavevector  $k_F$ . (b) The Kondo insulator has a completely filled lower band. There is no Fermi surface.

## 2.4 Heavy Fermion Metal

### 2.4.1 Characterizing the Ground State

When the chemical potential lies outside the hybridization gap, the system behaves as a Fermi liquid. For concreteness, let us suppose that the lower band is filled to some point *below* the hybridization gap. Then the relevant dispersion relation is that of the lower band,

$$E_{\mathbf{k}}^- = \frac{1}{2} \left[ \epsilon_{\mathbf{k}} - 2\mu - \sqrt{(\epsilon_{\mathbf{k}} - b)^2 + 4V^2} \right]. \quad (2.34)$$

Here we have assumed that either there is no applied magnetic field or that the Zeeman splitting is small enough to be ignored.

The key feature of the heavy fermion state is the hybridization gap. It generates a region of very shallow dispersion near the band gap edge, which is responsible for the large effective mass of the quasiparticles. This situation is depicted in Fig. 2-3(a). The heavy fermion state is metallic and possesses a well-defined Fermi surface given by the set of  $\mathbf{k}$  points satisfying  $E_{\mathbf{k}}^- = 0$ . Let  $\mathbf{k}_F$  denote a point on this surface. Then  $E_{\mathbf{k}_F}^- = 0$  implies that

$$\epsilon_{\mathbf{k}_F} = \frac{b^2 - 4\mu^2 + 4V^2}{2(b - 2\mu)}. \quad (2.35)$$

Making use of the fact that  $b - 2\mu = -2\mu_f$ , we can express this condition as

$$\epsilon_{\mathbf{k}_F} - 2\mu = \frac{(b - 2\mu)^2 + 4V^2}{2(b - 2\mu)} = \frac{\mu_f^2 + V^2}{-\mu_f}. \quad (2.36)$$

The effective mass  $m^*$  of the quasiparticle excitations is a function of

the band curvature at the Fermi surface. It is related to the noninteracting band mass by the variation  $m^* \delta E_{\mathbf{k}}^- = m \delta \epsilon_{\mathbf{k}}$  in the vicinity of  $\mathbf{k}_F$ . Hence, the derivative

$$\frac{\partial E_{\mathbf{k}}^-}{\partial \epsilon_{\mathbf{k}}} = \frac{1}{2} \left[ 1 - \frac{\epsilon_{\mathbf{k}} - b}{\sqrt{(\epsilon_{\mathbf{k}} - b)^2 + 4V^2}} \right] = \frac{1}{2} \left[ \frac{b - 2\mu - 2E_{\mathbf{k}}^-}{\epsilon_{\mathbf{k}} - 2\mu - 2E_{\mathbf{k}}^-} \right] \quad (2.37)$$

may be inverted and evaluated at the Fermi surface to give the mass enhancement factor

$$\frac{m^*}{m} = \left( \frac{\partial E_{\mathbf{k}}^-}{\partial \epsilon_{\mathbf{k}}} \right)_{\mathbf{k}=\mathbf{k}_F}^{-1} = \frac{2(\epsilon_{\mathbf{k}_F} - 2\mu)}{b - 2\mu} = 1 + \frac{V^2}{\mu_f^2}. \quad (2.38)$$

### 2.4.2 Detailed Mean Field Solution

A heavy fermion state results when the Fermi level is close to the hybridization gap edge, where the bands are strongly renormalized. Thus, heavy fermion effects are most pronounced when the system is near half-filling. Accordingly, let us represent the conduction band filling by  $n_c = 1 - x$  where  $x \ll 1$ . (The Fermi surface volume is  $2 - x$ .) Further, since Van Hove singularities do not play an important role here, let us assume that the density of levels in Eq. (2.31) is flat and replace the line-shape function by its average value  $g \rightarrow 1/W$ . Then the total DOS is

$$D(\omega) = \frac{1}{W} \left( 1 + \frac{V^2}{\omega^2} \right) \sum_{i=1}^4 (-1)^{i+1} \theta(\omega - \omega_i). \quad (2.39)$$

Since  $b$  controls the difference between the  $c$ - and  $f$ -electron occupation, it is proportional to the number of holes in the lower band. Thus  $b \sim x$  is also a small parameter in the problem. To order  $b^2/W$ , the energies of the band edges can be written as

$$\omega_1 = -W/2 - \Delta - \left( \frac{W + 2\Delta}{W + 4\Delta} \right) b \quad (2.40a)$$

$$\omega_2 = -\Delta - \left( \frac{2\Delta}{W + 4\Delta} \right) b \quad (2.40b)$$

$$\omega_3 = +\Delta - \left( \frac{2\Delta}{W + 4\Delta} \right) b \quad (2.40c)$$

$$\omega_4 = +W/2 + \Delta - \left( \frac{W + 2\Delta}{W + 4\Delta} \right) b. \quad (2.40d)$$

This comes from expanding Eqs. (2.29) in  $b$  and expressing the result in terms of the gap parameter  $2\Delta = \omega_3 - \omega_2 = \sqrt{(W/2)^2 + 4V^2} - W/2$ . The gap is related to the hybridization energy by  $(2V)^2 = 2\Delta(2\Delta + W)$ .

Let us consider the zero-field case. Since  $E_{\mathbf{k}}^n = I_{\mathbf{k}} - \mu_f$ , the  $c$ - and  $f$ -electron fillings can be computed by integrating  $D^c(\omega)$  and  $D^f(\omega)$  from

$\omega_1$  up to  $\mu_f \lesssim \omega_2$ . Neglecting small terms of order  $b\Delta/W$ , we write  $\omega_1 = -W/2 - \Delta - b$ . Following Eq. (2.33), we find that

$$\langle c^\dagger c \rangle = \frac{2}{W} \int_{\omega_1}^{\mu_f} d\omega = 1 + \frac{2}{W}(\Delta + b + \mu_f). \quad (2.41)$$

Since the conduction band filling is  $1 - x$ ,

$$\Delta + b = -\frac{Wx}{2} - \mu_f \quad \text{or, equivalently,} \quad \mu_c = -\Delta - \frac{Wx}{2}. \quad (2.42)$$

We compute the  $f$ -level occupation in a similar fashion—except that now, using the value of  $\Delta + b$  in Eq. (2.42), we can specify the lower integration bound as  $\omega_1 = -\frac{W}{2}(1 - x) + \mu_f$ . This yields

$$\langle f^\dagger f \rangle = \frac{2V^2}{W} \int_{\omega_1}^{\mu_f} \frac{d\omega}{\omega^2} = \frac{V^2(1 - x)}{\mu_f[\mu_f - \frac{W}{2}(1 - x)]}. \quad (2.43)$$

Imposing the occupation constraint  $\langle f^\dagger f \rangle = 1$  fixes the  $f$ -electron chemical potential at  $\mu_f = -\Delta$ . Having determined  $\mu_c$  and  $\mu_f$ , we can compute

$$\mu = -\Delta - \frac{Wx}{4} \quad \text{and} \quad b = -\frac{Wx}{2}. \quad (2.44)$$

As  $x$  increases from zero, the chemical potential drops below the lower edge of the hybridization gap, thus freeing up quasiparticle states at the top of the lower band. Equation (2.44) also confirms that  $b \sim x$ , as we argued earlier.

The value of  $\Delta$  is determined from the gap equation

$$1 = -\frac{3J}{4W} \int_{\omega_1}^{\mu_f} \frac{d\omega}{\omega} = -\frac{3J}{4W} \ln\left(\frac{2\Delta}{W(1 - x) + 2\Delta}\right), \quad (2.45)$$

whose solution is given by the Kondo energy

$$2\Delta_K = W(1 - x) \frac{e^{-4W/3J}}{1 - e^{-4W/3J}}. \quad (2.46)$$

We can now go back and complete our calculation of the mass enhancement factor, which depends explicitly on the position of the  $f$  level. Inserting  $\mu_f = -\Delta_K$  into Eq. (2.38) gives

$$\frac{m^*}{m} = 2 + \frac{W}{2\Delta_K}. \quad (2.47)$$

For realistic values of the physical parameters, the Kondo coupling is always smaller than the bandwidth. From Eq. (2.46), we see that  $J < W$  implies that  $\Delta_K \ll W$ , which guarantees that the mass enhancement factor is a large number.

## 2.5 Kondo Insulator

### 2.5.1 Zero-field Ground State

When its conduction band is half-filled ( $n_c = 1$ ), the KLM is particle-hole symmetric. This symmetry fixes the Lagrange multipliers  $\mu_c$  and  $\mu_f$  at the centre of the band; hence  $\mu = b = 0$ . Since the chemical potential sits inside the hybridization gap, the lower band is completely filled, the upper band is completely empty, and there is no Fermi surface. See Fig. 2-3(b). This state is an insulator. As we shall see, its charge excitations are gapped by the Kondo energy  $2\Delta_K$ .

The Kondo insulator ground state has an energy density  $\mathcal{U} = u + 8V^2/3J$ , where  $u = 2 \int d\omega D(\omega)\omega f(\omega)$  is the average quasiparticle kinetic energy. The quasiparticle states are filled from  $\omega_1$  to  $\omega_2$  and thus

$$u = \frac{2}{W} \int_{-W/2-\Delta}^{-\Delta} d\omega \left( \omega + \frac{V^2}{\omega} \right) = -\frac{W}{4} - \Delta + \frac{2V^2}{W} \ln\left(\frac{2\Delta}{W+2\Delta}\right). \quad (2.48)$$

Adding the hybridization self-energy gives the total energy density

$$\mathcal{U} = -\frac{W}{4} - \Delta + \frac{2V^2}{W} \left[ \ln\left(\frac{2\Delta}{W+2\Delta}\right) + \frac{4W}{3J} \right]. \quad (2.49)$$

Since the hybridization is related to the gap parameter by the identity  $(2V)^2 = 2\Delta(2\Delta + W)$ , we can treat Eq. (2.49) as a function of  $\Delta$  alone.

The value of the gap parameter that minimizes  $\mathcal{U}(\Delta)$  satisfies

$$\frac{\partial \mathcal{U}}{\partial \Delta} = \frac{1}{W} (4\Delta + W) \left[ \ln\left(\frac{2\Delta}{W+2\Delta}\right) + \frac{4W}{3J} \right] = 0. \quad (2.50)$$

The solution is  $\Delta = \Delta_K$ , where

$$2\Delta_K = \frac{W e^{-4W/3J}}{1 - e^{-4W/3J}}. \quad (2.51)$$

This is precisely the Kondo energy that was previously reported in Eq. (2.46) (with  $x = 0$ ). At large  $J$ , the Kondo energy is equal to the binding energy of a spin singlet; at small  $J$ , it is exponentially suppressed:

$$2\Delta_K = \begin{cases} \frac{3J}{4} & \text{as } J \rightarrow \infty \\ W e^{-4W/3J} & \text{as } J \rightarrow 0. \end{cases} \quad (2.52)$$

Substitution of Eqs. (2.50) and (2.51) into Eq. (2.49) yields the ground state energy density  $\mathcal{U}_K = -W/4 - \Delta_K$ . Note that the Kondo insulator is energetically favourable to the non-hybridized metallic state (having energy  $-W/4$ ) for all values of the Kondo coupling. Even an infinitesimal  $J$  is sufficient to open a hybridization gap.

### 2.5.2 Field-induced Metal-insulator Transition

In a magnetic field, the calculation proceeds as before except that the integrals are modified to account for the Zeeman splitting of the spin up and spin down bands. There is now a contribution to the energy density

$$\sum_s \int d\omega D(\omega)(\omega - sB/2)f(\omega - sB/2) = u - Bm \quad (2.53)$$

from both the kinetic energy

$$\begin{aligned} u &= \sum_s \int d\omega D(\omega)\omega f(\omega - sB/2) \\ &= \begin{cases} -\frac{W}{4} - \Delta + \frac{2V^2}{W} \ln\left(\frac{2\Delta}{W+2\Delta}\right) & \text{if } |B| < 2\Delta \\ \frac{B^2 - (W+2\Delta)^2}{4W} + \frac{2V^2}{W} \ln\left(\frac{|B|}{W+2\Delta}\right) & \text{if } 2\Delta < |B| < W + 2\Delta \\ 0 & \text{if } |B| > W + 2\Delta \end{cases} \end{aligned} \quad (2.54)$$

and the magnetization

$$\begin{aligned} m &= \sum_s \left(\frac{s}{2}\right) \int d\omega D(\omega)f(\omega - sB/2) \\ &= \begin{cases} 0 & \text{if } |B| < 2\Delta \\ \frac{|B|(|B+W) - 2\Delta(2\Delta+W)}{2BW} & \text{if } 2\Delta < |B| < W + 2\Delta \\ 1 & \text{if } |B| > W + 2\Delta. \end{cases} \end{aligned} \quad (2.55)$$

Equations (2.54) and (2.55) are defined piecewise because  $u$  and  $m$  are continuous but not smooth functions of the magnetic field strength. Their behaviour depends crucially on whether the applied field is large enough to overcome the hybridization gap. For example, so long as  $|B|$  does not meet the gap threshold, the system remains nonmagnetic. When  $|B|$  first exceeds  $2\Delta$ , the system begins to magnetize. Eventually, at sufficiently large fields, the quasiparticles polarize completely. See Fig. 2-4.

In the intermediate field strength regime ( $2\Delta < |B| < W + 2\Delta$ ), the total energy density  $\mathcal{U} = u - Bm + 8V^2/3J$  has the form

$$\mathcal{U} = -\frac{W}{4} + \frac{\Delta^2}{W} - \frac{1}{4W}|B|(|B| + 2W) + \frac{2V^2}{W} \left[ \ln\left(\frac{|B|}{W + 2\Delta}\right) + \frac{4W}{3J} \right]. \quad (2.56)$$

Once again, we treat  $\mathcal{U}$  as a function of  $\Delta$  alone and compute its derivative,

$$\frac{\partial \mathcal{U}}{\partial \Delta} = \frac{1}{W}(2\Delta + W) \left[ \ln\left(\frac{|B|}{W + 2\Delta}\right) + \frac{4W}{3J} \right] = 0. \quad (2.57)$$

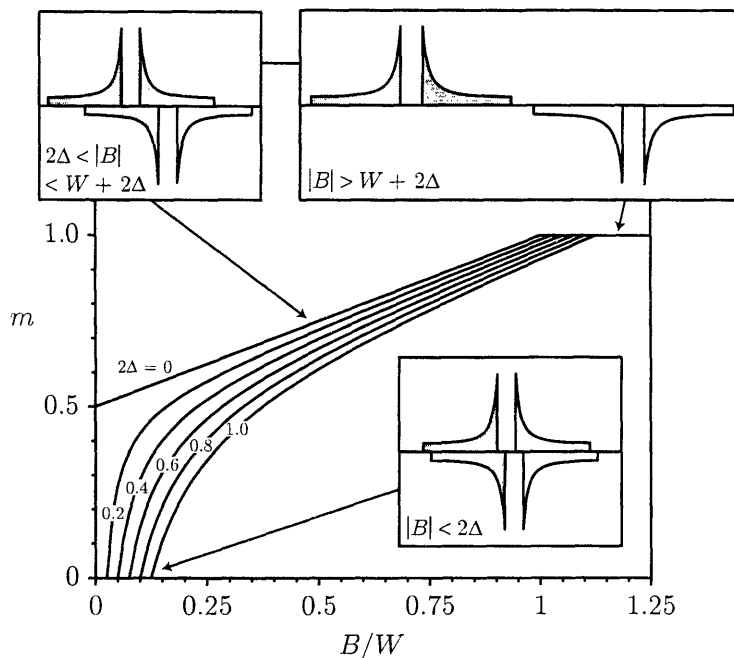


Figure 2-4: The magnetization is plotted as a function of applied magnetic field for various values of the gap width. As the magnetic field is increased from zero, the net magnetization of the sample remains zero until a critical threshold is reached. The magnetization then increases monotonically with the field strength until it saturates.

Equation (2.57) tells us that  $\mathcal{U}(\Delta)$  has an extremum at  $\Delta = \Delta_M$ , where

$$2\Delta_M = |B|e^{4W/3J} - W = \frac{|B|(W + 2\Delta_K)}{2\Delta_K} - W. \quad (2.58)$$

The second equality follows from comparison with Eq. (2.51).

This solution corresponds to a magnetized heavy metal (with magnetism and hybridization coexisting). Its energy, however, is a convex function of  $\Delta_M$ ; we find that  $\mathcal{U}_M = -W/4 + \Delta_M^2/W - |B|/2 - B^2/4W$ . Such a state is thermodynamically unstable with respect to the normal metallic state in which  $\Delta = 0$  and  $\mathcal{U}_{M0} = -W/4 - |B|/2 - B^2/4W$ . This rules out the possibility of a field-induced transition from the Kondo insulator to a heavy metal. As depicted in Fig. 2-5, we can solve for the critical value of the field strength by solving for the energy crossing  $\mathcal{U}_K = \mathcal{U}_{M0}$ . We find that

$$B_c = \sqrt{W^2 + 4\Delta_K} - W \approx 2\Delta_K - 2\Delta_K^2/W. \quad (2.59)$$

The general picture from the hybridization mean field theory is as follows. The KLM at half-filling has a Kondo insulator ground state. Initially,

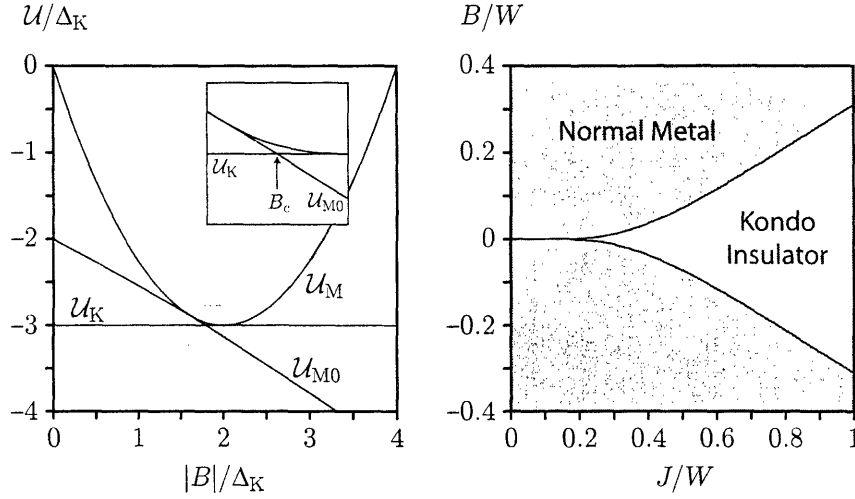


Figure 2-5: (Left) The energy densities of the (K) Kondo insulator, (M) heavy metal, and (M0) normal metal ground states are plotted as a function of the magnetic field strength. The curves shown are for a bandwidth of  $W/\Delta_K = 8$ . The Kondo insulator energy  $\mathcal{U}_K$  is independent of the magnetic field. It is the thermodynamically stable ground state until  $|B| = B_c \lesssim 2\Delta_K$ . (Right) The phase diagram of the KLM consists of a Kondo insulator phase at large  $J$  and a normal metal phase at large  $B$ . The two phases are separated by a line of first order transitions.

application of a magnetic field leaves the hybridization strength unchanged. As the magnetic field is ramped up, the spin up and spin down bands simply shift with respect to one another and the charge gap  $\Delta_c = 2\Delta_K - |B|$  decreases linearly. When  $|B|$  gets within  $2\Delta_K^2/W$  of the Kondo energy  $2\Delta_K$ , the system undergoes a first order transition in which the hybridization field collapses and the magnetization abruptly jumps to

$$m = \frac{1}{2} \text{sgn}(B) \sqrt{1 + \frac{4\Delta_K}{W}}. \quad (2.60)$$

## Chapter 3

# RKKY Antiferromagnetism

### 3.1 Outline

Within the hybridization mean field theory, the half-filled KLM has an insulating, nonmagnetic ground state for all values of the Kondo coupling  $J$ . With the application of a sufficiently large magnetic field, the system undergoes a first order transition to a normal metallic state in which the conduction electrons are completely decoupled from the quenched (completely spin polarized) local moments. This description is inadequate because it ignores the possible magnetic ordering of the spin lattice.

In this chapter, we consider how the hybridization picture is modified by the inclusion of RKKY antiferromagnetism. A diagrammatic resummation technique is employed to compute the renormalized Kondo and RKKY couplings, which are scaled up from their bare values by Stoner-like enhancement factors. Tracking where they diverge determines the Kondo and Néel temperatures,  $T_K$  and  $T_N$ , below which the Kondo lattice system becomes unstable to singlet formation and magnetic order, respectively.

This approach is similar in spirit to that of Doniach [19], who first considered the competition between Kondo physics and antiferromagnetism in the zero-field problem. Doniach recognized that the lattice of localized spins experiences an effective RKKY interaction  $R_{ij}(\tau - \tau') \hat{S}_i(\tau) \cdot \hat{S}_j(\tau')$ , whose coupling  $R = -(J^2/2)\Pi$  is proportional to the spin susceptibility of the conduction sea,  $\Pi_{ij}(\tau - \tau') = \partial \langle \frac{1}{2} c_i^\dagger(\tau) \sigma^3 c_i(\tau) \rangle / \partial B_j(\tau') \big|_{B_j(\tau')=0}$ . He showed that when  $J$  is sufficiently small,  $T_N$  exceeds  $T_K$ , indicating that RKKY-driven magnetism dominates in the weak-coupling regime. He went on to argue that—insofar as  $T_K$  and  $T_N$  constitute the characteristic energy scales of the Kondo singlet and antiferromagnetic ground states—one can infer the existence of a zero-temperature quantum critical point. See Fig. 3-1.

We want to generalize Doniach's calculation to the case of nonzero magnetic field. This amounts to extending Fig. 3-1 into the  $J$ - $B$  plane. The main complication is that, in the presence of an external field, the RKKY interaction is no longer isotropic in real space. [The field picks out a pre-

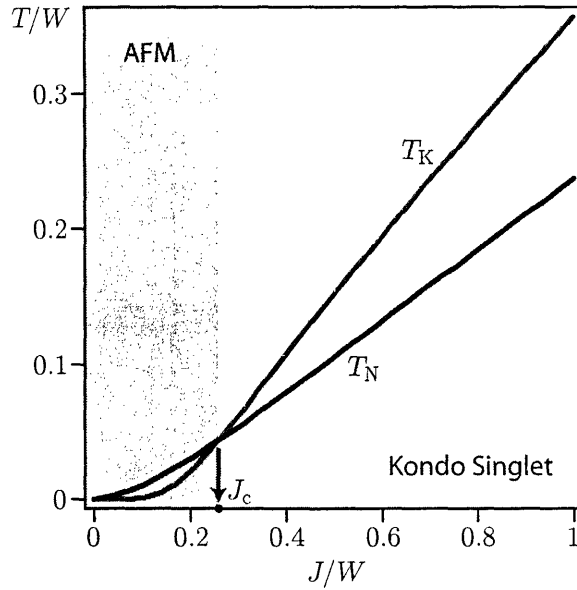


Figure 3-1:  $T_K$  and  $T_N$  are plotted for the half-filled Kondo lattice model as a function of the Kondo coupling  $J$ . For large  $J$ ,  $T_K > T_N$ . For small  $J$ ,  $T_K$  is exponentially suppressed and  $T_N > T_K$ . This suggests the existence of a zero-field transition that can be driven by tuning  $J$  through some critical value  $J_c$ . When  $J < J_c$ , the ground state is antiferromagnetic. When  $J > J_c$ , the ground state is a Kondo singlet.

ferred direction, reducing the spin rotation symmetry from  $O(3)$  to  $O(2)$ .] The lower symmetry can be accommodated by using the more general interaction  $\hat{S}_i(\tau) \cdot \vec{R}_{ij}(\tau - \tau') \cdot \hat{S}_j(\tau')$ , which now depends on the coupling *tensor*  $\vec{R} = -(J^2/2)\vec{\Pi}$ . The spin susceptibility

$$\vec{\Pi}_{ij}(\tau - \tau') = \left. \frac{\partial \langle \frac{1}{2} c_i^\dagger(\tau) \sigma c_i(\tau) \rangle}{\partial \mathbf{B}_j(\tau')} \right|_{\mathbf{B}_j(\tau') = \mathbf{B}} \quad (3.1)$$

is promoted to a  $3 \times 3$  matrix, which is block diagonal in the directions perpendicular and parallel to the field. Its Fourier/Matsubara components have the form

$$\vec{\Pi}(\mathbf{q}, \nu_n) = \begin{pmatrix} \text{Re } \Pi_\perp & i \text{Im } \Pi_\perp & \\ -i \text{Im } \Pi_\perp & \text{Re } \Pi_\perp & \\ & & \text{Re } \Pi_\parallel \end{pmatrix}. \quad (3.2)$$

We have introduced the notation  $\Pi_\perp = \Pi_{\uparrow\downarrow} = \Pi_{\downarrow\uparrow}^*$  and  $\Pi_\parallel = \Pi_{\uparrow\uparrow} = \Pi_{\downarrow\downarrow}^*$ .

As a result of this directional dependence, we must regard the system as having two Néel temperatures,  $T_{N\perp}$  and  $T_{N\parallel}$ . These mark the onset of stag-

gered order perpendicular and parallel to the applied field. Since the Kondo physics is singlet in character, however,  $T_K$  is insensitive to the field direction. Thus,  $T_K$ ,  $T_{N\perp}$ , and  $T_{N\parallel}$  constitute the complete set of relevant energy scales in the problem. By computing their values as a function of the physical parameters  $J$  and  $B$ , we can construct a rudimentary phase diagram. Each distinct region of the diagram is identified with a particular ordering of the temperature scales according to their relative magnitudes. This analysis suggests that, with the application of a sufficiently large magnetic field, the large- $J$  Kondo insulator gives way to a canted antiferromagnet.

Finally, we investigate how the antiferromagnetism first emerges. We derive the magnon dispersion relations for the triplet excitations above the singlet ground state and show that the transverse-mode bands descend as a function of applied field. At a critical value of the field strength, the energy of the transverse magnons with wavevector  $\mathbf{Q} = (\pi, \dots, \pi)$  drops to zero, and the system becomes unstable to transverse antiferromagnetic order. The spin wave theory also predicts a high-field transition at which the spins become saturated in the direction of the field and the antiferromagnetism vanishes.

### 3.2 Effective Kondo and RKKY Couplings

Our model Hamiltonian is the sum of hopping, exchange, and Zeeman terms:

$$\hat{H}_t = -t \sum_{\langle ij \rangle} (c_i^\dagger c_j + c_j^\dagger c_i), \quad (3.3a)$$

$$\hat{H}_J = J \sum_i \frac{1}{2} c_i^\dagger \boldsymbol{\sigma} c_i \cdot \hat{\mathbf{S}}_i = \frac{J}{4} \sum_i c_i^\dagger \boldsymbol{\sigma} c_i \cdot f_i^\dagger \boldsymbol{\sigma} f_i, \quad (3.3b)$$

$$\hat{H}_B = -\mathbf{B} \cdot \sum_i (\frac{1}{2} c_i^\dagger \boldsymbol{\sigma} c_i + \hat{\mathbf{S}}_i) = -\frac{B}{2} \sum_i (c_i^\dagger \sigma^3 c_i + f_i^\dagger \sigma^3 f_i). \quad (3.3c)$$

In Eqs. (3.3b) and (3.3c), we have partially ‘undone’ the Schrieffer-Wolf transformation by reintroducing an explicit  $f$  electron. As in Sect. 2.2.1, we treat the  $f^\dagger f = 1$  constraint on average (with  $\mu_c = \mu_f = 0$ ).

The diagrammatic calculation proceeds as follows. We group the Hamiltonian into two pieces,  $\hat{H}_0 = \hat{H}_t + \hat{H}_B$  and  $\hat{H}_1 = \hat{H}_J$ , and let  $\hat{H}_1$  serve as a perturbation around the noninteracting system  $\hat{H}_0$ . At lowest order,  $\hat{H}_1$  makes a contribution

$$\frac{1}{2} \sum_{ij} \int_0^\beta d\tau d\tau' \mathcal{V}_{ij;sr;s'r'}^0(\tau - \tau') c_{is}^\dagger(\tau) c_{ir}(\tau) f_{js'}^\dagger(\tau') f_{jr'}(\tau') \quad (3.4)$$

to the Euclidean action, where

$$\mathcal{V}_{ij;sr;s'r'}^0(\tau - \tau') = \frac{J}{2} \boldsymbol{\sigma}_{sr} \cdot \boldsymbol{\sigma}_{s'r'} \delta_{ij} \delta(\tau - \tau') \quad (3.5)$$

is a contact interaction in space and imaginary time between the  $c$  and  $f$  electrons. The higher order contributions renormalize the bare Kondo interaction and induce additional interaction terms.

At the level of two-body interactions, the effective action looks like

$$\begin{aligned}
S^{\text{eff}} = & \dots + \sum_i \int_0^\beta d\tau \hat{\chi}_i^{\mu\dagger}(\tau) J^{\mu\nu}(\tau - \tau') \hat{\chi}_i^\nu(\tau') \\
& + \frac{1}{2} \sum_{ij} \int_0^\beta d\tau d\tau' \hat{T}_i^{\mu\dagger}(\tau) U_{ij}^{\mu\nu}(\tau - \tau') \hat{T}_j^\nu(\tau') \\
& + \frac{1}{2} \sum_{ij} \int_0^\beta d\tau d\tau' \hat{S}_i^{\mu\dagger}(\tau) R_{ij}^{\mu\nu}(\tau - \tau') \hat{S}_j^\nu(\tau') + \dots
\end{aligned} \tag{3.6}$$

Here,  $\hat{\chi}^\mu = \frac{1}{\sqrt{2}} f^\dagger \sigma^\mu c$  is the hybridization operator that expresses the local singlet/triplet pairing.  $\hat{T}^\mu = \frac{1}{2} c^\dagger \sigma^\mu c$  and  $\hat{S}^\mu = \frac{1}{2} f^\dagger \sigma^\mu f$  are charge/spin operators for the  $c$  and  $f$  electrons. The interaction strengths are given by the renormalized Kondo coupling  $J^{\mu\nu}$ , the RKKY coupling  $R_{ij}^{\mu\nu}$ , and its  $c$ -electron counterpart  $U_{ij}^{\mu\nu}$ . Making use of the identity  $\frac{1}{2} \text{tr} \sigma^\mu \sigma^\nu = \delta^{\mu\nu}$ , we can show that

$$J^{\mu\nu} = \frac{1}{4} \sigma_{rs}^\mu \mathcal{V}_{sr, s'\tau'}^{cf} \sigma_{r'\tau'}^\nu. \tag{3.7}$$

Here,  $\mathcal{V}^{cf}$  is the effective two-body interaction for a scattering event between a  $c$  and an  $f$  electron. Analogous formulas relate the coupling  $U_{ij}^{\mu\nu}$  to  $\mathcal{V}_{ij}^{cc}$  and  $R_{ij}^{\mu\nu}$  to  $\mathcal{V}_{ij}^{ff}$ . Thus, the three terms in Eq. (3.6) represent interactions between all possible pairs of the two fermion species.

The effective interactions can be computed via diagrammatic expansion. As an approximation, we keep only the most divergent terms at each order, in each of the three interaction channels. This infinite subset of leading order diagrams is illustrated in Fig. 3-2. The corresponding Fourier/Matsubara coefficients obey the recurrence relations

$$\mathcal{V}_{sr; s'\tau'}^{cf}(\nu_n) = -\frac{J}{2} \sigma_{sr'} \cdot \sigma_{s'\tau} + \frac{J}{2} \sigma_{ss''} \cdot \sigma_{\tau''\tau} \Pi_{s''\tau''}^{cf}(\nu_n) \mathcal{V}_{s''\tau''; s'\tau'}^{cf}(\nu_n) \tag{3.8a}$$

$$\begin{aligned}
\mathcal{V}_{sr; s'\tau'}^{cc}(\mathbf{q}, \nu_n) = & -\frac{J^2}{4} \sigma_{sr} \cdot \sigma_{\tau''s''} \Pi_{\tau''s''}^{ff}(\nu_n) \sigma_{s''\tau''} \cdot \sigma_{s'\tau'} \\
& + \frac{J^2}{4} \sigma_{sr} \cdot \sigma_{\tau''s''} \Pi_{\tau''s''}^{ff}(\nu_n) \sigma_{s''\tau''} \cdot \sigma_{\tau''s''} \Pi_{\tau''s''}^{cc}(\mathbf{q}, \nu_n) \mathcal{V}_{s''\tau''; s'\tau'}^{cc}
\end{aligned} \tag{3.8b}$$

$$\begin{aligned}
\mathcal{V}_{sr; s'\tau'}^{ff}(\mathbf{q}, \nu_n) = & -\frac{J^2}{4} \sigma_{sr} \cdot \sigma_{\tau''s''} \Pi_{\tau''s''}^{cc}(\mathbf{q}, \nu_n) \sigma_{s''\tau''} \cdot \sigma_{s'\tau'} \\
& + \frac{J^2}{4} \sigma_{sr} \cdot \sigma_{\tau''s''} \Pi_{\tau''s''}^{cc}(\mathbf{q}, \nu_n) \sigma_{s''\tau''} \cdot \sigma_{\tau''s''} \Pi_{\tau''s''}^{ff}(\nu_n) \mathcal{V}_{s''\tau''; s'\tau'}^{ff}.
\end{aligned} \tag{3.8c}$$

The various polarization (bubble) diagrams are defined as convolutions of

the system becomes unstable to local singlet formation. As  $T \rightarrow T_K$  from above, the  $J^{00}$  coupling is renormalized to infinity, and  $\langle \hat{\chi}^0 \rangle$  acquires a nonzero expectation value. This is the hybridized Kondo insulator state that we discussed in Chapter 2.

The RKKY coupling is also diagonal in the static limit:

$$\mathcal{R}^{\mu\nu}(\mathbf{q}) = \delta^{\mu\nu} \left( 0 \quad \frac{(-J^2/2)\Pi_{\perp}^{cc}(\mathbf{q})}{1-J^2\Pi_{\perp}^{cc}(\mathbf{q})\Pi_{\perp}^{ff}} \quad \frac{(-J^2/2)\Pi_{\parallel}^{cc}(\mathbf{q})}{1-J^2\Pi_{\parallel}^{cc}(\mathbf{q})\Pi_{\parallel}^{ff}} \quad \frac{(-J^2/2)\Pi_{\parallel}^{cc}(\mathbf{q})}{1-J^2\Pi_{\parallel}^{cc}(\mathbf{q})\Pi_{\parallel}^{ff}} \right)^{\mu} . \quad (3.16)$$

Since  $\Pi^{cc} > 0$  and  $\Pi^{ff} > 0$ , there are potential RKKY instabilities in all the spin channels ( $\mu = 1, 2, 3$ ). These instabilities occur when

$$J^2\Pi_{\perp}^{cc}(\mathbf{Q})\Pi_{\perp}^{ff} = 1 \quad \text{and} \quad J^2\Pi_{\parallel}^{cc}(\mathbf{Q})\Pi_{\parallel}^{ff} = 1. \quad (3.17)$$

Equations (3.17) define the Néel temperatures  $T_{N\perp}$  and  $T_{N\parallel}$ , respectively. When  $T < T_{N\perp}$  and  $T < T_{N\parallel}$ , the divergence of the RKKY coupling leads to antiferromagnetic order  $\langle \hat{S}_j^1 \cos \theta + \hat{S}_j^2 \sin \theta \rangle \sim e^{i\mathbf{Q}\cdot\mathbf{r}_j}$  (perpendicular to the field) and  $\langle \hat{S}_j^3 \rangle \sim e^{i\mathbf{Q}\cdot\mathbf{r}_j}$  (parallel to the field).

Before we can determine the Kondo and Néel temperatures, we must first compute the various polarization bubbles. As a simple approximation, we impose the Brillouin zone nesting by hand ( $\epsilon_{\mathbf{k}+\mathbf{Q}} = -\epsilon_{\mathbf{k}}$ ), and assume a flat density of states

$$D(\omega) = \frac{1}{N} \sum_{\mathbf{k}} \delta(\omega - \epsilon_{\mathbf{k}}) = \frac{1}{W}. \quad (3.18)$$

The  $cf$  and  $cc$  polarization functions are given by the energy integrals

$$\begin{aligned} \Pi_{\parallel}^{cf} &= \frac{1}{2W} \int_{-W/2}^{W/2} \frac{d\epsilon}{\epsilon} \frac{\sinh(\epsilon/2T)}{\cosh[(\epsilon - B/2)/2T] \cosh(B/4T)} \\ \Pi_{\perp}^{cf} &= \frac{1}{2W} \int_{-W/2}^{W/2} \frac{d\epsilon}{\epsilon - B} \frac{\sinh[(\epsilon - B)/2T]}{\cosh[(\epsilon - B/2)/2T] \cosh(B/4T)} \\ \Pi_{\parallel}^{cc}(\mathbf{Q}) &= \frac{1}{4W} \int_{-W/2}^{W/2} \frac{d\epsilon}{\epsilon} \frac{\sinh(\epsilon/T)}{\cosh^2(\epsilon/2T) + \sinh^2(B/4T)} \\ \Pi_{\perp}^{cc}(\mathbf{Q}) &= \frac{1}{4W} \int_{-W/2}^{W/2} \frac{d\epsilon}{\epsilon} \tanh[(\epsilon - B/2)/2T]. \end{aligned} \quad (3.19)$$

The  $ff$  polarization functions are

$$\Pi_{\parallel}^{ff} = \frac{1}{4T \cosh^2(|B|/4T)} \quad \text{and} \quad \Pi_{\perp}^{ff} = \frac{\tanh(|B|/4T)}{|B|}. \quad (3.20)$$

Solving for the temperature dependence of the integrals in Eq. (3.19) allows us to determine the values of  $T_K$ ,  $T_{N\perp}$ , and  $T_{N\parallel}$  that satisfy Eqs. (3.15) and (3.17). In Fig. 3-3, these characteristic temperatures are plotted as a

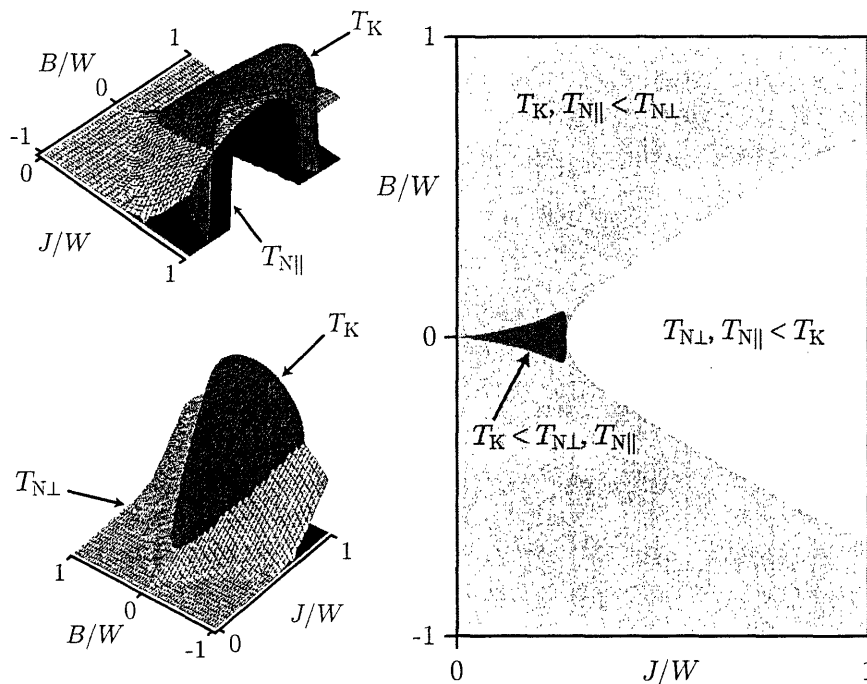


Figure 3-3: (Left) The critical temperatures  $T_K$ ,  $T_{N\perp}$ , and  $T_{N\parallel}$  are plotted as surfaces over the  $J$ - $B$  plane. Two views are given, rotated 90 degrees from one another. (Right) The plot indicates three regimes in which different temperature scales dominate. These roughly correspond to (light grey) Kondo singlet, (medium grey) canted antiferromagnetic, and (dark grey) isotropic antiferromagnetic behaviour.

function of the Kondo coupling and magnetic field. We find that  $T_{N\perp}$  is the dominant temperature scale at large fields, even for  $J > J_c$ . This suggests that the Kondo insulator is unstable to transverse staggered magnetic order above some critical field.

### 3.4 Spin Wave Theory

Since the charge excitations of the half-filled KLM are gapped, its Hilbert space breaks into distinct low- and high-energy sectors. An effective model of the low-energy spin degrees of freedom can be found by projecting the Hamiltonian onto the pure spin sector and allowing higher order virtual transitions into the charge sector to induce interaction terms. (See Appendix A.1.) Keeping only the interactions arising from second order processes gives

$$\hat{H}^{\text{eff}} = \sum_i \left[ J \hat{T}_i \cdot \hat{S}_i - B(\hat{T}_i^3 + \hat{S}_i^3) \right] + J' \sum_{\langle ij \rangle} \hat{T}_i \cdot \hat{T}_j. \quad (3.21)$$

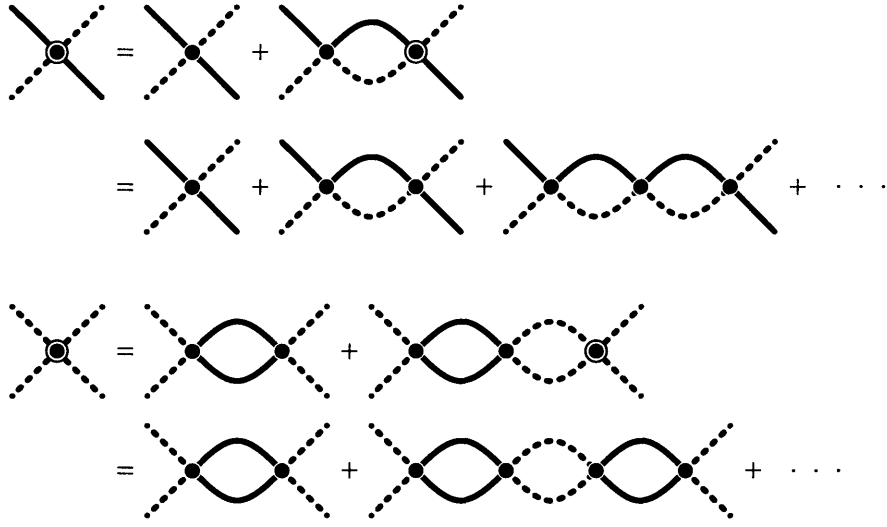


Figure 3-2: The diagrammatic equations for (top)  $\mathcal{V}^{cf}$  and (bottom)  $\mathcal{V}^{ff}$  are shown. The solid and dashed lines denote the bare Green's function for the  $c$  and  $f$  fermions. The unadorned dot represents the bare interaction.

the bare single-particle propagators:

$$\Pi_{sr}^{cf}(\nu_n) = \frac{1}{N} \sum_{\mathbf{k}} \frac{f(\epsilon_{\mathbf{k}} - sB/2) - f(-rB/2)}{i\nu_n - \epsilon_{\mathbf{k}} + (s-r)B/2} \quad (3.9a)$$

$$\Pi_{sr}^{cc}(\mathbf{q}, \nu_n) = \frac{1}{N} \sum_{\mathbf{k}} \frac{f(\epsilon_{\mathbf{k}+\mathbf{q}} - sB/2) - f(\epsilon_{\mathbf{k}} - rB/2)}{i\nu_n - \epsilon_{\mathbf{k}+\mathbf{q}} + \epsilon_{\mathbf{k}} + (s-r)B/2} \quad (3.9b)$$

$$\Pi_{sr}^{ff}(\nu_n) = \frac{f(-sB/2) - f(-rB/2)}{i\nu_n + (s-r)B/2}. \quad (3.9c)$$

Since the  $f$  electrons are dispersionless, we find that  $\Pi_{ij}^{cf} \sim \Pi_{ij}^{ff} \sim \delta_{ij}$ . Hence, their Fourier transforms, Eqs. (3.9a) and (3.9c), are  $\mathbf{q}$  independent. Equation (3.9b) is strongly peaked around  $\mathbf{q} = \mathbf{Q}$  due to the nesting of the Fermi surface.

Equations (3.8) can be formally solved to give

$$\mathcal{V}_{sr;s'r'}^{cf}(\nu_n) = -\frac{J}{2} \left[ \delta_{ss''} \delta_{r'r''} - \frac{J}{2} \boldsymbol{\sigma}_{ss''} \cdot \boldsymbol{\sigma}_{r''r} \Pi_{s''r''}^{cf}(\nu_n) \right]^{-1} \boldsymbol{\sigma}_{s''r'} \cdot \boldsymbol{\sigma}_{s'r''} \quad (3.10)$$

and

$$\mathcal{V}_{sr;s'r'}^{ff} = -\frac{J^2}{4} \left[ \delta_{ss''} \delta_{r'r''} - \frac{J^2}{4} \boldsymbol{\sigma}_{sr} \cdot \boldsymbol{\sigma}_{r''s''} \Pi_{r''s''}^{cc}(\mathbf{q}, \nu_n) \boldsymbol{\sigma}_{s''r''} \cdot \boldsymbol{\sigma}_{r''s''} \right. \\ \left. \Pi_{r''s''}^{ff}(\nu_n) \right]^{-1} \boldsymbol{\sigma}_{s''r''} \cdot \boldsymbol{\sigma}_{r''s''} \Pi_{r''s''}^{cc}(\mathbf{q}, \nu_n) \boldsymbol{\sigma}_{s''r''} \cdot \boldsymbol{\sigma}_{s'r''}, \quad (3.11)$$

where the four-index object  $[\dots]_{ss';r'r'}^{-1}$  is inverted as if it were a matrix of

two  $SU(2) \otimes SU(2)$  indices. The result for  $\mathcal{V}^{cc}$  is the same as Eq. (3.11) but with the  $c$  and  $f$  labels switched. Computing these matrix inversions and contracting their spin labels via Eq. (3.7) yields the Kondo

$$J^{\mu\nu}(\nu_n) = \begin{pmatrix} \frac{(-3J/4)(4+2J\Pi_{\parallel}^{cf'})}{4-4J\Pi_{\parallel}^{cf'}-3J^2|\Pi_{\parallel}^{cf}|^2} & 0 & 0 & \frac{(-3J/4)(2iJ\Pi_{\parallel}^{cf''})}{4-4J\Pi_{\parallel}^{cf'}-3J^2|\Pi_{\parallel}^{cf}|^2} \\ 0 & \frac{J}{4} \frac{4+2J\Pi_{\perp}^{cf'}}{|2+J\Pi_{\perp}^{cf}|^2} & \frac{J}{4} \frac{-2J\Pi_{\perp}^{cf''}}{|2+J\Pi_{\perp}^{cf}|^2} & 0 \\ 0 & \frac{J}{4} \frac{+2J\Pi_{\perp}^{cf''}}{|2+J\Pi_{\perp}^{cf}|^2} & \frac{J}{4} \frac{4+2J\Pi_{\perp}^{cf'}}{|2+J\Pi_{\perp}^{cf}|^2} & 0 \\ \frac{(J/4)(6iJ\Pi_{\parallel}^{cf''})}{4-2J\Pi_{\parallel}^{cf'}-3J^2|\Pi_{\parallel}^{cf}|^2} & 0 & 0 & \frac{(J/4)(4-6J\Pi_{\parallel}^{cf'})}{4-2J\Pi_{\parallel}^{cf'}-3J^2|\Pi_{\parallel}^{cf}|^2} \end{pmatrix} \quad (3.12)$$

and RKKY

$$\mathcal{R}^{\mu\nu}(\mathbf{q}, \nu_n) = \begin{pmatrix} 0 & 0 & 0 & 0 \\ 0 & -\frac{J^2}{2} \frac{\Pi_{\perp}^{cc'} - J^2 |\Pi_{\perp}^{cc}|^2 \Pi_{\perp}^{ff'}}{|1 - J^2 \Pi_{\perp}^{cc} \Pi_{\perp}^{ff}|^2} & \frac{iJ^2}{2} \frac{\Pi_{\perp}^{cc''} + J^2 |\Pi_{\perp}^{cc}|^2 \Pi_{\perp}^{ff''}}{|1 - J^2 \Pi_{\perp}^{cc} \Pi_{\perp}^{ff}|^2} & 0 \\ 0 & -\frac{iJ^2}{2} \frac{\Pi_{\perp}^{cc''} + J^2 |\Pi_{\perp}^{cc}|^2 \Pi_{\perp}^{ff''}}{|1 - J^2 \Pi_{\perp}^{cc} \Pi_{\perp}^{ff}|^2} & -\frac{J^2}{2} \frac{\Pi_{\perp}^{cc'} - J^2 |\Pi_{\perp}^{cc}|^2 \Pi_{\perp}^{ff'}}{|1 - J^2 \Pi_{\perp}^{cc} \Pi_{\perp}^{ff}|^2} & 0 \\ 0 & 0 & 0 & \frac{(-J^2/2)\Pi_{\parallel}^{cc'}}{1 - J^2 \Pi_{\parallel}^{cc'} \Pi_{\parallel}^{ff'}} \end{pmatrix} \quad (3.13)$$

couplings. The prime and double-prime are used to denote the real and imaginary parts of the polarization functions; *i.e.*,  $\Pi = \Pi' + i\Pi''$ .

### 3.3 What Physics Wins Out Where

Components of  $J^{\mu\nu}(\nu_n)$  and  $R^{\mu\nu}(\mathbf{q}, \nu_n)$  may be renormalized to very large values if any of the denominators in Eqs. (3.12) and (3.13) are small. The only unbounded components, however, are the static ones ( $\nu_n = 0$ ), since their purely real denominators have the potential to obtain a zero value.

In the  $\nu_n = 0$  limit, the off-diagonal terms in Eq. (3.12) vanish, so the Kondo coupling is given by

$$J^{\mu\nu} = \delta^{\mu\nu} \left( \frac{-3J/4}{1-(3J/2)\Pi_{\parallel}^{cf}} \quad \frac{J/4}{1+(J/2)\Pi_{\perp}^{cf}} \quad \frac{J/4}{1+(J/2)\Pi_{\perp}^{cf}} \quad \frac{J/4}{1+(J/2)\Pi_{\parallel}^{cf}} \right)^{\mu}. \quad (3.14)$$

Since  $J > 0$  and  $\Pi^{cf} > 0$ , the triplet components ( $\mu = 1, 2, 3$ ) are always bounded. The singlet component ( $\mu = 0$ ), however, diverges when

$$\frac{3J}{2}\Pi_{\parallel}^{cf} = 1. \quad (3.15)$$

This Stoner-like criterion defines the Kondo temperature  $T_K$ , below which

The resulting Hamiltonian describes a lattice of spin pairs  $(\hat{S}_i, \hat{T}_i)$ , whose net moment is coupled to a magnetic field. The spins interact onsite with the Kondo coupling  $J$  and between neighbouring sites with an antiferromagnetic exchange coupling  $J' = 4t^2/\Delta > 0$ . Here,  $\Delta$  is the difference between the lowest energy level in the spin and charge sectors. Approximating  $J'$  by its value in the atomic limit yields

$$J' = \frac{4t^2}{\Delta} \sim \begin{cases} \frac{8t^2}{3J-2|B|} & \text{if } |B| < J, \\ \frac{8t^2}{2|B|-J} & \text{if } |B| > J. \end{cases} \quad (3.22)$$

When  $J = \infty$  ( $|B| = \infty$ ), the ground state consists of a singlet (triplet) pair at each site, and the excitations are local. Away from these extreme limits, the system supports additional *collective* spin excitations, which can be studied by a spin wave analysis of Eq. (3.21).

In zero field, we find three degenerate magnon modes with dispersion

$$\omega_{\mathbf{q}} = \sqrt{J^2 + JJ'\gamma_{\mathbf{q}}/2} = \sqrt{J^2 + (4t^2/3)\gamma_{\mathbf{q}}}. \quad (3.23)$$

The  $\mathbf{q}$  dependence is inherited from  $\gamma_{\mathbf{q}} = \sum_{l=1}^d \cos q^l$ , so the lowest energy magnon occurs at the antiferromagnetic wavevector  $\mathbf{Q} = (\pi, \dots, \pi)$ . Around this minimum, Eq. (3.23) has the form

$$\omega_{\mathbf{q}+\mathbf{Q}} = \sqrt{J^2 - J_c^2(1 - |\mathbf{q}|^2/z)}, \quad (3.24)$$

where  $J_c = \sqrt{2z/3}t$  and  $z$  is the coordination number of the lattice. This is derived by expanding  $\gamma_{\mathbf{q}+\mathbf{Q}} \approx \frac{1}{2}(-z + |\mathbf{q}|^2)$  in small  $\mathbf{q}$ .

The magnons in the Kondo singlet phase ( $J > J_c$ ) are always gapped. As  $J$  approaches  $J_c$  from above, the spin gap  $\Delta_s = \sqrt{J^2 - J_c^2}$  decreases and the dispersion around  $\mathbf{Q}$  becomes ever more sharp. Right at the critical coupling, the spin gap vanishes and the dispersion becomes linear:  $\omega_{\mathbf{q}+\mathbf{Q}} \rightarrow J_c|\mathbf{q}|/\sqrt{z}$  as  $J \rightarrow J_c$ . See Fig. 3-4(a).

When  $B \neq 0$ , the two transverse modes ( $\omega_{\mathbf{q}}^{\perp}$ ) split off from the longitudinal mode ( $\omega_{\mathbf{q}}^{\parallel}$ ). The latter always remains gapped. The transverse modes, however, descend as a function of the applied field:

$$\omega_{\mathbf{q}}^{\perp} = \omega_{\mathbf{q}}^{\parallel} - |B| = \sqrt{J^2 + JJ'\gamma_{\mathbf{q}}/2} - |B|, \quad (3.25)$$

Around its minimum, Eq. (3.25) behaves as  $\omega_{\mathbf{q}+\mathbf{Q}}^{\perp} \approx \Delta_s + v|\mathbf{q}|^2$ . It shows quadratic dispersion above a spin gap

$$\Delta_s = J\sqrt{1 - \frac{2t^2z}{J(3J-2|B|)}} - |B|. \quad (3.26)$$

As the field strength is ramped up,  $\Delta_s$  shrinks until it eventually vanishes at some lower critical field  $B_{c1}$ . When  $|B| = B_{c1}$ , the  $\omega_{\mathbf{Q}}^{\perp}$  spin waves have

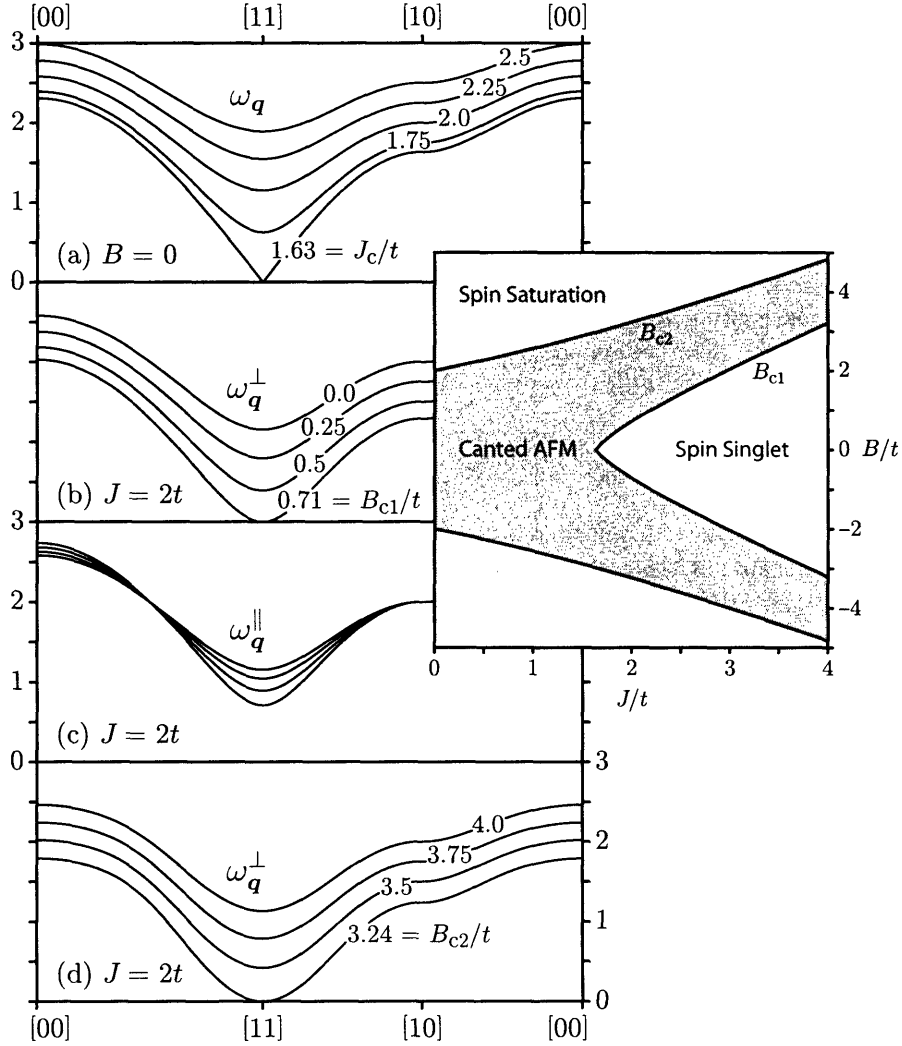


Figure 3-4: The dispersion of the magnon bands is plotted in units of  $t$  along high-symmetry lines in the ( $d = 2$ ) Brillouin zone. In panel (a), the values of  $J/t$  are labelled. At the critical coupling, the gap vanishes and the dispersion becomes linear about  $\mathbf{q} = \mathbf{Q}$ . In panels (b) and (d), the values of  $B/t$  are labelled. The spin gaps vanish at the critical fields  $B_{c1}$  and  $B_{c2}$ . The bands in panel (c) correspond to the same field values as those in panel (b). The sideset plot shows the complete phase diagram.

zero energy cost and begin to proliferate. In this way, staggered magnetic order perpendicular to the field is established.

Coming from the large field limit, the spins are fully polarized and cannot support spin excitations directed along the field. What remains are the two transverse modes with dispersion

$$\omega_{\mathbf{q}}^{\perp} = \frac{1}{2} \left[ 2|B| - J + \frac{1}{2} J' \gamma_{\mathbf{q}} - \sqrt{J^2 + \frac{1}{4} (J' \gamma_{\mathbf{q}})^2} \right]. \quad (3.27)$$

Again, these transverse modes are quadratic around their minimum at  $\mathbf{Q}$ ,  $\omega_{\mathbf{q}+\mathbf{Q}}^{\perp} \approx \Delta_s + v|\mathbf{q}|^2$ . The spin gap is given by

$$\Delta_s = \frac{(2|B| - J)^2 - 2zt^2 - \sqrt{J^2(2|B| - J)^2 + 4z^2t^2}}{2(2|B| - J)}. \quad (3.28)$$

The gap shrinks as the applied field is ramped down and disappears when  $|B|$  drops below the upper critical field  $B_{c2} = \frac{1}{2}(J + \sqrt{J^2 + 6J_c^2})$ .

Thus, whenever  $B_{c1} < |B| < B_{c2}$ ,  $\omega_{\mathbf{q}}^{\perp}$  is negative at  $\mathbf{q} = \mathbf{Q}$ . The lines  $|B| = B_{c1}$  and  $|B| = B_{c2}$ , plotted in Fig. 3-4, are phase boundaries to the antiferromagnetic region.



## Chapter 4

# Numerical Results

### 4.1 Outline

Let us briefly recapitulate. The unusual properties of the heavy fermion materials are the result of strong interactions between their mobile  $s$ ,  $p$ ,  $d$  and tightly-bound  $f$  electrons. The KLM is thought to provide an approximate description of such materials. The mean field picture of Chapter 2 describes a broad conduction band, intersected by a nearly flat band of renormalized core levels. Hybridization produces a band structure with extremely shallow dispersion near the band edge. When the chemical potential lies below the hybridization gap, the system is a metal characterized by a very large effective electron mass. When the chemical potential lies inside the gap, the system is an insulator.

Heavy fermion systems often live at the edge of magnetic instability. As we demonstrated in Chapter 3, RKKY antiferromagnetism competes with the hybridization mechanism. In zero magnetic field, the magnetism dominates at small Kondo coupling, and local singlet formation wins out only when  $J$  exceeds some critical value  $J_c$ . An applied magnetic field will interfere with the singlet-RKKY competition and, if strong enough, tilt the balance in favour of the antiferromagnetism. The Zeeman term, a field  $B$  coupled to the total magnetic moment, favors triplet rather than singlet formation at each site. Accordingly, it suppresses the singlet amplitude and thus has the potential to stabilize an antiferromagnetic phase, even in the  $J > J_c$  region.

The Zeeman splitting lifts the degeneracy of the spin up and spin down bands, shifting them with respect to one another and potentially closing the charge gap. The precise evolution of the charge gap, however, depends on the interplay between the RKKY and hybridization effects.

In this chapter, we show by variational mean field and quantum Monte Carlo (QMC) calculations that, as the applied field is ramped up, the Kondo insulator ground state gives way to a canted antiferromagnetic phase. At sufficiently large fields, the localized spins become polarized, the antiferromagnetism falls off, and the system crosses over to a nearly-metallic regime

with an exponentially small charge gap. The QMC simulation, which is exact, provides an important confirmation of the mean field predictions. Our QMC efforts are closely related to the zero-field work of Capponi and Asaad [20]. A similar mean field calculation in zero field has previously been carried out by Zhang and Yu [21].

## 4.2 Variational Mean Field

A comprehensive variational calculation of the ground state must incorporate all of the following: hybridization between the  $c$  and  $f$  bands (singlet formation), antiferromagnetism transverse to the field, and magnetism parallel to the field. A suitable trial wavefunction is the ground state of the variational Hamiltonian

$$\begin{aligned} \hat{H}_{\text{var}} = & -t \sum_{\langle ij \rangle} (c_i^\dagger c_j + c_j^\dagger c_i) - \sum_i (V^* f_i^\dagger c_i + V c_i^\dagger f_i) \\ & - \frac{M_f}{2} \sum_i (-1)^i c_i^\dagger \sigma^1 c_i - \frac{B_f}{2} \sum_i c_i^\dagger \sigma^3 c_i \\ & - \frac{M_c}{2} \sum_i (-1)^{i+1} f_i^\dagger \sigma^1 f_i - \frac{B_c}{2} \sum_i f_i^\dagger \sigma^3 f_i. \end{aligned} \quad (4.1)$$

It contains five symmetry-breaking terms, controlled by the variational parameters  $\{V_m\} = \{V, M_c, M_f, B_c, B_f\}$ . The variational ground state energy  $\mathcal{U}\{\{V_m\}\}$  is the expectation value of the exact Hamiltonian evaluated in the ground state of  $\hat{H}_{\text{var}}$ . For every value of the physical parameters  $J$  and  $B$ , the set  $\{V_m\}$  is chosen such that  $\mathcal{U}$  is minimized. Figure 4-1 shows one  $B = 0$  and three constant- $J$  slices of data from the variational calculation. Figure 4-2 gives the complete phase diagram.

The top panel of Fig. 4-1 shows the zero-field case. A critical value of the Kondo coupling  $J_c \approx 1.6t$  separates the Kondo singlet and antiferromagnetic phases. For  $J > J_c$ , the system is hybridized. Below  $J_c$ , the hybridization dies out and the  $c$  and  $f$  moments order antiferromagnetically. The  $c$ -electron magnetism is relatively weak, but the  $f$  electrons exhibit their full  $S=1/2$  moment. In a very small window around  $J_c$ , hybridization and antiferromagnetism coexist. The charge gap, which is nonzero for all  $J$ , does not pass smoothly through the transition. It rises sharply with the initial onset of the antiferromagnetism.

The Kondo singlet regime is characterized by a nonzero hybridization ( $V \neq 0$ ) and the absence of magnetic order ( $M_{c,f} = 0$ ,  $B_{c,f} = B$ ). The energy levels, given by

$$E_{\mathbf{k}s}^n = \frac{1}{2} \left( \varepsilon_{\mathbf{k}} - sB + n \sqrt{\varepsilon_{\mathbf{k}}^2 + 4V^2} \right) \quad (4.2)$$

with  $\varepsilon_{\mathbf{k}} = -2t \sum_{l=1}^d \cos k^l$  (for a  $d$ -hypercubic lattice), are parameterized by

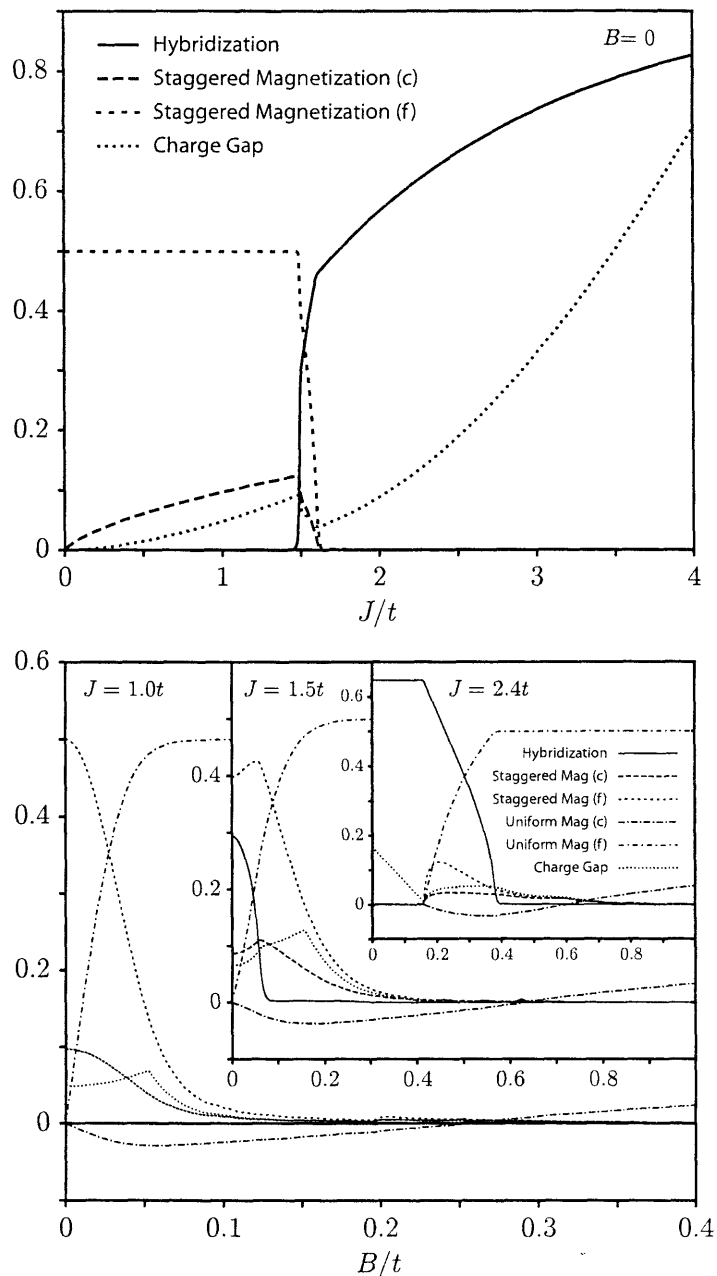


Figure 4-1: The variational mean field result is computed at  $T = 0$  on the square lattice. The hybridization  $\langle f^\dagger c \rangle$ , the staggered magnetization  $\langle (-1)^i \frac{1}{2} c_i^\dagger \sigma^1 c_i \rangle$  and  $\langle (-1)^i \frac{1}{2} f_i^\dagger \sigma^1 f_i \rangle$ , the uniform magnetization  $\langle \frac{1}{2} c_i^\dagger \sigma^3 c_i \rangle$  and  $\langle \frac{1}{2} f_i^\dagger \sigma^3 f_i \rangle$ , and the charge gap  $\Delta_c$  are plotted (top) as a function of  $J$  in zero field and (bottom) as a function of  $B$  for three values of  $J$  ( $J < J_c$ ,  $J \sim J_c$ , and  $J > J_c$ ).

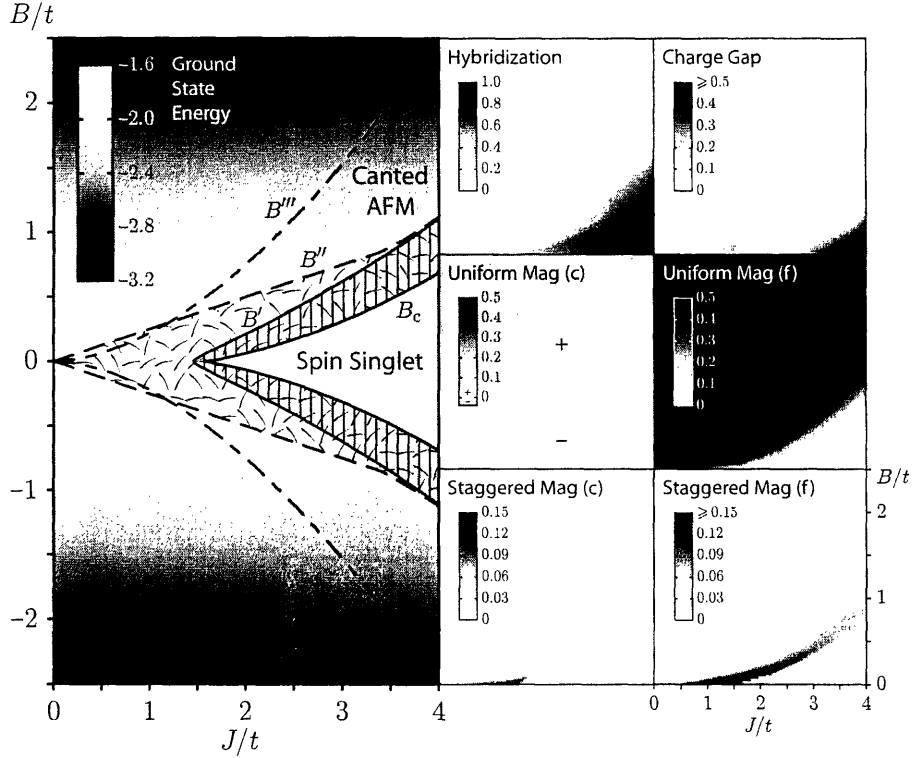


Figure 4-2: (Left panel)  $B_c$  is a second-order transition;  $B'$ ,  $B''$ , and  $B'''$  are crossovers. The spin singlet phase has hybridization order only. Antiferromagnetic and hybridization order coexist in the striped region. The stippling indicates where the electron moments are directed opposite to the  $B$  field. For  $|B| > B'''$ , the charge gap is exponentially suppressed. Along the line  $J < J_c$ ,  $B = 0$ , the system exhibits uncanted Néel order. (Rightmost six panels)  $\langle f^\dagger c \rangle$ ,  $\Delta_c$ ,  $\langle \frac{1}{2} c_i^\dagger \sigma^3 c_i \rangle$ ,  $\langle \frac{1}{2} f_i^\dagger \sigma^3 f_i \rangle$ ,  $\langle (-1)^i \frac{1}{2} c_i^\dagger \sigma^1 c_i \rangle$ , and  $\langle (-1)^i \frac{1}{2} f_i^\dagger \sigma^1 f_i \rangle$  are plotted in the upper half of the phase diagram.

the band index  $n = \pm$  and spin projection  $s = \pm$  ( $\uparrow, \downarrow$ ). In the  $B = 0$  case (inset Fig. 4-6), the band separation takes its minimum,  $2V$ , on the surface  $|k^1| + \dots + |k^d| = \pi$  ( $\varepsilon_{\mathbf{k}} = 0$ ). The band gap, however, is indirect: promoting a quasiparticle from the top of the lower band [at  $\mathbf{Q} = (\pi, \dots, \pi)$ ] to an arbitrary momentum state in the upper band costs  $\omega^{\text{qp}}(\mathbf{k}) = E_{\mathbf{k}}^+ - E_{\mathbf{Q}}^-$ ; around its minimum,  $\omega^{\text{qp}}(\mathbf{k}) \approx 2\Delta_K + (1/2m^*)|\mathbf{k}|^2$ , where  $4V^2 = 2\Delta_K(2\Delta_K + W)$  and  $W = 4dt$  is the noninteracting bandwidth. The Kondo energy  $\Delta_K (< V)$  sets the scale for both the charge gap ( $\Delta_c = 2\Delta_K$ ) and the ground state energy shift ( $\mathcal{U}[V] - \mathcal{U}[0] = -\Delta_K$ ).

Now consider  $B \neq 0$ . Throughout the singlet phase,  $V$  is independent of the applied field (see the  $J = 2.4t$  inset of Fig. 4-1). Thus, according to Eq. (4.2), the hybridized bands simply shift with respect to one another

in response to the applied field and the charge gap decreases monotonically:  $\Delta_c = 2\Delta_K - |B|$ . Before the charge gap closes completely, however, magnetic order sets in ( $|B| = B_c \lesssim 2\Delta_K$ ). The localized spins develop a uniform moment directed with the field and a staggered moment perpendicular to it. The electrons do the same but are “effectively diamagnetic,” canting *against* the field. As  $|B|$  increases,  $V$  begins to fall off and vanishes at  $|B| = B'$ . When  $|B| = B'' \approx \max(J/4, B')$ ,  $\langle \frac{1}{2}c_i^\dagger \sigma^3 c_i \rangle$  changes sign. When  $|B| \sim B'''$ , the charge gap collapses to an exponentially small value; at this point, the local spins have saturated and the antiferromagnetism is only weakly supported by virtual spin flips. In a system without perfect nesting of the Fermi surface, the antiferromagnetism would die out completely, making  $B'''$  a transition to a true metallic state: the conduction electrons would decouple from the quenched local spins and propagate freely.

Naively, one might have expected the charge gap to close at  $|B| = 2\Delta_K$ . As shown in Fig. 4-3, however, the incipient antiferromagnetism prevents the level crossing by mixing the  $(c, f)_{\mathbf{k}\uparrow}$  and  $(c, f)_{\mathbf{k}+\mathbf{Q}\downarrow}$  bands. The charge gap has the behavior shown in Fig. 4-2 (sideset, top-right): it decreases linearly with  $|B|$  in the singlet phase, resurges in the canted antiferromagnetic phase, and finally collapses in the nearly-metallic regime.

An important feature of the charge gap’s evolution is that it does not collapse at the center of the reduced (mod  $\mathbf{Q}$ ) Brillouin zone. As the system is driven through the antiferromagnetic phase ( $B_c < |B| \lesssim B'''$ ), the gap migrates from  $\mathbf{k} = 0$  out to the zone edge. A consequence is that the hybridization energy and not the Kondo energy determines the robustness of the insulating state. This leads to a separation of energy scales: the spin gap closes when  $|B| \sim 2\Delta_K$ , whereas the charge gap collapses when  $|B| \sim \sqrt{2\Delta_K W}$ .

### 4.3 Quantum Monte Carlo

The partition function of the system can be written as

$$Z = \int d\eta d\bar{\eta} e^{\bar{\eta}\eta} \langle \eta | \prod_{l=1}^L \left( \hat{P} \int d\chi_l e^{-\epsilon \hat{H}[\chi_l]} \right) | -\eta \rangle, \quad (4.3)$$

where  $l$  labels the slices of discretized imaginary time ( $\epsilon = \beta/L$ ), the Grassman vector  $\eta = (c_\uparrow \ c_\downarrow \ f_\uparrow \ f_\downarrow)$  holds the four fermionic species, and the operator  $\hat{P}$  projects out states that violate the single occupancy requirement of the  $f$  electrons.  $\hat{H}[\chi_l]$  is bilinear and related to the Hamiltonian by a Hubbard-Stratonovich decomposition of the Kondo interaction in the hybridization channel.

Replacing  $e^{-\epsilon \hat{H}[\chi_l]}$  by its coherent state representation puts a set of Grassman states at each time slice  $l$ . The matrix elements  $\langle \eta_l | \hat{P} | \eta_{l+1} \rangle$  can be handled by introducing a U(1) gauge field  $z_{l,l+1}$  living on the temporal

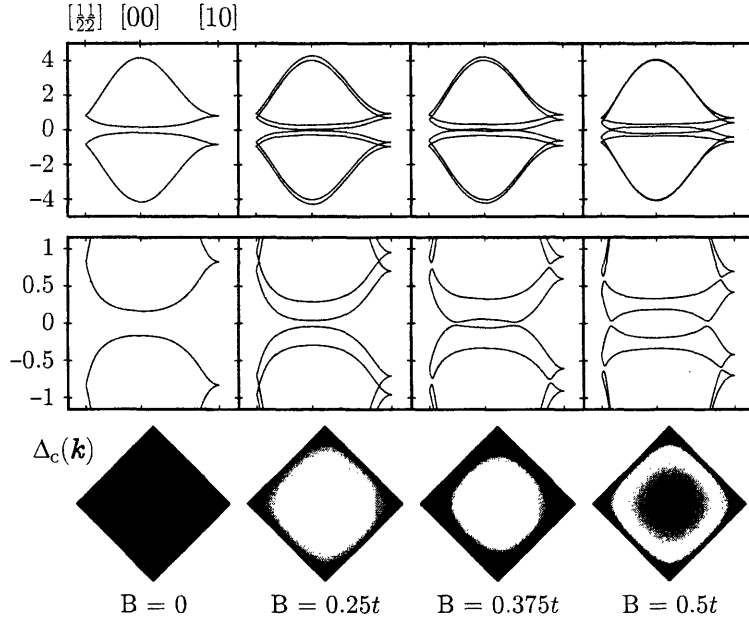


Figure 4-3:  $J/t = 3$ ,  $B_c/t \doteq 0.323$ . (Top row) Mean field band structure, folded into the reduced Brillouin zone, as a function of applied magnetic field. (Middle) Same, magnified to show the evolution of the band gap. (Bottom) The greyscale (white–black  $\leftrightarrow$  0–0.5t) indicates the wavevector-dependent gap magnitude. For  $|B| < B_c$ ,  $\Delta_c(\mathbf{k})$  is a minimum at  $\mathbf{k} = 0$ , and for  $|B| > B_c$ , at an expanding ring of points.

links. Integrating out the Grassman fields gives  $Z = \int d\chi dz e^{-S[\chi, z]}$ , where  $S = \sum_{i, k} |\chi_{i, k}|^2 - \text{tr} \ln M[\chi, z]$  is the action of a lattice gauge theory in  $d+1$  dimensions. By exploiting the particle-hole symmetry of the Hamiltonian and the bipartite nature of the lattice, it is possible to transform to a gauge in which  $M$  is positive definite. Specifically, under  $c_{i\uparrow} \rightarrow c_{i1}$ ,  $c_{i\downarrow} \rightarrow (-1)^i \bar{c}_{i2}$ ,  $f_{i\uparrow} \rightarrow f_{i1}$ ,  $f_{i\downarrow} \rightarrow (-1)^{i+1} \bar{f}_{i2}$ , the gauge theory acquires a block diagonal form,  $M = \text{diag}(M_1, M_2)$  with  $M_2 = M_1^\dagger$ , so that  $\det M = |\det M_1|^2$ . Since the total magnetic moment transforms as  $\sum_i (\bar{c}_i \sigma^3 c_i + \bar{f}_i \sigma^3 f_i) \rightarrow \sum_i \sum_{s=1,2} (\bar{c}_{is} c_{is} + \bar{f}_{is} f_{is})$ , the positivity of  $M$  is preserved even for  $B \neq 0$ .

A general  $n$ -particle correlation function of the form

$$Z^{-1} \int d\chi dz M_{i_1 i'_1; \tau_1 \tau'_1}^{-1} \cdots M_{i_n i'_n; \tau_n \tau'_n}^{-1} e^{-S[\chi, z]} \quad (4.4)$$

is evaluated via stochastic sampling [22] by interpreting  $\mathcal{P}[\chi, z] = Z^{-1} e^{-S[\chi, z]}$  as a probability weight. (Since  $\det M > 0$ , there is no fermion sign problem.) The sampling algorithm ensures that any particular configuration  $\chi, z$  is visited with probability  $\mathcal{P}[\chi, z]$ . Thus, computing correlation functions amounts to binning and tabulating  $M_{i_i' i'_i; \tau_i \tau'_i}^{-1}$  for a large series of independent

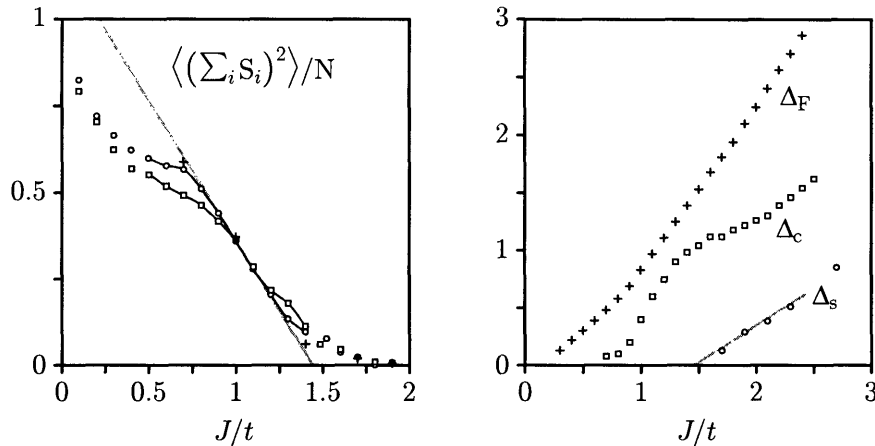


Figure 4-4: (Left) The global spin magnitude is plotted as a function of the Kondo coupling for a series of  $4 \times 4$  ( $\circ$ ),  $6 \times 6$  ( $\square$ ), and  $8 \times 8$  ( $+$ ) lattices. The finite size scaling suggests a critical value of  $J_c/t = 1.47 \pm 0.08$ . (Right) The spin gap  $\Delta_s$ , the charge gap  $\Delta_c$ , and the direct gap  $\Delta_F$  (evaluated at the Fermi wavevector of the noninteracting system). The spin gap vanishes at  $J = J_c$ . The charge gap varies continuously across the transition; it is nonzero for all values of  $J$ .

field configurations. Updates are effected by a more sophisticated version of the algorithm introduced by Blankenbecler, Scalapino, and Sugar [23]. Implementation details and other technical issues are discussed at length in Chapter 5. The reliability of our code is verified by comparison with the zero-field KLM results of Capponi and Assaad [20]. Our computed critical coupling,  $J_c/t = 1.47 \pm 0.08$ , is consistent with their value of  $1.45 \pm 0.05$ . See Fig. 4-4.

The one-particle electron Green's function  $G(\mathbf{k}, \tau) = \langle T[c_{\mathbf{k}}(0)c_{\mathbf{k}}^\dagger(\tau)] \rangle$  corresponds to  $\int d\chi dz M_{\mathbf{k};0\tau}^{-1} \mathcal{P}[\chi, z]$ . Written in terms of its spectral function  $A(\mathbf{k}, \omega)$ , the Green's function has the form of a linear functional  $G(\mathbf{k}, \tau) = \int d\omega K(\tau, \omega) A(\mathbf{k}, \omega) = \mathbf{K}[A(\mathbf{k}, \omega)]$  with kernel  $K(\tau, \omega) = e^{-\omega\tau}/(e^{-\beta\omega} + 1)$ . To extract  $A(\mathbf{k}, \omega)$ , we perform a functional inversion  $A(\mathbf{k}, \omega) = \mathbf{K}^{-1}[G(\mathbf{k}, \tau)]$ . Since the input data is noisy and incomplete, however, the inversion problem is ill-posed and must be systematically regularized. The most widely used procedure is the method of maximum entropy [24].

We employ a generalization of maximum entropy, which, rather than selecting a single most probable solution, averages (in the spirit of Ref. [25]) over a series of likely candidates. We believe that this method (to be presented in full detail in Chapter 6) does a better job of extracting fine spectral features from data of low quality (*i.e.*, having poor statistics).

Figures 4-5 and 4-6 show the zero-field spectra in the antiferromagnetic ( $J < J_c$ ) and singlet ( $J > J_c$ ) phases. In the singlet case, the spectral peaks

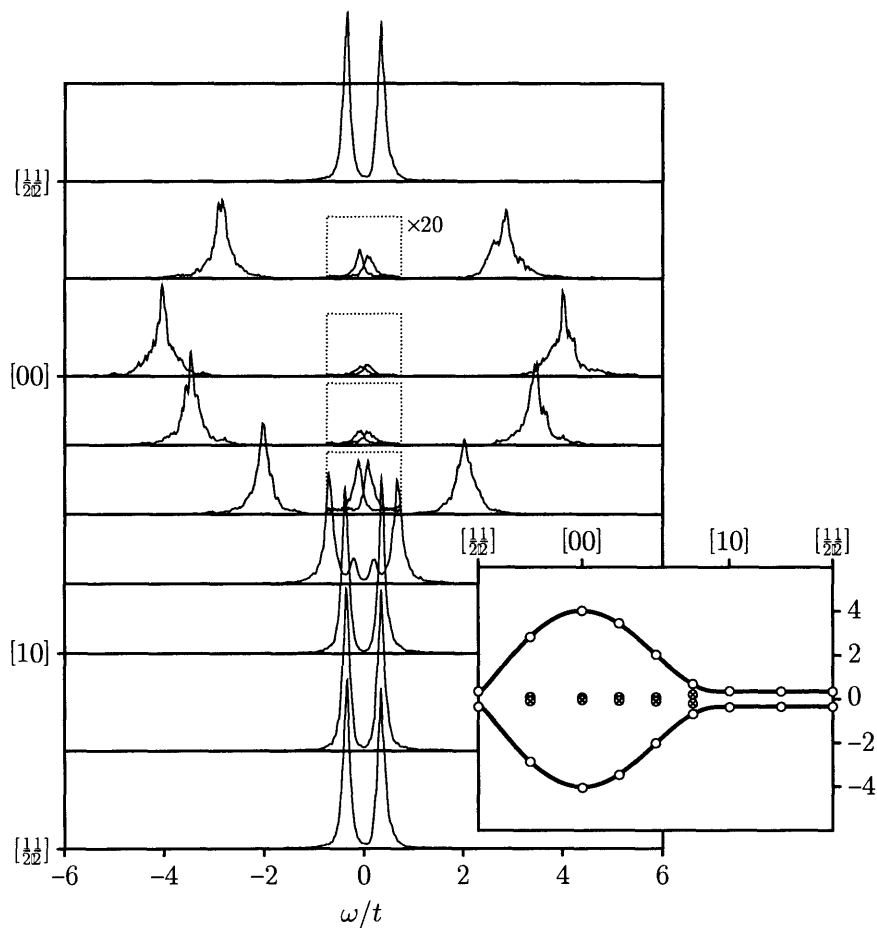


Figure 4-5: Analytically continued data from the one-particle electron Green's function for  $J/t = 1$ ,  $\beta t = 14$  on an  $8 \times 8$  lattice. Spectral functions  $A(\mathbf{k}, \omega)$  are plotted in the reduced (mod  $\mathbf{Q}$ ) Brillouing zone. (Inset) the peaks locations are superimposed on the mean field antiferromagnetic band structure with  $M_f$  chosen to fit the band splitting at  $\mathbf{k} = (\pi/2, \pi/2)$ . The dominant peaks are marked with open circles and the subsidiary peaks with crossed circles.

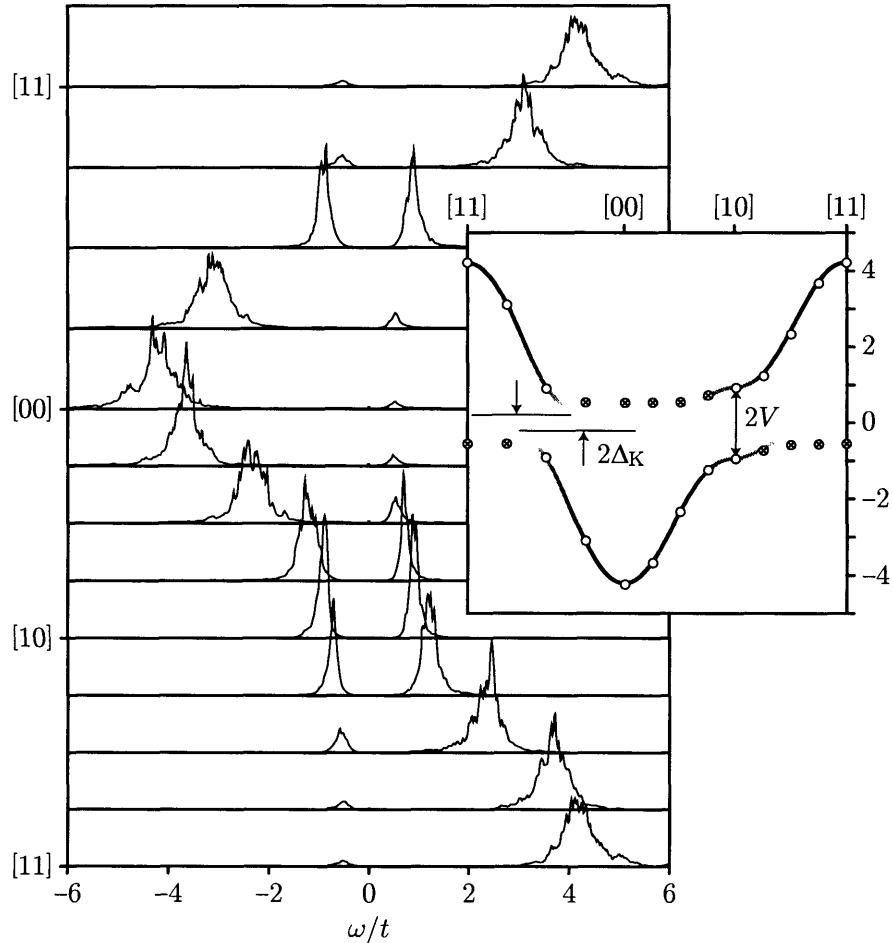


Figure 4-6: Analytically continued data from the one-particle electron Green's function for  $J/t = 1.7$ ,  $\beta t = 14$  on an  $8 \times 8$  lattice. Spectral functions  $A(\mathbf{k}, \omega)$  are plotted for wavevectors along high-symmetry lines in the Brillouin zone. (Inset) the peaks locations are superimposed on the mean field band structure [Eq. (4.2)] with  $V$  chosen to fit the band splitting at  $\mathbf{k} = (\pi, 0)$ . The dominant peaks are marked with open circles and the subsidiary peaks with crossed circles. The greyscale indicates the spectral weight (white–black  $\leftrightarrow$  0–1).

trace out two bands separated by a small gap at the chemical potential. The lower and upper bands exhibit (heavy fermion) regions of low spectral weight and nearly flat dispersion in the vicinity of  $\mathbf{k} = (\pi, \pi)$  and  $\mathbf{k} = 0$ , respectively.

QMC results confirm that the system is well-described by its mean field theory. Several signature features are observed in the simulations: a robust singlet phase ( $J > J_c$ ,  $|B| < B_c$ ), electronic moments directed against the field ( $B_c < |B| < B''$ ), transverse staggered magnetic order ( $B_c < |B| \lesssim B'''$ ), and a high-field ( $|B| \sim B'''$ ) collapse of the charge gap near the reduced zone edge.

The inset in Fig. 4-7 depicts the phase boundary between the singlet and canted antiferromagnetic phases; it also marks where  $\langle \frac{1}{2} c_i^\dagger \sigma^3 c_i \rangle$  changes sign. The main plot shows in six panels the spectral function of a spin up electron evaluated at a series of wavevectors snaking through the Brillouin zone from  $\mathbf{k} = 0$  to  $\mathbf{k} = (\pi/2, \pi/2)$ ; the panels are arranged (from bottom to top) in order of increasing distance from the zone center.

As per Eq. (4.2), the spectra exhibit a double peak structure and drift leftward (lowering energy) as  $B$  increases from zero. For small  $\mathbf{k}$ , there is a primary peak near the non-interacting particle energy  $\omega = \varepsilon_{\mathbf{k}}$  and a secondary peak near  $\omega = \Delta_K$ . The leftward drift of the secondary peak is interrupted by the growth of antiferromagnetic correlations that protect the gap. *The spectral weight rearranges by hopping over the forbidden region.* There is no weight at the chemical potential, so the system remains insulating even when  $|B| = 2\Delta_K$ .

At  $\mathbf{k} = (\pi/2, \pi/2)$ , there are two equally weighted peaks at  $\pm V$ . As  $B$  is ramped up, spectral weight from the lower peak is transferred to the upper, unoccupied peak (this accounts for  $\langle \frac{1}{2} c^\dagger \sigma^3 c \rangle < 0$ ), which grows increasingly sharper as it drifts leftward and crosses the chemical potential (fixed at  $\mu = 0$  by particle-hole symmetry). To within the numerical resolution of the simulation, the spectral weight of the lower peak is exhausted and  $A(\mathbf{k}, \omega) \rightarrow \delta(\omega - B/2)$ , its free electron value; the antiferromagnetic correlations vanish here as well.

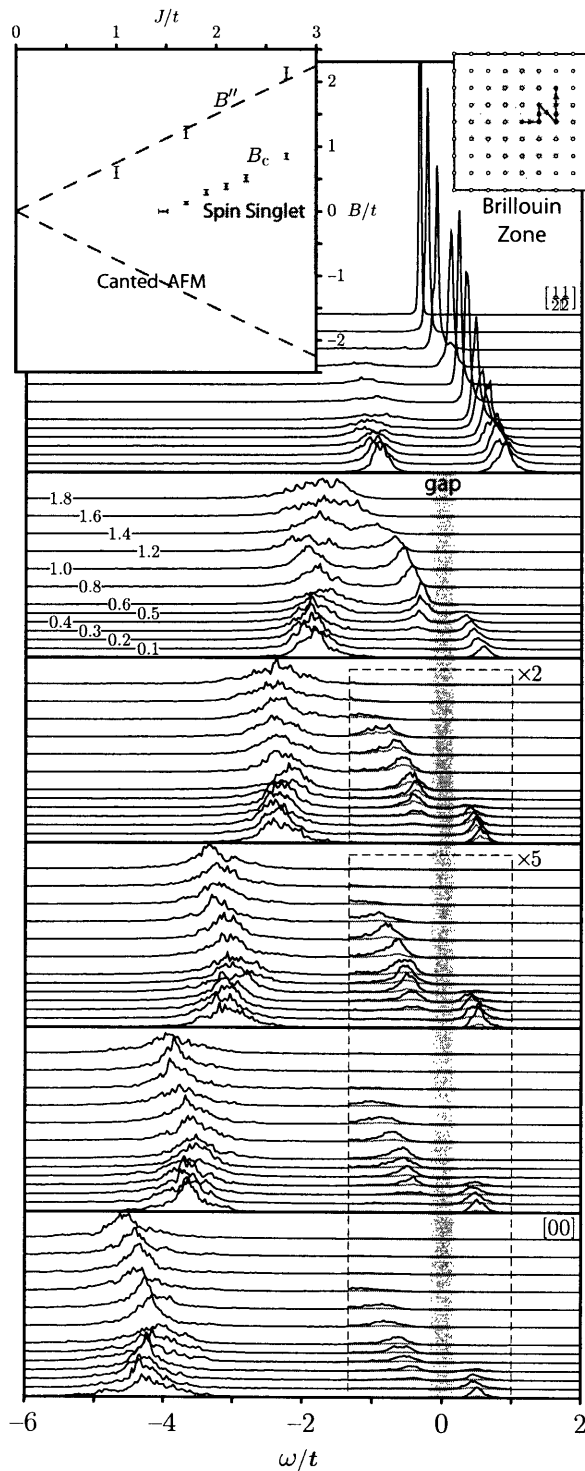


Figure 4-7:  $J/t = 1.7$ ,  $\beta t = 14$ ,  $8 \times 8$  lattice. Spectral functions  $A_{\uparrow}(\mathbf{k}, \omega)$  are plotted over a range of field values ( $0 \leq B/t \leq 1.8$  offset) for a series of wavevectors (identified in the top right inset). Smaller peaks have been scaled by the indicated magnification factor. Note that, instead of shifting smoothly through zero in a magnetic field, the spectral weight jumps across the gap, except for  $\mathbf{k}$  on the reduced zone boundary. (Top left inset) A partial phase diagram. Electron moments are directed against the field between  $B_c$  and  $B''$ .



## Chapter 5

# Constrained Quantum Monte Carlo

### 5.1 Outline

Monte Carlo techniques [26, 27] have been successfully applied to many problems in quantum magnetism and strong electronic correlations. Work in this area, however, has emphasized models such as the Heisenberg and Hubbard (and their descendants) that contain only a single kind of degree of freedom. Efficient simulation schemes have been developed for quantum spins and fermions alone, but relatively little attention has been paid to handling the two simultaneously (with several notable exceptions [28, 29, 20]). This is obviously an important issue if we want to study Kondo lattice systems, which incorporate large numbers of spins and fermions.

In developing the machinery to treat systems with mixed degrees of freedom, we want to build as much as possible on existing algorithms. To start, we must decide whether to add fermion capability to the spin algorithms or spin capability to the fermion algorithms. The latter, it turns out, is much easier to do. The stochastic series expansion [30], a powerful generalization of Handscomb's method, and the worm algorithm [31] due to Prokof'ev are the current state of the art for spin simulations. In principle, these methods could be adapted for fermions, but it would be cumbersome and very computationally expensive to keep track of all the fermion phases in spatial dimensions greater than one.

In contrast, it is relatively simple to incorporate spin degrees of freedom into the fermion simulation framework. A spin can be represented in terms of fermions using  $\hat{S} = \frac{1}{2}f^\dagger\sigma f$ , provided that we enforce  $f^\dagger f = 1$ . In other words, a Hamiltonian with spin and fermionic degrees of freedom is equivalent to a purely fermionic Hamiltonian whose Hilbert space is constrained in a particular way. Our goal in this chapter is to develop that idea into a practical simulation method.

Most of the widely-used lattice fermion algorithms fall under the loose

heading of “determinant” Monte Carlo. This is an umbrella term for algorithms that operate by stochastically sampling a system of auxiliary fields dual to the original system. The general approach is to treat the Boltzmann factor  $e^{-\beta\hat{H}}$  as a composition of infinitesimal evolution operators, each of which is subjected to a Suzuki-Trotter decomposition [32] to separate the mutually-noncommuting parts of the Hamiltonian and a Hubbard-Stratonovich transformation [33, 34] to break up the many-body terms. In this way, a Hamiltonian with two-body interaction terms is replaced by a purely one-body Hamiltonian coupled to a dynamical auxiliary field.

Since the resulting Hamiltonian is one-body in character, techniques appropriate to the noninteracting problem can be applied. For instance, it is straightforward to compute the grand-canonical trace, canonical trace, or ground state projection. Typically, the fermion degrees of freedom are eliminated by one of these methods. What remains is an effective model parameterized by the auxiliary fields.

In the Blankenbecler-Sugar-Scalapino (BSS) approach [35, 36], the grand-canonical ensemble average is computed by inserting coherent states at discrete imaginary times and then integrating out the Grassman variables. Constraints can be enforced by introducing an extra set of fields that live on the temporal links between the discrete times. Since these new fields are fully dynamical, the BSS algorithm must be modified to ensure that they are updated as well.

In what follows, we describe the modified BSS algorithm in detail. We also discuss the resolution of two other technical issues. First, the BSS requires some form of numerical stabilization in order to reach low temperatures. We present a very effective stabilization technique in which ill-conditioned matrix products are broken into smaller, well-behaved fragments. Second, we discuss how to avoid the notorious fermion sign problem. We identify a special class of Hamiltonians that are immune and show that the half-filled KLM on a square lattice belongs to this class by virtue of the model’s particle-hole symmetry and the bipartite nature of the lattice. Previous workers have not always exploited this property and have suffered from sign problems as a result [28].

## 5.2 Formulation of the Constrained Action

Consider a lattice fermion system, described by a Hamiltonian  $\hat{H}$ , whose degrees of freedom are subject to some arbitrary constraint. If the system is held in thermal equilibrium at a fixed temperature  $1/\beta > 0$ , its partition function takes the form

$$Z = \text{Tr}' e^{-\beta\hat{H}}, \quad (5.1)$$

where the prime indicates that the trace is over only those states consistent with the constraint. Now suppose that the operator  $\hat{P}$  projects states in the full Hilbert space onto the constrained subspace. The partition function can

then be expressed in terms of an *unrestricted* trace by applying  $\hat{P}$  between each imaginary time slice:

$$Z = \lim_{L \rightarrow \infty} \text{Tr} (\hat{P} e^{-\epsilon \hat{H}})^L. \quad (5.2)$$

The time step  $\epsilon = \beta/L$  becomes infinitesimal in the limit of large  $L$ .

In general, the Hamiltonian contains many-body interactions that make explicit evaluation of the trace in Eq. (5.2) impossible. These spoiler terms can often be decomposed, however, using the Hubbard-Stratonovich transformation (see Appendix A.2), which reduces two-body terms to one-body form at the price of an additional field dependence. Let  $\hat{h}(\chi)$  denote the resulting one-body Hamiltonian. The partition function now includes  $L$  integrations over the auxiliary fields:

$$Z = \lim_{L \rightarrow \infty} \int d\chi_1 \cdots d\chi_L \text{Tr} \hat{P} e^{-\epsilon \hat{h}(\chi_L)} \cdots \hat{P} e^{-\epsilon \hat{h}(\chi_1)}. \quad (5.3)$$

In terms of the fermion creation and annihilation operators  $\hat{\eta}^\dagger$  and  $\hat{\eta}$ , the Hamiltonian (after Hubbard-Stratonovich) has the bilinear form

$$\hat{h}(\chi) = \mathcal{J} |\chi|^2 + \hat{\eta}^\dagger h(\chi) \hat{\eta}. \quad (5.4)$$

In order to simplify the presentation, contracted indices (such as lattice site and spin labels) have been suppressed. In this notation,  $\hat{\eta}^\dagger$  and  $\hat{\eta}$  are, respectively, multi-component row and column vectors.  $h(\chi)$  is a rank-compatible square matrix.

In order to make the formal expression Eq. (5.3) concrete, we must select a basis for the Hilbert space. If we introduce a set of coherent states  $\{|\eta\rangle\}$ , then the operator trace  $\text{Tr} \hat{A} = \int d\bar{\eta} d\eta e^{-\bar{\eta}\eta} \langle \eta | \hat{A} | -\eta \rangle$  can be expressed as a Grassmann integral. The coherent states are eigenstates of the creation and annihilation operators, labelled by their Grassmann eigenvalues,

$$\begin{aligned} \hat{\eta} |\eta\rangle &= \eta |\eta\rangle \\ \text{and } \hat{\eta}^\dagger |\eta\rangle &= \bar{\eta} |\eta\rangle. \end{aligned} \quad (5.5)$$

Working in such a basis, we find that Eq. (5.3) is equivalent to  $Z = \lim_{L \rightarrow \infty} \int d\chi_1 \cdots d\chi_L Z_L[\chi]$ , where

$$Z_L[\chi] = \int d\bar{\eta} d\eta e^{-\bar{\eta}\eta} \langle \eta | \hat{P} e^{-\epsilon \hat{h}(\chi_1)} \cdots \hat{P} e^{-\epsilon \hat{h}(\chi_L)} | -\eta \rangle. \quad (5.6)$$

Furthermore, each single-time-step evolution operator can be expressed as a Grassman integral over coherent states:

$$e^{-\epsilon \hat{h}(\chi)} = e^{-\epsilon \mathcal{L}^0} \int d\bar{\eta} d\eta |\eta\rangle e^{-\bar{\eta} T \eta} \langle \eta|. \quad (5.7)$$

Here,  $\mathcal{L}^0 = \mathcal{J}|\chi|^2 + \text{tr } h(\chi)$  and  $T = \exp \epsilon h(\chi)$ . This identity is derived (in Appendix A.3) by inserting a coherent state representation of unity in the middle of the anti-normal-ordered operator form. Putting Eq. (5.7) into Eq. (5.6) yields

$$Z_L[\chi] = e^{-\epsilon \sum_l \mathcal{L}_l^0} \int \prod_{l=1}^L d\bar{\eta}_l d\eta_l \langle -\eta_1 | \hat{P} | \eta_L \rangle e^{-\bar{\eta}_L T_L \eta_L} \quad (5.8)$$

$$\times \langle \eta_L | \hat{P} | \eta_{L-1} \rangle e^{-\bar{\eta}_{L-1} T_{L-1} \eta_{L-1}} \dots \langle \eta_2 | \hat{P} | \eta_1 \rangle e^{-\bar{\eta}_1 T_1 \eta_1}.$$

What remains is to evaluate the matrix elements of the projection operator. For a broad class of constraints—*viz.*, those in which the disallowed states possess a particular symmetry—these matrix elements can be expressed in the integral form

$$\langle \eta | \hat{P} | \eta' \rangle = \int dz e^{\bar{\eta} U(z)^\dagger \eta'}, \quad (5.9)$$

where  $U(z)$  is a family of unitary matrices.

Accordingly,  $Z = \lim_{L \rightarrow \infty} \int (\prod_{l=1}^L d\chi_l dz_l) Z_L[\chi, z]$  requires integration over *two* sets of auxiliary fields: the interaction fields  $\chi_l$  and the constraint fields  $z_l$ . The integrand  $Z_L[\chi, z] = e^{-S[\chi, z]}$  is a function of the action

$$S = \bar{\eta}_1 U_1^\dagger \eta_L - \sum_{l=2}^L \bar{\eta}_l U_l^\dagger \eta_{l-1} + \sum_{l=1}^L (\epsilon \mathcal{L}_l^0 + \bar{\eta}_l T_l \eta_l). \quad (5.10)$$

Note that the numerical subscripts can be understood as labelling the subintervals of  $(0, \beta]$  formed by the mesh of discrete imaginary times  $\tau_l = \epsilon \cdot l$ . In Appendix A.5, we verify that this discrete action passes to the correct continuum limit.

Recall that the goal of these manipulations is to eliminate the fermion degrees of freedom and thereby derive an effective action in terms of the auxiliary fields alone. Integrating out the Grassman variables yields

$$Z_L[\chi, z] = \det M[\chi, z] e^{-S^0[\chi]}, \quad (5.11)$$

where

$$M = \begin{pmatrix} T_1 & & & & +U_1^\dagger \\ -U_2^\dagger & T_2 & & & \\ & -U_3^\dagger & T_3 & & \\ & & \ddots & \ddots & \\ & & & -U_L^\dagger & T_L \end{pmatrix} \quad (5.12)$$

and  $S^0 = \epsilon \sum_l \mathcal{L}_l^0$ .  $U_l$  and  $T_l$  are square matrices of size  $N$ , where  $N$  is the total number of fermion degrees of freedom.  $M$  is a square matrix of size  $NL$ . The resulting effective action  $S^{\text{eff}}[\chi, z] = S^0[\chi] - \text{tr} \ln M[\chi, z]$  is highly

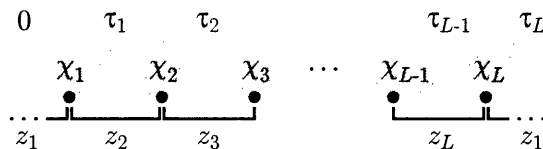


Figure 5-1: The imaginary time domain  $(0, \beta]$  is divided into  $L$  equally-spaced subintervals  $(0, \tau_1], (\tau_1, \tau_2], \dots, (\tau_{L-1}, \tau_L]$ . The interaction fields  $\chi_l$  are centred on the subintervals. The constraint fields  $z_l$  connect adjacent ones.

non-local in space and time.

Note that fermion anti-periodicity,  $\eta(0) = -\eta(\beta)$ , necessitates a sign change in the Grassman variables between  $\tau_1$  and  $\tau_L$ . This requirement, which is expressed in Eq. (5.8) by the factor  $\langle -\eta_1 | \hat{P} | \eta_L \rangle$ , is ultimately realized as a reversed sign in the top-right entry of the coefficient matrix ( $M_{1L} = +U_1^\dagger$ ).

We should emphasize that our formulation of the discrete action differs from the usual one in that Eq. (5.7) evaluates the evolution operator at *equal* times. As a consequence, the  $T_l$  blocks appear on the main diagonal of Eq. (5.12). More commonly, the evolution operator is evaluated between adjacent time slices  $\langle \eta_{l+1} | e^{-\epsilon \hat{h}} | \eta_l \rangle$ , in which case the Hamiltonian contribution is off-diagonal (see Eq. (2.70a) of Ref. [37] or Eq. (45) of Ref. [35]). Here, in other words, the interaction fields live on the time slices whereas the constraint fields live on the temporal links between them. See Fig. 5-1.

The determinant of the coefficient matrix is given by  $\det M = \det(\mathbb{1} + B_1 B_2 \cdots B_L)$ , where  $B_l = U_l T_l = U_l \exp \epsilon h(\chi_l)$  is the matrix that evolves the system from one time slice to the next. A crucial feature is that this determinant is invariant under cyclic permutation of the matrices  $B_1 \cdots B_L$ .

## 5.3 Monte Carlo Sampling

### 5.3.1 Generating the Markov Chain

All physical observables of the system are related to Eq. (5.11) by an integration over the auxiliary fields. Monte Carlo techniques can be used to approximate the intractable multi-dimensional integral by statistical sampling:

$$\langle \langle f \rangle \rangle = \frac{\int d\chi dz f[\chi, z] Z_L[\chi, z]}{\int d\chi dz Z_L[\chi, z]} \approx \frac{1}{|\mathcal{S}|} \sum_{(\chi, z) \in \mathcal{S}} f[\chi, z]. \quad (5.13)$$

Here  $\mathcal{S}$  is a finite set of independent field configurations (random variables) distributed with probability  $\mathcal{P}[\chi, z] = Z_L[\chi, z] / \int d\chi dz Z_L[\chi, z]$ .

The challenge is to construct such a set. The standard method is to start from some arbitrary initial field configuration and to build the rest of the set

sequentially as a Markov chain, with each new field configuration depending only on the one immediately preceding it.

So long as the move set  $\{(\chi, z) \rightarrow (\tilde{\chi}, \tilde{z})\}$  spans the entire configuration space and the transition probabilities  $\mathcal{W}$  are chosen to satisfy detailed balance, *viz.*,

$$\mathcal{P}[\chi, z]\mathcal{W}[(\chi, z) \rightarrow (\tilde{\chi}, \tilde{z})] = \mathcal{P}[\tilde{\chi}, \tilde{z}]\mathcal{W}[(\tilde{\chi}, \tilde{z}) \rightarrow (\chi, z)], \quad (5.14)$$

the Markov process will be ergodic and unbiased. Equation (5.14) specifies that thermodynamic equilibrium is a stationary state with respect to evolution of the fields: at equilibrium, the average number of moves  $(\chi, z) \rightarrow (\tilde{\chi}, \tilde{z})$  is the same as the average number of inverse moves  $(\tilde{\chi}, \tilde{z}) \rightarrow (\chi, z)$ . Hence, the detailed balance condition ensures that a system in equilibrium will remain in equilibrium. Moreover, one can show that a system out of equilibrium will always flow to equilibrium [38]. Given sufficient simulation time (the so-called *thermalization time* or *burn-in time*), the system is equilibrated, at which point its field configurations are suitable for sampling (*i.e.*, for inclusion in the set  $\mathcal{S}$ ). This is true irrespective of the choice of initial field configuration.

In the Monte Carlo language, an attempted application of any member of the move set is a *walk*. It consists of a trial change in the field configuration  $(\chi, z) \rightarrow (\tilde{\chi}, \tilde{z})$ , which is either accepted or rejected depending on the ratio

$$R = \frac{\mathcal{W}[(\chi, z) \rightarrow (\tilde{\chi}, \tilde{z})]}{\mathcal{W}[(\tilde{\chi}, \tilde{z}) \rightarrow (\chi, z)]} = \frac{Z_L[\tilde{\chi}, \tilde{z}]}{Z_L[\chi, z]}. \quad (5.15)$$

Written explicitly,

$$R = \frac{\det M[\tilde{\chi}, \tilde{z}]}{\det M[\chi, z]} \exp \left[ \epsilon \sum_{l=1}^L (\mathcal{L}^0[\chi_l] - \mathcal{L}^0[\tilde{\chi}_l]) \right]. \quad (5.16)$$

The simplest decision algorithm is due to Metropolis [22]. The appropriate procedure is to generate a walk, select a random number  $x \in [0, 1]$ , and accept the walk if  $x > R$ .

Clearly, the most important requirement is that  $R$  be real and positive definite, since  $\min(1, R)$  serves as the acceptance probability. This can be circumvented by accepting walks with probability  $\min(1, |R|)$  and sampling over the phase contribution of  $R$  (*i.e.*,  $\langle\langle f \rangle\rangle \rightarrow \langle\langle f e^{i\phi} \rangle\rangle / \langle\langle e^{i\phi} \rangle\rangle$ , where  $\phi = \arg R$ ), but only at the cost of exponentially slower convergence. This is the so-called *fermion sign problem*.

Here, we describe a scenario in which  $R > 0$  is guaranteed. Suppose that there is some conserved quantum number  $\alpha$  with  $2Q$  discrete values. This implies that, in the appropriate basis,  $\hat{h} = \mathcal{J}|\chi|^2 + \sum_{\alpha=1}^{2Q} \eta_{\alpha}^{\dagger} h_{\alpha} \eta_{\alpha}$  and the

matrix action  $M$  is block diagonal:

$$M = \begin{pmatrix} M_1 & & & \\ & M_2 & & \\ & & \ddots & \\ & & & M_{2Q} \end{pmatrix}. \quad (5.17)$$

If, in addition, those blocks are pairwise hermitian (*i.e.*,  $M_{\alpha+Q} = M_{\alpha}^{\dagger}$ ), then

$$\det M = \prod_{\alpha=1}^Q |\det M_{\alpha}|^2 > 0. \quad (5.18)$$

Hence  $R > 0$ , and the sign problem is avoided.

### 5.3.2 Update Scheme

In this section, we describe a generalization of the BSS update scheme [35, 36] that takes into account the presence of the constraint fields. The basic algorithm remains unchanged except that the walk attempts are now organized into  $2L$  passes (double the previous number). We apply interaction- and constraint-field walks alternately as we step sequentially through the  $L$  time slices: first we update the  $\chi_1$  fields, then the  $z_1$ , then the  $\chi_2$ , *etc.*

In order to perform the updates, we need to be able to calculate  $R$  efficiently, without having to evaluate the expensive  $NL \times NL$  matrix determinants. To start, we define the  $N \times N$  equal-time propagators

$$\mathbb{1} - g_l = (\mathbb{1} + B_{l+1} \cdots B_L B_1 \cdots B_l)^{-1}. \quad (5.19)$$

These have the property that  $\det(\mathbb{1} - g_l) = (\det M)^{-1}$  for all  $1 \leq l \leq L$ . Equation (5.19) can be inverted to recover the sequence of evolution matrices:

$$\begin{aligned} B_{l+1} \cdots B_L B_1 \cdots B_l &= (\mathbb{1} - g_l)^{-1} - \mathbb{1} \\ &= (\mathbb{1} - g_l)^{-1} g_l. \end{aligned} \quad (5.20)$$

Now suppose that interaction fields on the  $l^{\text{th}}$  time slice are modified (tentatively) so that  $T_l \rightarrow \tilde{T}_l$ . Using Eq. (5.20), we find

$$\begin{aligned} (\mathbb{1} - \tilde{g}_l)^{-1} &= \mathbb{1} + B_{l+1} \cdots B_L B_1 \cdots B_{l-1} U_l \tilde{T}_l \\ &= \mathbb{1} + (\mathbb{1} - g_l)^{-1} g_l B_l^{-1} U_l \tilde{T}_l \\ &= (\mathbb{1} - g_l)^{-1} (\mathbb{1} + g_l \Delta), \end{aligned} \quad (5.21)$$

where  $\Delta = T_l^{-1} \tilde{T}_l - \mathbb{1}$ . Accordingly,

$$\frac{\det \tilde{M}}{\det M} = \frac{\det(\mathbb{1} - g_l)}{\det(\mathbb{1} - \tilde{g}_l)} = \det(\mathbb{1} + g_l \Delta). \quad (5.22)$$

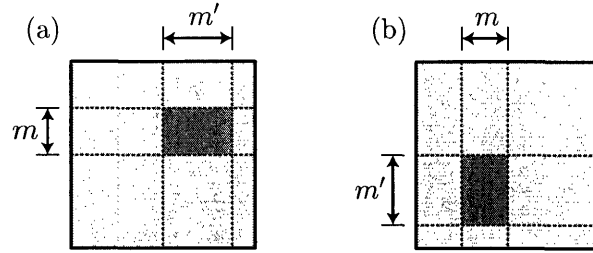


Figure 5-2: (a) Both  $\Delta$  and  $K$  are sparse  $N \times N$  matrices with zero entries everywhere except for a small  $m \times m'$  block. (b)  $g_l$ , on the other hand, is dense; nonetheless, only the transposed  $m' \times m$  block of its entries are required to compute  $R$  and  $K$ .

If only a small number of fields is modified, then  $\Delta$  has only a few nonzero entries—confined to a small  $m \times m'$  block, say. Then, Eq. (5.22) says that the ratio of two  $NL \times NL$  determinants is equal to the ratio of two  $N \times N$  determinants, which in turn is equal to a single  $m' \times m'$  determinant. This simplifies the calculation of  $R$  enormously.

If the walk is accepted,  $g_l$  must be modified to reflect the change in the field configuration. From Eq. (5.21), it follows that

$$\begin{aligned} \mathbb{1} - \tilde{g}_l &= (\mathbb{1} + g_l \Delta)^{-1} (\mathbb{1} - g_l) \\ &= \left[ \mathbb{1} + g_l \Delta (\mathbb{1} + g_l \Delta)^{-1} \right] (\mathbb{1} - g_l). \end{aligned} \quad (5.23)$$

Hence, updates to  $g_l$  can be effected iteratively using

$$\tilde{g}_l = g_l - g_l \Delta (\mathbb{1} + g_l \Delta)^{-1} (\mathbb{1} - g_l). \quad (5.24)$$

Note that Eq. (5.24) has the form  $\tilde{g}_l = g_l - g_l K (\mathbb{1} - g_l)$ , which allows for relatively fast updating since the matrix kernel  $K = \Delta (\mathbb{1} + g_l \Delta)^{-1}$ , like  $\Delta$ , has only an  $m \times m'$  block of nonzero entries.

Let  $\mathfrak{d}$  denote the block of nonzero entries of  $\Delta$  and let  $\mathfrak{g}$  represent the corresponding transposed block of entries from  $g_l$ ; see Fig. 5-2. Then, as we claimed earlier,  $R = \det(\mathbb{1} + \mathfrak{g}\mathfrak{d})$  is given by a single  $m' \times m'$  matrix determinant. Similarly, the nonzero block of  $K$  can be computed with a single  $m' \times m'$  matrix inversion,  $\mathfrak{K} = \mathfrak{d}(\mathbb{1} + \mathfrak{g}\mathfrak{d})^{-1}$ . This is an important optimization, since the simulation spends much of its time in the loop of walks and updates.

When the block width  $m'$  is very small, it is easy to solve for  $R$  and  $\mathfrak{K}$  explicitly. If  $m' = 1$ , then  $R = 1 + \mathfrak{g}\mathfrak{d}$  and  $\mathfrak{K} = \frac{1}{R}\mathfrak{d}$ . If  $m' = 2$ , then  $R = 1 + \text{tr}(\mathfrak{g}\mathfrak{d}) + \det(\mathfrak{g}\mathfrak{d})$  and  $\mathfrak{K} = \frac{1}{R}\mathfrak{d}[\mathbb{1} + \det(\mathfrak{g}\mathfrak{d})(\mathfrak{g}\mathfrak{d})^{-1}]$ . These expressions can then be implemented directly (*i.e.*, expanded out and coded component-wise), saving us the expense of computing numerically a generic matrix determinant and matrix inverse for each walk.

By this procedure, we systematically update all the interaction fields on the  $l^{\text{th}}$  time slice. To do the same for the constraint fields, we apply the transformation

$$g_{l+1/2} = T_{l+1}^{-1} g_l T_{l+1}, \quad (5.25)$$

which positions  $U_l$  at the far right of the matrix product:

$$\mathbb{1} - g_{l+1/2} = (\mathbb{1} + T_l B_{l+1} \cdots B_L B_1 \cdots B_{l-1} U_l)^{-1}. \quad (5.26)$$

We then entertain trial moves of the form  $U_l \rightarrow \tilde{U}_l$ .  $R$  and  $K$  are computed from  $g_{l+1/2}$  and  $\Delta = U_l^\dagger U_l - \mathbb{1}$ . Once all the fields on a given time slice have been updated, the entire procedure can be repeated by applying the cyclic identity  $g_{l+1} = U_{l+1}^\dagger g_{l+1/2} U_{l+1}$  to advance to the next time slice.

On a real computer with limited floating point precision, the shifting operation [Eq. (5.25)] can only be performed so many times before rounding errors become fatal.  $g_l$  must be regularly recomputed from scratch.

### 5.3.3 Accounting for Autocorrelation Effects

We have described how the update process can be made computationally efficient by restricting the attempted moves to a small number of fields on a single time slice. The trade-off is that these baby-step modifications do not substantially change the overall field configuration. Thus, configurations separated by a single walk—call them  $\chi^{(n)}$  and  $\chi^{(n+1)}$ —cannot serve as independent random variables in the Markov chain.

A more appropriate measure of progress is the *sweep*, which denotes a sequence of walks applied systematically to each field on each time slice. After one sweep, a fraction  $a$  of the fields has been updated, where  $a$  is the average acceptance ratio for the attempted moves. Many sweeps may be required to produce a new independent field configuration. This number, which we denote by  $n_1$ , is commonly called the *autocorrelation time* (in the sense of stochastic or simulation time rather than physical time).

Since the configurations will continue to have a significant overlap so long as many individual fields go un-updated, it is the case that  $n_1 \gg 1/a$ . Clearly, there is an interest in preventing  $a$  from getting too small, lest the autocorrelation time grow unmanageably long. The value of  $a$  can be increased by imposing an upper bound on the step sizes  $|\tilde{\chi} - \chi|$ ,  $|\tilde{z} - z|$  or by skewing the distribution of step sizes so that large steps are more rare. ( $a$  can be made arbitrarily close to 1 by taking the step size small enough.) At the same time, reducing the step size restricts the sampling of the configuration space, so using too small a step size may be counterproductive. These two competing effects lead to an optimal intermediate value of  $a$  at which the algorithm is maximally efficient. In practice, rather than fussing over the precise best value of  $a$ , we simply adopt the “Goldilocks rule” and aim for  $a \sim 50\%$ , either by judiciously choosing a fixed step size or by implementing an adaptive algorithm that modifies the step size on the fly.

Note that in many applications it is possible to employ finite fields that range over a discrete set of values [39]. In that case, the step size cannot be tuned arbitrarily. Thus, it may not be possible to adjust the acceptance ratio to its optimal value. For this reason, we recommend the use of continuous fields, which do not suffer from this problem.

For a data set consisting of  $\Omega$  total sweeps, the degree of overlap between configurations separated by  $n$  sweeps (with  $n \ll \Omega$ ) can be measured as follows:

$$C(n) = \frac{1}{\Omega - n} \sum_{m=1}^{\Omega-n} \text{Re} \chi^{(n+m)} \bar{\chi}^{(m)}. \quad (5.27)$$

The stochastic time scale over which these correlations decay is precisely the autocorrelation time that characterizes the update routine:  $C(n) - C(0) \sim e^{-n/n_1}$ . Thus, measurements of Eq. (5.27) can be used to compute the value of  $n_1$ .

Since  $n_1$  represents the basic time scale for meaningful changes in the fields, we can take the thermalization time to be some large number of autocorrelation times; *e.g.*,  $n_0 = 1000n_1$ . Thus, the appropriate choice of sample set for use in Eq. (5.13) is

$$\mathcal{S} = \{(\chi^{(n)}, z^{(n)}) : n = n_0, n_0 + n_1, n_0 + 2n_1, \dots\}. \quad (5.28)$$

## 5.4 Computing Physical Observables

Every measurable property of the system can be expressed as an ensemble average of a physical operator acting in the Hilbert space of the original Hamiltonian (using either  $\langle \hat{A} \rangle = Z^{-1} \text{Tr}' e^{-\beta \hat{H}} \hat{A}$  or its time-ordered generalization). In the determinant Monte Carlo scheme, however, the descriptive framework is no longer the system of fermions but instead the dual system of interacting fields. The Grassman degrees of freedom have been purged, and the detailed evolution of the fermion states is no longer directly accessible.

Nonetheless, that information is not lost; rather, it is encoded, albeit indirectly (*i.e.*, highly non-locally), in the configuration of the auxiliary fields. As we shall show, every operator has an auxiliary-field-dependent counterpart (operator  $\hat{A} \leftrightarrow$  function  $A[\chi, z]$ ) that, when field averaged via Eq. (5.13), is equal to  $\langle \hat{A} \rangle$ . This section is devoted to clarifying that correspondence.

Let us consider the most general measurement that can be made using the determinant quantum Monte Carlo scheme. It is possible to compute the ensemble average of any time-ordered operator sequence

$$\langle \hat{A}(\tau') \hat{B}(\tau'') \hat{C}(\tau''') \dots \rangle = \frac{1}{Z} \text{Tr}' \text{T} \left[ e^{-\int_0^\beta d\tau \hat{H}(\tau)} \hat{A}(\tau') \hat{B}(\tau'') \hat{C}(\tau''') \dots \right]. \quad (5.29)$$

As it turns out, we can treat this in much the same way we did the partition function. Repeating the manipulations that took us from Eq. (5.1) to Eq. (5.10), and letting the time ordering control the placement of the



Green's function is given by

$$\langle \hat{\eta}_{i\alpha}(\tau_k) \hat{\eta}_{j\beta}^\dagger(\tau_l) \rangle = \langle \langle G_{kl}; ij; \alpha\beta \rangle \rangle, \quad (5.35)$$

where  $G_{kl}$  is the matrix block formed by the  $\tau_k, \tau_l$  components of  $\mathcal{M}^{-1}$ . Explicitly, these are

$$G_{kl} = \begin{cases} (\mathbb{1} + B_{l+1} \cdots B_L B_1 \cdots B_l)^{-1} B_{l+1} \cdots B_k & k > l \\ \mathbb{1} - (\mathbb{1} + B_{l+1} \cdots B_L B_1 \cdots B_l)^{-1} & k = l \\ -B_{l+1} \cdots B_L B_1 \cdots B_k (\mathbb{1} + B_{l+1} \cdots B_L B_1 \cdots B_l)^{-1} & k < l. \end{cases} \quad (5.36)$$

More generally, the  $n$ -point function is constructed from linear combinations of the  $G$  matrices:

$$\begin{aligned} & \langle \hat{\eta}_{i_1 \alpha_1}(\tau_{k_1}) \hat{\eta}_{i_2 \alpha_2}(\tau_{k_2}) \cdots \hat{\eta}_{i_n \alpha_n}(\tau_{k_n}) \hat{\eta}_{j_n \beta_n}^\dagger(\tau_{l_n}) \cdots \hat{\eta}_{j_2 \beta_2}^\dagger(\tau_{l_2}) \hat{\eta}_{j_1 \beta_1}^\dagger(\tau_{l_1}) \rangle \\ &= \sum_{\zeta} (-1)^\zeta \langle \langle G_{k_{\zeta_1} l_1; i_{\zeta_1} j_1; \alpha_{\zeta_1} \beta_1} \cdots G_{k_{\zeta_n} l_n; i_{\zeta_n} j_n; \alpha_{\zeta_n} \beta_n} \rangle \rangle. \end{aligned} \quad (5.37)$$

The summation is over all permutations of degree  $n$ . Even and odd permutations contribute a factor  $(-1)^\zeta = 1$  and  $-1$ , respectively.

Recall that, by assumption, the model exhibits a conserved quantum number with even symmetry. The  $G$  matrices have no off-diagonal components in this quantum number, and the diagonal components are pairwise conjugate:

$$G_{kl; ij; \alpha\beta} = \delta_{\alpha\beta} \begin{cases} G_{kl; ij; \alpha\alpha} & \text{if } 1 \leq \alpha \leq Q \\ G_{kl; ij; \alpha-Q, \alpha-Q}^* & \text{if } Q < \alpha \leq 2Q. \end{cases} \quad (5.38)$$

Since only half the components are independent, we need only keep track of the  $1 \leq \alpha \leq Q$  components.  $B_l$  and  $G_{kl}$  can be stored as  $(N/2) \times (N/2)$  matrices, which reduces the computer memory requirements by a factor of four.

A further simplification follows from the imaginary-time translational invariance of the model. It is not necessary to compute all of the  $L^2$  components of  $G_{kl}$ . Rather, it suffices to construct the following  $3L - 2$  quantities:

$$\begin{aligned} \mathcal{G}_l^{(>)} &= G_{L-l, L} = (\mathbb{1} + B_1 \cdots B_L)^{-1} B_1 \cdots B_{L-l} \\ \mathcal{G}_l^{(=)} &= G_{l, l} = \mathbb{1} - (\mathbb{1} + B_{l+1} \cdots B_L B_1 \cdots B_l)^{-1} \\ \mathcal{G}_l^{(<)} &= G_{L, L-l} = -B_{L-l} \cdots B_L (\mathbb{1} + B_1 \cdots B_L)^{-1} \end{aligned} \quad (5.39)$$

for  $0 < l < L$ , and

$$\mathcal{G}_0^{(>)} = \mathcal{G}_0^{(=)} = \mathcal{G}_0^{(<)} = G_{LL}. \quad (5.40)$$

Here, we have introduced the superscript notation  $(>)$ ,  $(=)$ , and  $(<)$  to label the positive-, equal-, and negative-time propagators. We have already

encountered the equal-time version [see Eq. (5.19)], which we previously denoted  $g_l$ .

In terms of these time-translation-invariant propagators, the common two- and four-point functions are given by

$$\langle \hat{\eta}(\tau_k) \hat{\eta}^\dagger(\tau_l) \rangle = \begin{cases} \langle \langle \mathcal{G}_{k-l}^{(>)} \rangle \rangle & \text{if } k \geq l \\ \langle \langle \mathcal{G}_{l-k}^{(<)} \rangle \rangle & \text{if } k < l \end{cases} \quad (5.41)$$

and

$$\langle \hat{\eta}(\tau_k) \hat{\eta}(\tau_l) \hat{\eta}^\dagger(\tau_l) \hat{\eta}^\dagger(\tau_k) \rangle = \langle \langle \mathcal{G}_{|k-l|}^{(=)} \mathcal{G}_0^{(=)} \rangle \rangle - \langle \langle \mathcal{G}_{|k-l|}^{(>)} \mathcal{G}_{|k-l|}^{(<)} \rangle \rangle. \quad (5.42)$$

In Eqs. (5.41) and (5.42), we have suppressed all site and spin labels.

## 5.5 Numerical Stabilization

One serious drawback of the BSS algorithm is that its floating point precision requirements increase without bound as the simulation temperature goes to zero. On a typical 32-bit machine, the lowest accessible temperature is  $\beta \sim 4W$ , where  $W$  is the width of the energy spectrum of  $\hat{H}$ . This is a serious impediment because it is precisely the low-temperature properties of the system that are typically of interest.

In the first instance, the culprit is the the half-time-step shifting operation, Eq. (5.25), which is used to advance from the current time slice to the next temporal link. It introduces serious rounding errors each time it is applied. Up to a point, this difficulty can be circumvented by occasionally recomputing  $g_l$  directly from Eq. (5.19). As the temperature is lowered, however, the number of shifts that can be safely performed decreases, and  $g_l$  must be recomputed more and more often. At some sufficiently low temperature, the allowed number of shifts drops to zero, and  $g_l$  must be recomputed for each time slice.

The more fundamental limitation is that, at lower temperatures still, it becomes impossible even to recompute  $g_l$  using standard numerical techniques (*e.g.*, Gaussian elimination). The product of the evolution matrices  $B_1 \cdots B_L \sim \prod_{l=1}^L U_l e^{\epsilon h(x_l)}$  has eigenvalues both exponentially large and exponentially small in  $\beta W$ . It is effectively ill-conditioned on a finite precision computer: *i.e.*,  $\text{cond}(B_1 \cdots B_L) \sim e^{\beta W} > F_\infty$ , where  $F_\infty$  is the machine infinity. And its largest eigenvalues swamp the unit contribution whenever we attempted to compute the propagator  $(\mathbf{1} + B_1 \cdots B_L)^{-1}$ .

The essence of the problem is that the BSS algorithm trades off numerical stability for speed. There exists a more straightforward update scheme [29], one that does not suffer from stability problems, but it involves keeping track of the coefficient matrix  $M$  in its entirety and naively computing its complete  $NL \times NL$  inverse after each time step. This method is grossly inefficient. Its computational requirements scale as  $\text{CPU} \sim N^3 L^3$ , making

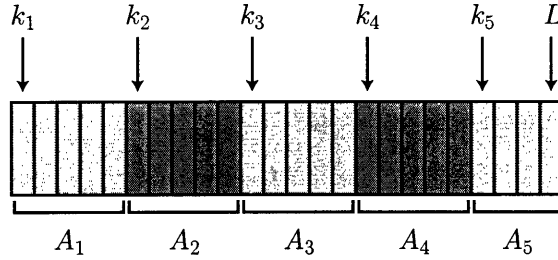


Figure 5-3:  $L = 24$  time slices are partitioned into bundles of at most  $L_0 = 5$ . The starting position of each bundle is given by  $k_1 = 1$ ,  $k_2 = 6$ ,  $k_3 = 11$ ,  $k_4 = 16$ , and  $k_5 = 20$ .

it intractable for large numbers of time slices. The advantage of the BSS algorithm is that its working matrices are only  $N \times N$  in size,  $L$  in number. Hence,  $\text{CPU} \sim N^3 L$ .

Hirsch attempted to interpolate between these two schemes [40] by collapsing the time slices into  $P = L/L_0$  groups of  $L_0$ . Here, the same set of  $NP \times NP$  matrix manipulations are repeated  $L_0$  times, which means that  $\text{CPU} \sim (NP)^3 L_0 = N^3 LP^2$ . The troublesome BSS matrix is replaced by a larger, better-conditioned one. The trade-off is that the execution time increases by a factor of  $P^2$ . This method has been used with some success [41, 42, 43, 44].

A more sophisticated approach due to White, Scalapino, and Sugar [45] uses Gram-Schmidt orthogonalization to decompose the evolution matrices into independent modes covering the full range of energy scales. They are expressed as the product of well-conditioned dense matrices and diagonal matrices holding the terms that vary widely in magnitude. The computation is organized to keep the large and small eigenvalues separated from one another. The rounding error introduced at each matrix operation is thus minimized.

It is possible to achieve the same effect without resorting to complicated matrix factorization. We make use of the fact that shorter strings of evolution matrices have a correspondingly smaller numerical range. If the time slices are collected into bundles of size  $L_0$ , then  $\text{cond}(B_1 \cdots B_{L_0}) \sim e^{\beta W/P}$  where the number of bundles is  $P = \text{ceil}(L/L_0)$ . It is possible to choose the bundle size small enough (small  $L_0$ , large  $P$ ) so that  $e^{\beta W/P} < F_\infty$ . Using these bundles, we compute small propagator fragments that can later be assembled using special matrix composition operations [46]:

$$\begin{aligned} x \odot y &\equiv y(\mathbb{1} - x - y + 2xy)^{-1} x \\ x \otimes y &\equiv y(\mathbb{1} - x - y + 2xy)^{-1} (\mathbb{1} - x). \end{aligned} \quad (5.43)$$

Any subset of the time slices  $k_1 (= 1) < k_2 < \cdots < k_P < L$  naturally partitions the time slices into bundles  $[k_1, k_2 - 1], [k_2, k_3 - 1], \dots, [k_P, L]$ . For

our purposes, it is convenient to choose  $k_p = 1 + (p - 1)L_0$ , as depicted in Fig. 5-3. The corresponding propagator fragments are

$$A_p = \begin{cases} (\mathbb{1} + B_{k_p} B_{k_p+1} \cdots B_{k_{p+1}-1})^{-1} & \text{if } 1 \leq p < P \\ (\mathbb{1} + B_{k_P} B_{k_P+1} \cdots B_L)^{-1} & \text{if } p = P. \end{cases} \quad (5.44)$$

Each of these can be safely computed so long as the numerical range  $e^{\beta W/P} \sim e^{\epsilon L_0 W}$  is small enough. (There is no lower bound to the temperatures that are accessible by this method since  $\epsilon L_0 \sim L_0/L$  can be made arbitrarily small by a combination of increasing the total number of time slices and decreasing the time-slice bundle size.)

The  $A_p$  matrices are numerically stable building blocks. We string them together using the composition operations defined in Eq. (5.43) in order to construct the full propagators. These operations are associative and satisfy  $(\mathbb{1} + a)^{-1} \odot (\mathbb{1} + b)^{-1} = (\mathbb{1} + ab)^{-1}$  and  $(\mathbb{1} + a)^{-1} \otimes (\mathbb{1} + b)^{-1} = (a^{-1} + b)^{-1}$ .

The equal-time propagator, evaluated at one of the special times  $k_p$ , is given by

$$\begin{aligned} \mathcal{G}_{k_p}^{(=)} &= \mathbb{1} - (\mathbb{1} + B_{k_p+1} \cdots B_L B_1 \cdots B_{k_p})^{-1} \\ &= \mathbb{1} - A_{p+1} \odot \cdots \odot A_P \odot A_1 \odot \cdots \odot A_p. \end{aligned} \quad (5.45)$$

The remaining intermediate values ( $k_p < l < k_{p+1}$ ) can be filled in using

$$\mathcal{G}_l^{(=)} = B_{k_p-1}^{-1} \cdots B_l^{-1} \mathcal{G}_{k_p}^{(=)} B_l \cdots B_{k_p-1}. \quad (5.46)$$

To compute the positive- and negative-time propagators, it is helpful to express them in the form

$$\begin{aligned} \mathcal{G}_{L-l}^{(>)} &= (B_l^{-1} \cdots B_1^{-1} + B_{l+1} \cdots B_L)^{-1} \\ \mathcal{G}_{L-l}^{(<)} &= -(B_L^{-1} \cdots B_{l+1}^{-1} + B_1 \cdots B_l)^{-1}, \end{aligned} \quad (5.47)$$

rather than as shown in Eq. (5.39). It follows that

$$\begin{aligned} \mathcal{G}_{L-k_p}^{(>)} &= (B_l^{-1} \cdots B_1^{-1} + B_{k_p+1} \cdots B_L)^{-1} \\ &= (A_1 \odot \cdots \odot A_p) \otimes (A_{p+1} \odot \cdots \odot A_P) \\ \mathcal{G}_{L-k_p}^{(<)} &= -(B_L^{-1} \cdots B_{k_p+1}^{-1} + B_1 \cdots B_l)^{-1} \\ &= -(A_{p+1} \odot \cdots \odot A_P) \otimes (A_1 \odot \cdots \odot A_p). \end{aligned} \quad (5.48)$$

The remaining values can be computed using

$$\begin{aligned} \mathcal{G}_{L-l}^{(>)} &= \mathcal{G}_{L-k_p}^{(>)} B_{k_p+1} \cdots B_l \\ \mathcal{G}_{L-l}^{(<)} &= B_l \cdots B_{k_p+1} \mathcal{G}_{L-k_p+1}^{(<)}. \end{aligned} \quad (5.49)$$

## 5.6 Kondo Lattice Model

In this chapter, we have described a method for simulating lattice fermions that live in a constrained Hilbert space. The method is applicable to any system whose Hamiltonian is pairwise conjugate in some conserved quantum number and whose constraint can be represented by an integral in the form of Eq. (5.9). We now specialize to the KLM, our model of interest, and show that it meets these criteria.

The KLM Hamiltonian is given by

$$\hat{H} = -t \sum_{\langle ij \rangle} (c_i^\dagger c_j + c_j^\dagger c_i) + J \sum_i \frac{1}{2} c_i^\dagger \boldsymbol{\sigma} c_i \cdot \hat{\mathbf{S}}_i - B \sum_i (\frac{1}{2} c_i^\dagger \sigma^3 c_i + \hat{\mathbf{S}}_i). \quad (5.50)$$

Its spins can be represented by  $\hat{\mathbf{S}} = \frac{1}{2} f^\dagger \boldsymbol{\sigma} f$ , provided that we restrict  $f^\dagger f = 1$ . This is in keeping with our strategy of reducing the system to purely fermionic variables subject to constraints. In this representation, the exchange interaction looks like

$$\begin{aligned} c^\dagger \boldsymbol{\sigma} c \cdot f^\dagger \boldsymbol{\sigma} f &= \sum_{s,s'} [2c_s^\dagger c_{s'} f_{s'}^\dagger f_s - c_s^\dagger c_s f_{s'}^\dagger f_{s'}] \\ &= \sum_{s,s'} [2c_s^\dagger c_{s'} f_{s'}^\dagger f_s - (c_s^\dagger c_s + f_s^\dagger f_s)] + 1. \end{aligned} \quad (5.51)$$

Up to a constant, this is equal to the anticommutator  $\{\hat{O}, \hat{O}^\dagger\}$  of the hybridization operator  $\hat{O} = f^\dagger c$ . It is straightforward to show that

$$\begin{aligned} \hat{O}^\dagger \hat{O} &= \sum_s c_s^\dagger c_s - \sum_{s,s'} c_s^\dagger c_{s'} f_{s'}^\dagger f_s \\ \hat{O} \hat{O}^\dagger &= \sum_s f_s^\dagger f_s - \sum_{s,s'} c_s^\dagger c_{s'} f_{s'}^\dagger f_s. \end{aligned} \quad (5.52)$$

Comparing these results with Eq. (5.51), we see that

$$\hat{O}^\dagger \hat{O} + \hat{O} \hat{O}^\dagger = 1 - 2c^\dagger \boldsymbol{\sigma} c \cdot \hat{\mathbf{S}}. \quad (5.53)$$

We now change to a new fermion basis in which the symmetry of the Hamiltonian is explicit. (An important requirement for what follows is that the lattice be bipartite.) Consider the mapping

$$\begin{pmatrix} c_{i\uparrow} \\ c_{i\downarrow} \\ f_{i\uparrow} \\ f_{i\downarrow} \end{pmatrix} \longrightarrow \begin{pmatrix} \eta_{i1} \\ (-1)^i \eta_{i2}^\dagger \\ \xi_{i1} \\ (-1)^{i+1} \xi_{i2}^\dagger \end{pmatrix}, \quad (5.54)$$

which consists of a particle-hole transformation in the down spin channel, a  $\pi/2$  rotation of the conduction electrons in the A sublattice, and a  $\pi/2$

rotation of the local spins in the B sublattice. The hopping term in the Hamiltonian is invariant under this mapping: the nearest neighbour sites  $i$  and  $j$  are in different sublattices and thus  $c_i^\dagger c_j = \eta_i^\dagger \eta_j + \eta_j^\dagger \eta_i$ . In the Zeeman term, however, the local magnetization is transformed into a density operator:  $c_i^\dagger \sigma^3 c_i = \eta_i^\dagger \eta_i - 1$ .  $B/2$  now plays the role of a chemical potential. The resulting Hamiltonian is

$$\begin{aligned} \hat{H} = & -t \sum_{\langle ij \rangle} (\eta_i^\dagger \eta_j + \eta_j^\dagger \eta_i) - \frac{J}{4} \sum_i (\hat{O}_i^\dagger \hat{O}_i + \hat{O}_i \hat{O}_i^\dagger) \\ & - \frac{B}{2} \sum_i (\eta_i^\dagger \eta_i + \xi_i^\dagger \xi_i) + (J/4 + B)N. \end{aligned} \quad (5.55)$$

Following Eq. (5.53), we have expressed the exchange interaction in terms of the hybridization operator  $\hat{O} = \xi_1^\dagger \eta_1 + \eta_2^\dagger \xi_2$ .

Decomposing the interaction in the hybridization channel yields

$$e^{\frac{\epsilon J}{4}(\hat{O}^\dagger \hat{O} + \hat{O} \hat{O}^\dagger)} \sim \int d\chi \exp \left[ -\frac{\epsilon J}{2} (|\chi|^2 + (\chi \hat{O}^\dagger + \bar{\chi} \hat{O})) \right], \quad (5.56)$$

where  $\chi$  is a complex field. Making the identification  $e^{-\epsilon \hat{H}} \sim \int d\chi e^{-\epsilon \hat{h}[\chi]}$ , Eq. (5.55) is replaced with the bilinear (field-dependent) Hamiltonian

$$\begin{aligned} \hat{h}[\chi] = & -t \sum_{\langle ij \rangle} (\eta_i^\dagger \eta_j + \text{h.c.}) + \frac{J}{2} \sum_i \left[ \eta_i^\dagger \begin{pmatrix} \chi_i & 0 \\ 0 & \bar{\chi}_i \end{pmatrix} \xi_i + \text{h.c.} \right] \\ & - \frac{B}{2} \sum_i (\eta_i^\dagger \eta_i + \xi_i^\dagger \xi_i) + \frac{J}{2} \sum_i |\chi_i|^2 + (J/4 + B)N. \end{aligned} \quad (5.57)$$

Up to a constant, Eq. (5.57) is equal to

$$\frac{J}{2} \sum_i |\chi_i|^2 + \sum_{ij} \left[ \begin{pmatrix} \eta_{i1}^\dagger & \xi_{i1}^\dagger \end{pmatrix} h_{ij} \begin{pmatrix} \eta_{j1} \\ \xi_{j1} \end{pmatrix} + \begin{pmatrix} \eta_{i2}^\dagger & \xi_{i2}^\dagger \end{pmatrix} h_{ij} \begin{pmatrix} \eta_{j2} \\ \xi_{j2} \end{pmatrix} \right], \quad (5.58)$$

where  $h_{ij}$  has nonzero entries only between nearest neighbours and onsite:

$$h_{ij} = \begin{pmatrix} -t & 0 \\ 0 & 0 \end{pmatrix} \quad \text{and} \quad h_{ii} = \frac{1}{2} \begin{pmatrix} -B & J\chi \\ J\bar{\chi} & -B \end{pmatrix}. \quad (5.59)$$

We conclude that the model has no sign problem. According to Eq. (5.58), the Hamiltonian divides into two hermitian-conjugate blocks, associated with the pseudo-spin values  $\alpha = 1$  and  $\alpha = 2$ . This corresponds to the  $Q = 1$  case of Eq. (5.17). In the original basis, this symmetry was not apparent.

Another consequence of working in the  $\eta$  and  $\xi$  basis is that the occupation constraint is transformed into the requirement that the number of  $\xi$

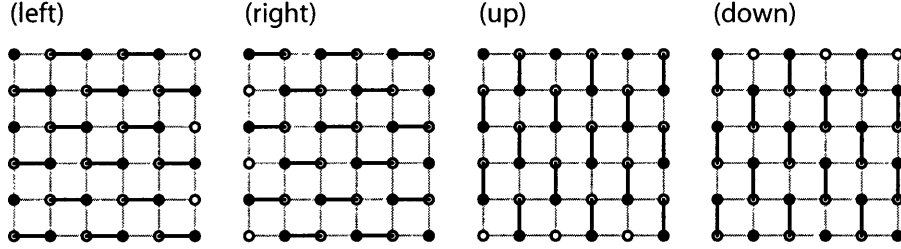


Figure 5-4: The bipartite lattice consists of interpenetrating A (solid dots) and B (open dots) sublattices. The checkerboard decomposition partitions the bonds into those that emerge right, left, up, and down from sites on the A sublattice.

fermions be even:

$$f^\dagger f = 1 \iff \xi_1^\dagger \xi_1 = \xi_2^\dagger \xi_2 \iff \xi^\dagger \xi = 0, 2 \quad (5.60)$$

As we show in Appendix A.4, the operator  $\hat{P}$  that projects onto the even-occupancy states has the integral form

$$\langle \xi | \hat{P} | \xi' \rangle = \int_{z \in U(1)} dz \exp \left[ \bar{\xi} \begin{pmatrix} z & 0 \\ 0 & \bar{z} \end{pmatrix} \xi' \right]. \quad (5.61)$$

At this point, the formal correspondence with our earlier notation is complete. The Lagrangian offset  $\mathcal{L}^0 = \frac{J}{2} \sum_i |\chi_i|^2 + \text{const}$  can be read off from Eq. (5.58). Exponentiating Eq. (5.59) gives  $T = e^{\epsilon h}$ . From Eq. (5.61), we identify the constraint matrix

$$U_{ii} = \begin{pmatrix} 1 & 0 \\ 0 & z_i \end{pmatrix}. \quad (5.62)$$

The constraint field updates are carried out as exactly as described in Sect. 5.3.2. For example, if one constraint field at site  $i_0$  is modified then  $U \rightarrow \tilde{U}$  implies that  $\Delta = U^{-1} \tilde{U} - \mathbf{1}$  has the form

$$\Delta_{i_0 i_0} = \begin{pmatrix} 0 & 0 \\ 0 & z_{i_0} \bar{z}_{i_0}^* - 1 \end{pmatrix}. \quad (5.63)$$

The acceptance ratio is  $R = 1 + (z_{i_0} \bar{z}_{i_0}^* - 1) g_{i_0 i_0; \xi \xi}$ , and the equal-time propagator is updated with  $\tilde{g} = g - gK(\mathbf{1} - g)$ . The update kernel is

$$K_{ij} = \delta_{i, i_0} \delta_{j, i_0} \begin{pmatrix} 0 & 0 \\ 0 & \frac{z_{i_0} \bar{z}_{i_0}^* - 1}{1 + (z_{i_0} \bar{z}_{i_0}^* - 1) g_{i_0 i_0; \xi \xi}} \end{pmatrix}. \quad (5.64)$$

Updates for the interaction fields, however, are not so straightforward. A

difficulty we have not yet discussed is that each entry  $T_{ij}$  depends nonlinearly on every field value  $\chi_i$ . The exponentiation  $T = e^{\epsilon h}$  involves an infinite series of matrix products

$$(e^{\epsilon h})_{ij} = \delta_{ij} + \epsilon h_{ij} + \frac{1}{2}\epsilon^2 \sum_{j'} h_{ij'} h_{j'j} + \frac{1}{6}\epsilon^3 \sum_{j'j''} h_{ij'} h_{j'j''} h_{j''j} + \dots \quad (5.65)$$

so that every site is connected to every other by a chain of operators. The update scheme, however, depends on our being able to limit changes in  $T$  to a small block of entries.

We can accomplish this, at least approximately, by partitioning the Hamiltonian into mutually isolated pieces whose bond operators share no sites in common. We first separate the off-diagonal and diagonal components,  $h(\chi) = h^{(t)} + h^{(JB)}(\chi)$ . We further break up the hopping term by bond direction: using the checkerboard decomposition shown in Fig. 5-4, we write  $h^{(t)} = \sum_{\delta} h^{(t,\delta)}$  where  $\delta = \text{left, right, up, down}$ .

This allows us to write  $T$  as a product

$$T = e^{\epsilon h} = \left( \prod_{\delta} T^{(t,\delta)} \right) T^{(JB)} + O(\epsilon^2) \quad (5.66)$$

with terms that are trivially exponentiated and local in  $\chi_i$ . The nonzero entries of  $T^{(t,\delta)}$  are given by

$$T_{ii}^{(t,\delta)} = [e^{\epsilon h^{(t,\delta)}}]_{ii} = \begin{pmatrix} \cosh \epsilon t & 0 \\ 0 & 1 \end{pmatrix} \quad (5.67)$$

and

$$T_{ij}^{(t,\delta)} = [e^{\epsilon h^{(t,\delta)}}]_{ij} = \begin{pmatrix} -\sinh \epsilon t & 0 \\ 0 & 0 \end{pmatrix}, \quad (5.68)$$

where  $i$  labels a site in the A sublattice and  $j = i + \delta$  a site in the B sublattice.  $T^{(JB)}$  is diagonal in the site indices:

$$T_{ii}^{(JB)} = [e^{\epsilon h^{(JB)}}]_{ii} = e^{-\epsilon B/2} \begin{pmatrix} \cosh |\epsilon J \chi_i/2| & \frac{\chi_i}{|\chi_i|} \sinh |\epsilon J \chi_i/2| \\ \frac{\bar{\chi}_i}{|\chi_i|} \sinh |\epsilon J \chi_i/2| & \cosh |\epsilon J \chi_i/2| \end{pmatrix}. \quad (5.69)$$



## Chapter 6

# Stochastic Analytic Continuation

### 6.1 Outline

Wick rotation transforms imaginary time correlation functions into real, measurable response functions. Analytical results, or numerical results fit to a known functional form, allow for a simple substitution of variables: *e.g.*,  $-i\tau \mapsto t(1 + i0^+)$ . In general, however, this is not possible. To interpret the results of computer simulations such as quantum Monte Carlo and to make comparisons with experiment, we require a technique that reliably extracts spectral information from imaginary time data. At issue is how best to do this given that the input data is intrinsically noisy and incomplete.

The most widely used technique is the venerable maximum entropy method (MEM) [47, 48, 49], which selects the best candidate solution that is consistent with the data. Here, “best” means most likely in the Bayesian sense. There are several variations on the algorithm, but in general it plays out as a competition between the goodness-of-fit measure  $\chi^2$  and the entropic prior  $\mathcal{S}$ . In practice, one minimizes the functional  $\chi^2 - \alpha^{-1}\mathcal{S}$  (for some  $\alpha^{-1} \neq 0$ ). The presence of the entropic prior introduces a non-linearity that pulls the minimum away from the least squares solution. One of the key advantages to the method is that it is rigorously derived from statistical considerations and guarantees a unique solution (for each  $\alpha$ ).

Another strategy is to generate a sequence of possible solutions and then take their mean, with the hope that spurious features will be averaged out and legitimate features reinforced (as, *e.g.*, in Ref. [50]). Such methods, however, tend to be *ad hoc* and are not rigorously justified. There are no criteria for selecting which solutions to include or for assigning their relative weights in the sum. Moreover, how these schemes are related to the MEM solution is unclear. There is no reason *a priori* to believe that an average over several possible spectra will be closer to the true spectrum than the single most probable one.

Nonetheless, there is compelling evidence that averaging methods can produce better spectra than the MEM. In particular, Sandvik [25] has shown that an unbiased thermal average of all possible spectra, Boltzmann weighted according to  $\chi^2$ , produces (in several test cases) an average spectrum that is in better agreement with the true spectrum (found via exact diagonalization) than is the MEM result. Indeed, our own experience suggests that the MEM is unduly biased toward smooth solutions: sharp spectral features tend to be washed out or obliterated.

In this chapter, we show how the averaging approach can be made systematic. We relate the analytic continuation problem to a system of interacting classical fields living on the unit interval and prove that the MEM solution is realized as its mean field configuration. From that point of view, Sandvik's method amounts to allowing thermal fluctuations about this mean field configuration. It is, in some sense, the most natural dynamical generalization of the MEM. Finally, we sketch out an improved algorithm for performing the stochastic sampling and provide test results for the two methods applied to the spectrum of a simple BCS superconductor.

## 6.2 Analytic Continuation

A dynamical correlation function of imaginary time,  $G(\tau) = \langle T[\hat{O}(\tau)\hat{O}^\dagger(0)] \rangle$ , satisfies the (anti-)periodicity relation  $G(\tau + \beta) = \mp G(\tau)$ , where the upper sign holds for fermionic operators and the lower sign for bosonic ones. Since it is uniquely determined by its values in the region  $\tau \in [0, \beta)$ , the function admits a discrete Fourier transform

$$G(\tau) = \frac{1}{\beta} \sum_{\omega_n} e^{-i\omega_n\tau} G(\omega_n) \quad (6.1a)$$

$$G(\omega_n) = \int_0^\beta d\tau e^{i\omega_n\tau} G(\tau), \quad (6.1b)$$

where the sum is over the Matsubara frequencies  $\omega_n = (2n + 1)\pi/\beta$  for fermions and  $\omega_n = 2n\pi/\beta$  for bosons, with  $n \in \mathbb{Z}$ .

Provided that  $|G(\omega_n)|$  falls off at least as fast as  $1/|\omega_n|$  when  $n \rightarrow \infty$  (which is guaranteed so long as the operator (anti-)commutator satisfies  $\langle \hat{O}\hat{O}^\dagger \pm \hat{O}^\dagger\hat{O} \rangle < \infty$ ), the Fourier components are representable in terms of a function of the form

$$\mathcal{G}(z) = \mp \int_{-\infty}^{\infty} \frac{d\omega}{2\pi} \frac{\rho(\omega)}{z - \omega} \quad (6.2)$$

with the identification  $G(\omega_n) = \mathcal{G}(i\omega_n)$ . The function  $\rho(\omega)$  is real-valued and satisfies  $\rho(\omega) \geq 0$  for fermions and  $\text{sgn}(\omega)\rho(\omega) \geq 0$  for bosons. Note that  $\mathcal{G}(z)$  is analytic everywhere in the complex plane, with the possible exception of the real line. Wherever  $\rho(\omega)$  is nonzero, there will be a corresponding jump in  $\mathcal{G}(z)$ :

$$\mathcal{G}(\omega + i0^+) - \mathcal{G}(\omega - i0^+) = \pm\rho(\omega). \quad (6.3)$$

The principle of analytic continuation states that given the value of  $\mathcal{G}(z)$  at a countably infinite number of points along the imaginary axis—by which we mean that  $G(\omega_n)$  or, equivalently,  $G(\tau)$  is known—we can *uniquely* extend  $\mathcal{G}(z)$  from those points to the full complex plane. In particular, we can find its values just above and just below the real axis and hence, via Eq. (6.3), extract  $\rho(\omega)$ .

According to Eq. (6.2), we can write

$$G(\omega_n) = \mp \int \frac{d\omega}{2\pi} \frac{\rho(\omega)}{i\omega_n - \omega}. \quad (6.4)$$

Transforming back to imaginary time, via Eq. (6.1a), and performing the Matsubara frequency sum yields

$$\begin{aligned} G(\tau) &= \mp \int \frac{d\omega}{2\pi} \frac{1}{\beta} \sum_{\omega_n} \frac{e^{-i\omega_n\tau}}{i\omega_n - \omega} \rho(\omega) \\ &= \int \frac{d\omega}{2\pi} \frac{e^{-\omega\tau} \rho(\omega)}{e^{-\beta\omega} \pm 1} \\ &= \int d\omega K(\tau, \omega) A(\omega). \end{aligned} \quad (6.5)$$

In the last line, we have defined

$$K(\tau, \omega) = \begin{cases} e^{-\omega\tau}/(e^{-\beta\omega} + 1) & \text{fermions} \\ \omega e^{-\omega\tau}/(e^{-\beta\omega} - 1) & \text{bosons} \end{cases} \quad (6.6)$$

and

$$A(\omega) = \begin{cases} \rho(\omega)/2\pi & \text{fermions} \\ \rho(\omega)/2\pi\omega & \text{bosons.} \end{cases} \quad (6.7)$$

(For some applications it may be more appropriate to define  $K(\tau, \omega) = e^{-\omega\tau}$  and  $A(\omega) = \rho(\omega)/2\pi(e^{-\beta\omega} - 1)$  in the bosonic case.) The *spectral function*  $A(\omega)$ , which we shall view as the main quantity of interest, is positive definite and satisfies a sum rule  $\int d\omega A(\omega) = \mathcal{N} < \infty$ .

Equation (6.5) tells us that we can interpret  $G(\tau)$  as a linear functional of  $A(\omega)$  with kernel  $K(\tau, \omega)$ . Hence, the analytic continuation is equivalent to the functional inversion  $A(\omega) = \mathbf{K}^{-1}[G(\tau)]$ . Only a finite inversion is practicable, however. If we discretize frequency and imaginary time using a uniform mesh (with spacings  $\Delta\tau$  and  $\Delta\omega$ ), then  $A_j = A(\Delta\omega \cdot j)\Delta\omega$  and  $G_k = G(\Delta\tau \cdot k)$  are related by  $A_j = \sum_k K_{jk}^{-1} G_k$ . The problem is thus reduced to a matrix inversion of

$$K_{kj} = \frac{e^{\Delta\omega\Delta\tau \cdot j \cdot k}}{e^{-\beta\Delta\omega \cdot j} \pm 1}. \quad (6.8)$$

This inversion is not an easy one to perform, however. The condition number of  $K_{jk}$  is extremely large: the matrix will have eigenvalues both

exponentially large and exponentially small in  $\beta$ . This means that computation of the inversion requires extremely high numerical precision [51]. Worse, the inversion problem is ill-posed and responds badly to any measurement error in the input set  $G_k$ . The inversion typically overfits the noise with spurious high-frequency modes in  $A_j$ .

The history of practical analytic continuation methods is one of continual refinement of the procedures for regularization of the matrix inversion. The simplest example of regularization is to try

$$A_j = \sum_k (K_{kj} + \lambda \delta_{kj})^{-1} G_k. \quad (6.9)$$

Since the high-frequency modes in  $A_j$  are generated by the smallest eigenvalues of  $K_{jk}$ , a nonzero value of  $\lambda$  will have the effect of suppressing those modes with eigenvalues on the order or  $\lambda$  or smaller. To see this, note that for each eigenvalue  $E$  of  $K_{jk}$ , there is an eigenvalue in the inverse matrix that is modified according to  $1/E \rightarrow 1/(E + \lambda)$ .

This naive scheme has two major flaws. First, filtering out the high frequency modes in this way has the effect of eliminating from the spectral function *all* fine structure below a certain frequency scale, whether spurious or real. Second, it does not ensure that  $A_j \geq 0$ , as required. The MEM, which we describe briefly in the next section, is considerably more sophisticated about what to filter and has nonnegativity built in.

### 6.3 Maximum Entropy Method

Suppose that to the exact function  $G(\tau)$  we have a measured approximation  $\bar{G}(\tau)$ . In practice, this will usually have been generated from some Monte Carlo simulation, so that

$$\bar{G}(\tau) = G(\tau) + \text{statistical noise}. \quad (6.10)$$

The goodness-of-fit functional

$$\chi^2[A] = \int_0^\beta \frac{d\tau}{\sigma(\tau)^2} \left| \int d\omega K(\tau, \omega) A(\omega) - \bar{G}(\tau) \right|^2 \quad (6.11)$$

measures how closely the correlation function generated from  $A(\omega)$  [via Eq. (6.5), the forward model] matches  $\bar{G}(\tau)$ . Here,  $\sigma(\tau)$  is the best-guess estimate of the total measurement error in  $\bar{G}(\tau)$ . (See Appendix A.6.) There is also an entropy associated with each spectral function,

$$\mathcal{S}[A] = - \int d\omega A(\omega) \ln (A(\omega)/D(\omega)), \quad (6.12)$$

which measures the information content of  $A(\omega)$ . Here,  $D(\omega)$  is the so-called *default model*, a smooth function that serves as the zero (maximum) entropy

configuration. Any features of the true spectral function known in advance can be encoded in  $D(\omega)$ .

It can be shown that the likelihood of any  $A(\omega)$  being the true spectral function is equal to  $\mathcal{P}[A] \sim e^{-Q[A]}$  where  $Q = \chi^2 - \alpha^{-1}\mathcal{S}$  (and  $\alpha^{-1}$  is a parameter that controls the degree of regularization). The MEM solution corresponds to the spectral function that minimizes  $Q$ . In practice, the minimization of  $Q$  is treated as a numerical optimization problem and is typically performed using the Newton-Raphson algorithm or some other gradient search technique. Nonetheless, a formal solution can be found by identifying the spectral function for which  $Q$  is stationary with respect to functional variation. The result, derived in Appendix A.7, is

$$\bar{A}(\omega) = e^{\alpha\mu} D(\omega) \exp \left[ -2\alpha \int_0^\beta \frac{d\tau}{\sigma(\tau)^2} \psi(\tau) K(\tau, \omega) \right] \quad (6.13)$$

where

$$\psi(\tau) = \int d\omega K(\tau, \omega) \bar{A}(\omega) - \bar{G}(\tau) \quad (6.14)$$

and  $\mu$  is a Lagrange multiplier chosen to enforce the normalization.

In two trivial limits, this set of equations can be solved exactly. When  $\alpha \rightarrow \infty$ , Eq. (6.13) demands that  $\psi \rightarrow 0$ . This yields the noisy, unregularized spectrum  $\bar{A}(\omega) = \mathbf{K}^{-1}[\bar{G}(\tau)]$ , which is the solution that minimizes  $\chi^2[A]$ . When  $\alpha \rightarrow 0$ ,  $\bar{A}(\omega) = D(\omega)$ , the smooth default function. This solution maximizes  $\mathcal{S}[A]$ . Note that these results come about because  $Q \sim \chi^2[A]$  and  $Q \sim -\mathcal{S}[A]$ , respectively, in the two limits.

Over the full range of intermediate values ( $0 < \alpha < \infty$ ), Eq. (6.13) constitutes a one-parameter family of solutions interpolating between these two extremes. An additional condition must be imposed to remove this ambiguity, *i.e.*, to turn the family of solutions into a single final spectrum. In *classic* MEM, one takes the point of view that somewhere between overfitting and over-smoothing lies an ideal intermediate range centred on some optimal value of  $\alpha$ . In other schemes, the final result is produced by averaging,  $\bar{A}(\omega) = \int_0^\infty d\alpha w(\alpha) \bar{A}(\alpha, \omega) / \int_0^\infty d\alpha w(\alpha)$ , in which case the question becomes which weighting function  $w(\alpha)$  to use. In their definitive review [24], Jarrel and Gubernatis address these issues in greater detail.

## 6.4 The Stochastic Approach

In this section and the next, we introduce the stochastic analytic continuation approach and demonstrate how it is related to the MEM. To start, consider a smooth mapping  $\phi : \mathbb{R} \mapsto [0, 1]$ , which takes the frequency domain of the spectral function onto the unit interval. Such a function will be of the form

$$\phi(\omega) = \frac{1}{\mathcal{N}} \int_{-\infty}^{\omega} d\nu D(\nu) \quad (6.15)$$

where  $D = \mathcal{N}\phi'$  is positive definite and (like  $A$ ) normalized to  $\mathcal{N}$  but otherwise arbitrary. (We use the notation  $D$  for the mapping's kernel in anticipation of identifying it with the default model of the MEM.) Then,

$$1 = \frac{1}{\mathcal{N}} \int d\omega A(\omega) = \int d\phi(\omega) \frac{A(\omega)}{D(\omega)} = \int_0^1 dx n(x). \quad (6.16)$$

In the last line, we have made the change of variables  $x = \phi(\omega)$  and introduced the dimensionless field

$$n(x) = \frac{A(\phi^{-1}(x))}{D(\phi^{-1}(x))}. \quad (6.17)$$

Under this change of variables, Eq. (6.11) becomes

$$H[n(x)] = \int_0^\beta \frac{d\tau}{\sigma(\tau)^2} \left| \int_0^1 dx \hat{K}(\tau, x) n(x) - \bar{G}(\tau) \right|^2 \quad (6.18)$$

with  $\hat{K}(\tau, \phi(\omega)) = K(\tau, \omega)$ . We take the point of view that Eq. (6.18) is the Hamiltonian for the system of classical fields  $\{n(x)\}$ . Then, supposing the system is held fixed at a fictitious inverse temperature  $\alpha$ , it has a partition function  $Z = \int dn e^{-\alpha H[n]}$  with a measure of integration

$$\int dn = \int_0^\infty \left( \prod_x dn(x) \right) \delta \left( \int_0^1 dx n(x) - 1 \right). \quad (6.19)$$

The thermally averaged value of the field is

$$\langle n(x) \rangle = \frac{1}{Z} \int dn n(x) e^{-\alpha H[n]}. \quad (6.20)$$

The corresponding ‘‘thermally regulated’’ spectral function,

$$\langle A(\omega) \rangle = \langle n(\phi(\omega)) \rangle D(\omega), \quad (6.21)$$

can be recovered using Eq. (6.17).

At zero temperature ( $\alpha \rightarrow \infty$ ), Eq. (6.20) simply picks out the ground-state field configuration; the corresponding spectral function is the unregularized analytic continuation result. In the high temperature limit ( $\alpha \rightarrow 0$ ), Eq. (6.20) represents an *unweighted* average over all possible field configurations. In that case, the average is completely independent of the input function  $\bar{G}(\tau)$  and as such can only yield the zero-information result  $\langle n(x) \rangle = 1$ . From Eq. (6.17), it follows that  $D(\omega)$  is the corresponding spectral function.

These limits are precisely those of the MEM, which we discussed at the end of Sect. 6.3. Note that the kernel of the mapping in Eq. (6.15) plays the same role as the MEM's default model and the fictitious temperature the same role as the MEM's regularization parameter.

## 6.5 Approximate Solutions

Now let us extend our “interacting classical field” analogy a little further. Expanding the square in Eq. (6.18), we can cast the Hamiltonian in the familiar form

$$H[n(x)] = \int_0^1 dx \epsilon(x)n(x) + \frac{1}{2} \int_0^1 dx dy V(x,y)n(x)n(y), \quad (6.22)$$

with a free dispersion

$$\epsilon(x) = -2 \int_0^\beta \frac{d\tau}{\sigma(\tau)^2} \bar{G}(\tau) \hat{K}(\tau, x) \quad (6.23)$$

and an interaction term

$$V(x, y) = V(y, x) = 2 \int_0^\beta \frac{d\tau}{\sigma(\tau)^2} \hat{K}(\tau, x) \hat{K}(\tau, y). \quad (6.24)$$

*Noninteracting system*—Let us ignore the interaction term for a moment and proceed by setting  $V = 0$ . Then, if we represent the delta function constraint in Eq. (6.19) with an integral representation

$$\delta(X) = \int_{-\infty}^{\infty} d\zeta \exp(i\zeta X), \quad (6.25)$$

the partition function is simply  $\mathcal{Z} = \int_{-\infty}^{\infty} d\zeta e^{-i\zeta} \mathcal{Z}(\zeta)$ , where

$$\mathcal{Z}(\zeta) = \int_0^\infty \left( \prod_x dn(x) \right) e^{-\int_0^1 dx (\alpha\epsilon(x) - i\zeta)n(x)}. \quad (6.26)$$

The saddle point solution for the field is

$$\bar{n}(x) = \frac{\delta}{\delta\epsilon(x)} \left( -\frac{1}{\alpha} \ln Z(\bar{\zeta}) \right) = e^{-\alpha(\epsilon(x) - \mu)}. \quad (6.27)$$

This says that the fields are Maxwell-Boltzmann distributed according to their energy as measured with respect to a chemical potential  $\mu \equiv i\bar{\zeta}/\alpha$ , which is chosen such that  $\int_0^1 dx \bar{n}(x) = 1$ .

*Mean field treatment*—Now let us reintroduce  $V$ . Assuming that fluctuations of the  $n(x)$  field about its mean value are negligible,

$$(n(x) - \bar{n}(x))(n(y) - \bar{n}(y)) \approx 0, \quad (6.28)$$

the Hamiltonian has a mean field form

$$H_{\text{MF}} = \int_0^1 dx E(x)n(x) + \text{const.}, \quad (6.29)$$

where

$$E(x) = \left. \frac{\delta H[n]}{\delta n(x)} \right|_{n=\bar{n}} = \epsilon(x) + \int dy V(x, y) \bar{n}(y). \quad (6.30)$$

Equation (6.29) leads to the saddle point solution given by Eq. (6.27) but now with  $\epsilon(x)$  replaced by  $E(x)$ . Using the definition of  $E(x)$  from Eq. (6.30), we arrive at the self-consistent equation

$$\bar{n}(x) = e^{\alpha\mu} \exp \left[ -\alpha \left( \epsilon(x) + \int dy V(x, y) \bar{n}(y) \right) \right]. \quad (6.31)$$

Again,  $\mu$  is a chemical potential used to fix the normalization.

Now consider the reverse change of variables taking  $n(x)$  back to  $A(\omega)$ . With only a little effort, one can show that Eq. (6.31) is identical to Eq. (6.13). What this tells us is that the mean field treatment of the classical field system is *formally equivalent to the MEM*.

We can make this equivalence more explicit still. The free energy density of the system we have just described is  $F = U - \alpha^{-1}S - \mu$ , where the internal energy is given by  $U = H[\bar{n}(x)]$  and the entropy (see Appendix A.8) by

$$S[\bar{n}] = - \int_0^1 dx \bar{n}(x) \ln \bar{n}(x). \quad (6.32)$$

As we saw earlier, Eqs. (6.11) and (6.18) are connected by a change of variables. Similarly,

$$\begin{aligned} S[\bar{n}] &= - \int_0^1 dx \bar{n}(x) \ln \bar{n}(x) \\ &= - \int d\phi(\omega) \frac{\bar{A}(\omega)}{D(\omega)} \ln \left( \frac{\bar{A}(\omega)}{D(\omega)} \right) \\ &= - \int d\omega \bar{A}(\omega) \ln \left( \frac{\bar{A}(\omega)}{D(\omega)} \right) = \mathcal{S}[\bar{A}], \end{aligned} \quad (6.33)$$

where the final equality follows from comparison with Eq. (6.12). Thus,  $\chi^2 = H[\bar{n}(x)]$  and  $\mathcal{S} = S[\bar{n}(x)]$ , which makes clear that  $F\mathcal{N} = Q = \chi^2 - \alpha^{-1}\mathcal{S} - \mu\mathcal{N}$ . This means that the MEM solution is just the one that minimizes the free energy of the  $\{n(x)\}$  system at the mean field level.

## 6.6 Monte Carlo Evaluation

### 6.6.1 Configurations and Update Scheme

The energy of a field configuration, given by Eq. (6.18), can be written in the form

$$H[n(x)] = \int_0^\beta d\tau h(\tau)^2, \quad (6.34)$$

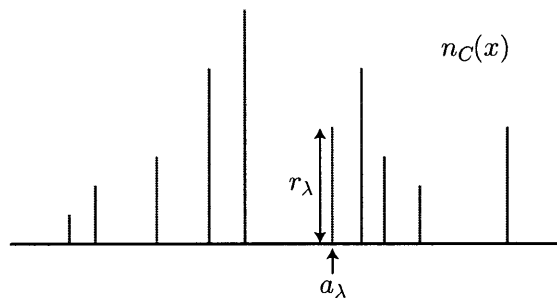


Figure 6-1: A field configuration of delta functions  $n_C(x)$  is specified by a set  $C = \{r_\gamma, a_\gamma\}$  of residues and coordinates.

where

$$h(\tau) = \frac{1}{\sigma(\tau)} \int_0^1 dx \hat{K}(\tau, x) n(x) - g(\tau) \quad (6.35)$$

and  $g(\tau) = \bar{G}(\tau)/\sigma(\tau)$  is the input Green's function rescaled by the variance.

Computing  $\langle n(x) \rangle$  requires that we integrate over all possible field configurations. To accomplish this, we need some ansatz to render the measure  $dn$  finite. One choice is to represent each field configuration as a superposition of delta functions. In that case, we can parameterize each configuration by a set of residues and coordinates  $C = \{r_\gamma, a_\gamma\}$  satisfying  $r_\gamma > 0$ ,  $0 \leq a_\gamma \leq 1$ , and  $\sum_\gamma r_\gamma = 1$ . The corresponding field configuration is

$$n_C(x) = \sum_\gamma r_\gamma \delta(x - a_\gamma). \quad (6.36)$$

The partition function  $\mathcal{Z} = \int dC \exp(-\alpha H_C)$  has a new, computationally tractable measure

$$\int dC = \prod_\gamma \int_0^\infty dr_\gamma \int_0^1 da_\gamma \delta\left(\sum_\gamma r_\gamma - 1\right). \quad (6.37)$$

In order to calculate the energy  $H_C$  of a given configuration via Eq. (6.34), we shall need the relation

$$\begin{aligned} g(\tau) + h_C(\tau) &= \frac{1}{\sigma(\tau)} \int_0^1 dx \hat{K}(\tau, x) n_C(x) \\ &= \frac{1}{\sigma(\tau)} \sum_\gamma r_\gamma \hat{K}(\tau, a_\gamma). \end{aligned} \quad (6.38)$$

Now suppose that the configuration is modified ( $C \mapsto C'$ ) by altering the

parameters in some subset  $\Lambda$  of the delta function walkers:

$$\begin{aligned} r_\gamma &\mapsto r'_\gamma = r_\gamma + \sum_{\lambda \in \Lambda} \delta_{\gamma\lambda} \Delta r_\lambda, \\ a_\gamma &\mapsto a'_\gamma = a_\gamma + \sum_{\lambda \in \Lambda} \delta_{\gamma\lambda} \Delta a_\lambda. \end{aligned} \quad (6.39)$$

Accordingly,  $h_C \mapsto h_{C'} = h_C + \Delta h$ , where

$$\Delta h(\tau) = \frac{1}{\sigma(\tau)} \sum_{\lambda \in \Lambda} \left[ r'_\lambda \hat{K}(\tau, a'_\lambda) - r_\lambda \hat{K}(\tau, a_\lambda) \right]. \quad (6.40)$$

The configuration energy changes to

$$\begin{aligned} H_{C'} &= \int_0^\beta d\tau (h_C(\tau) + \Delta h(\tau))^2 \\ &= H_C + \int_0^\beta d\tau \Delta h(\tau) [2h_C(\tau) + \Delta h(\tau)]. \end{aligned} \quad (6.41)$$

The Monte Carlo procedure is to calculate  $H_C$  and  $h_C(\tau)$  for some arbitrary starting configuration  $C$  and then update them whenever a walk is accepted. Acceptance is determined according to the usual Metropolis algorithm: create a modified trial configuration and compute its energy shift  $\Delta H = H_{C'} - H_C$  following Eq. (6.41); choose a random real number  $\xi \in [0, 1]$ ; if  $\exp(-\alpha \Delta H) > \xi$ , accept the walk and update

$$\begin{aligned} H_C &\mapsto H_{C'} = H_C + \Delta H, \\ h_C &\mapsto h_{C'} = h_C + \Delta h. \end{aligned} \quad (6.42)$$

The path of the delta function walkers through the configuration space must be normalization-conserving and must satisfy detailed balance. Moreover, the entire phase space must, in principle, be accessible. Only two types of moves are necessary to meet these criteria: (1) coordinate shifting moves, in which the walker  $\lambda$  is translated by a distance  $\Delta a_\lambda$ , and (2) weight sharing moves, in which the total residue of a subset of walkers is reapportioned amongst themselves such that  $\sum_\gamma r_\gamma = 1$  is preserved.

It is useful, however, to introduce additional weight sharing moves that also conserve higher moments

$$\mathcal{M}^{(n)} = \int_0^1 dx n(x) x^n = \sum_\gamma r_\gamma a_\gamma^n. \quad (6.43)$$

Sandvik has shown that such moves dramatically improve the acceptance ratio of attempted walks at low temperature. At a minimum we want to consider walks that preserve the overall normalization  $\mathcal{M}^{(0)} = 1$ . But we also consider rearrangements of weight between  $n > 2$  walkers that conserve

the first  $n - 1$  moments. Such a move can be effected as follows. Let  $\tilde{\Lambda} = \{\lambda_2, \dots, \lambda_n\}$  and  $\Lambda = \{\lambda_1, \dots, \lambda_n\}$ . Defining the scale factors

$$Q_\lambda = \begin{cases} -1 & \text{if } \lambda = \lambda_1 \\ \frac{\prod_{\mu \in \tilde{\Lambda}} (a_\mu - a_{\lambda_1})}{\prod_{\mu \in \tilde{\Lambda}} (a_\mu - a_\lambda)} & \text{if } \lambda \in \tilde{\Lambda}, \end{cases} \quad (6.44)$$

we can express the changes in residue as

$$r'_\lambda = r_\lambda + \Delta r_\lambda = r_\lambda - s Q_\lambda, \quad (6.45)$$

where  $s$  parameterizes the one-dimensional line of constraint through the  $n$ -dimensional space of residues. In order to preserve the positivity of the residues, we must impose  $r'_\lambda > 0$ . Hence, we need to ensure that  $r_\lambda > Q_\lambda \Delta r_\lambda$  for all  $\lambda \in \Lambda$ . Accordingly, we take  $s$  to be randomly distributed in the interval

$$\max_{\lambda \in \Lambda^-} (r_\lambda / Q_\lambda) < s < \min_{\lambda \in \Lambda^+} (r_\lambda / Q_\lambda), \quad (6.46)$$

where  $\Lambda^- = \{\lambda : Q_\lambda < 0\}$  and  $\Lambda^+ = \{\lambda : Q_\lambda > 0\}$ .

### 6.6.2 Parallel Tempering

The Monte Carlo algorithm described above can be improved by introducing parallel tempering [52]. The idea is to allow multiple instantiations of the simulation to proceed simultaneously for a variety of parameters  $\{\alpha_0, \alpha_1, \dots, \alpha_N\}$  covering a large range of inverse temperatures. The temperature profile is arbitrary, but we shall find it convenient to choose a constant ratio  $\alpha_{p+1}/\alpha_p = R$  between one temperature layer and the next.

Most important, the field configurations in each layer are made to evolve in parallel but not independently. Configurations are swapped between adjacent layers in a way that preserves detailed balance and ensures that each layer  $p$  will eventually settle into thermal equilibrium at inverse temperature  $\alpha_p$ . The update rule is quite simple: given two adjacent layers  $p$  and  $q = p \pm 1$ , choose a random real number  $\xi \in [0, 1]$  and swap the  $p$  and  $q$  configurations if

$$\exp\left[(\alpha_p - \alpha_q)(H_p - H_q)\right] > \xi. \quad (6.47)$$

Parallel tempering eliminates the need for a separate, initial annealing stage [25]. Because the simulation simultaneously samples over a large temperature range, there is no danger of getting trapped in false minima: the interlayer walks always provide a cheap pathway between configurations separated by large energy barriers. All that is required is to let the system thermalize for some time before sampling (*i.e.*, before actually beginning to bin and tabulate the field configurations). By tracking the average acceptance rates for swaps between layers, it is straightforward to determine when the system has equilibrated. Figure 6-2 shows a sample run (for a test case to

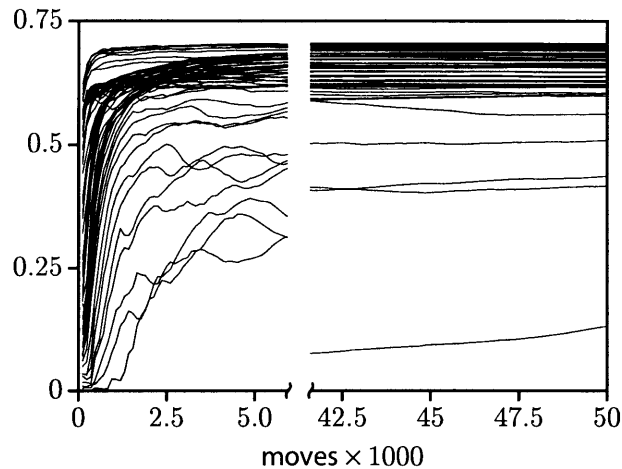


Figure 6-2: The acceptance ratio of configuration swaps between adjacent levels ( $\alpha_p \leftrightarrow \alpha_{p+1}$ ) evolves as a function of the number of updates performed. When the system is fully thermalized, the acceptance ratios stabilize to asymptotic values.

be described in Sect. 6.8). We see that on a stochastic time-scale of several tens of thousands of moves, each temperature layer settles into thermal equilibrium.

An additional advantage of the parallel tempering algorithm is that it yields in one run a complete temperature profile of all the important thermodynamic variables. In the next section, we discuss how we can put that information to use.

## 6.7 Critical Temperature

The Monte Carlo simulation yields a set of thermally averaged field configurations  $\{\langle n(x) \rangle_{\alpha_p} : p = 0, 1, \dots, N\}$ . With little additional effort, we can also keep track of the internal energies  $\{U(\alpha_p) = \langle H[n] \rangle_{\alpha_p} : p = 0, 1, \dots, N\}$ . In this section, we propose a final candidate spectral function constructed from only these quantities.

To start, note that the specific heat can be written as

$$C(\alpha_p) = \left. \frac{dU(\alpha)}{d(\alpha^{-1})} \right|_{\alpha=\alpha_p} \approx \frac{a_p U(\alpha_p)}{\ln R} \frac{d \ln U(\alpha_p)}{dp}. \quad (6.48)$$

(See Appendix A.9.) In Fig. 6-3,  $\ln U(\alpha_p)$  is plotted for each temperature level. The knee in the function, occurring in the vicinity of the level  $p = p^*$ , indicates there is a jump in the specific heat. At low temperatures ( $\alpha > \alpha^* \equiv \alpha_{p^*}$ ), the system freezes out and the correlations  $\langle n(x)n(y) \rangle - \langle n(x) \rangle \langle n(y) \rangle$

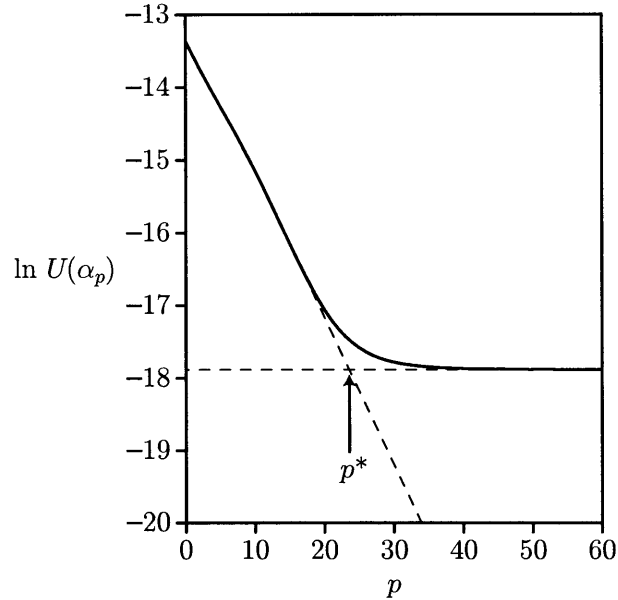


Figure 6-3: The internal energy of the  $\{n(x)\}$  system at each temperature layer is plotted. The knee at  $p = p^*$ , corresponding to a jump in the specific heat, signals a thermodynamic phase transition.

become short-ranged. There is a characteristic energy scale  $E^* = U(\alpha^*)$  associated with this phase transition.

Recall that in the *microcanonical ensemble*, the average over all configurations having energy  $E$  is given by

$$\langle n(x) \rangle_E = \int dn n(x) \delta(E - H[n]). \quad (6.49)$$

We propose that the final spectrum be defined as

$$\langle\langle n(x) \rangle\rangle = \frac{1}{E^*} \int_0^{E^*} dE \langle n(x) \rangle_E, \quad (6.50)$$

which sums over all field configurations in the ordered phase (*i.e.*, configurations with energies  $E$  satisfying  $0 \leq E < E^*$ ). Roughly speaking, this amounts to performing an unbiased average over all spectral functions  $A$  that surpass the fitting threshold  $\chi^2[A] < E^*$ .

Since the Monte Carlo simulation is performed at fixed temperature, however, we must make the change of variables  $dE = (dU/d\alpha)d\alpha$ . Equation (6.50) becomes

$$\langle\langle n(x) \rangle\rangle = \frac{1}{U(\alpha^*)} \int_{\alpha^*}^{\infty} d\alpha \left( -\frac{dU}{d\alpha} \right) \langle n(x) \rangle_{\alpha}. \quad (6.51)$$

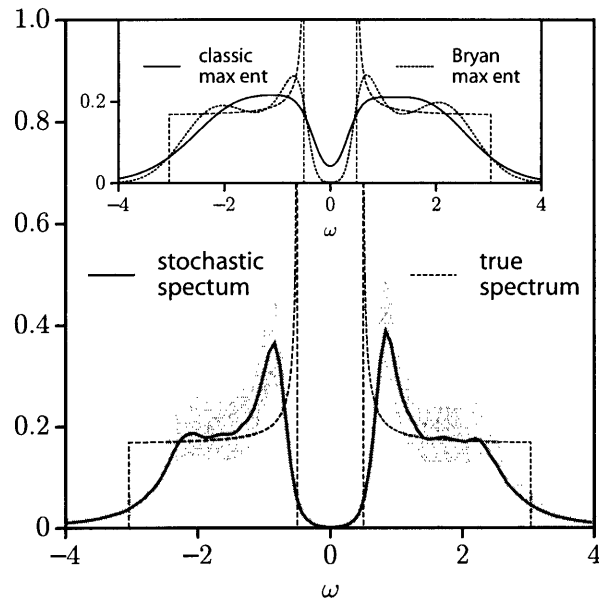


Figure 6-4: The stochastic analytic continuation method is used to extract the spectrum of a BCS superconductor (bandwidth  $W = 6$  and gap  $2\Delta = 1$ ) from noisy data. The grey region indicates the statistical uncertainty of the computed spectrum. The inset shows the classic and Bryan MEM results.

The discretized version of this integral is

$$\langle\langle n(x) \rangle\rangle = \frac{\sum_{p=p^*}^{N-1} (U(\alpha_p) - U(\alpha_{p+1})) \langle n(x) \rangle_{\alpha_p}}{U(\alpha_{p^*}) - U(\alpha_N)}. \quad (6.52)$$

## 6.8 BCS Test Case

We showed in Sect. 6.5 that the stochastic analytic continuation method is a dynamical generalization of the MEM. The question remains, What is gained by going beyond the mean field calculation? Our contention is that the stochastic method is better able to resolve sharp spectral features buried in noisy data. To illustrate this point, we have taken the spectrum of a BCS superconductor—which contains flat regions, steep peaks, and sharp gap edges—as a test case. The exact spectral function is

$$A(\omega) = \begin{cases} \frac{1}{W} \frac{|\omega|}{\sqrt{\omega^2 - \Delta^2}} & \text{if } \Delta < |\omega| < W/2 \\ 0 & \text{otherwise,} \end{cases} \quad (6.53)$$

where  $W$  is the bandwidth and  $2\Delta$  the gap magnitude.

From Eq. (6.53) we generated an exact  $G(\tau)$  using the forward model. We then applied random error to the function to create an approximate  $\tilde{G}(\tau)$ ,

which was made to serve as the input data for our stochastic algorithm and for two flavours of the MEM—the classic method and a method due to Bryan [53] (both described in Ref. [24]). Figure 6-4 shows these computed spectra alongside the exact result.

The most striking aspect of the comparison is that the stochastically generated spectrum does a superior job of modelling the gap. It closely follows the trough of the gap and captures some of the sharpness of the peaks at the gap edges. The MEM spectra, on the other hand, are much too smooth. The classic MEM spectrum is especially poor. It is at best a caricature of the true BCS spectrum: the sharp features are completely washed out and the depression at  $\omega = 0$  is not a fully developed gap.

Bryan’s algorithm does a somewhat better job of reproducing the gap and its adjacent peaks, but in doing so it also forms a second pair of spurious humps around  $\omega = 2$ . In our experience, this is typical behaviour. The MEM method has trouble making sudden transitions from regions of high to low curvature. What one tends to get is a smooth curve gently oscillating around the correct result. The stochastic method, in contrast, seems to have no trouble generating a flat region next to a sharp peak.

## 6.9 Summary

In this paper, we have made the case that the MEM is not the best method for extracting spectral information from imaginary time data. Instead, we advocate the use of the stochastic analytic continuation method. Our claim is that the stochastic method is at least as good as the MEM and may even surpass it for a broad class of problems in which the spectrum to be extracted has very sharp features.

This is a difficult point to argue convincingly. New analytic continuation methods tend to face considerable resistance, and claims of superiority on their behalf are met (quite rightly) with a high degree of skepticism. The MEM has a record of years of successful use in a variety of settings; plus, it offers the comfort of a seemingly rock-solid mathematical rationale. Competing schemes tend to lack any clear justification other than a few tantalizing examples of their performance in a handful of test cases.

The prevailing opinion is that the MEM is the definitive “solution” to the analytic continuation problem. Some other method may produce better spectra in particular special cases, but as a general method, the MEM has to win out. The thinking goes: no other algorithm can outperform the MEM because its solution is, by construction, the unique, best candidate spectrum—a claim that rests on the firm foundation of Bayesian logic.

What this line of reasoning misses, however, is the possibility that an average of *many* likely candidates might better reproduce the true spectral function than does the *single* most likely spectrum. To give a path integral analogy, we would argue that including fluctuations about a saddle point solution (the single most likely field configuration) can yield a result closer

to the full integral. This is how we go about justifying the stochastic analytic continuation method.

Let us be careful about what can be established rigorously. To be precise, the standard conditional probability analysis used to derive the MEM proves only that the most likely spectrum belongs to the family of solutions (parameterized by  $\alpha^{-1}$ ) that minimizes  $Q = \chi^2 - \alpha^{-1}S$ . From our point of view, then, what is required of an averaging method is that it produce at the mean field level a family of solutions that coincides with the MEM result. The stochastic method, as we have formulated it, does exactly this—under the guise of minimizing the free energy  $FN (= Q)$  of a system of classical fields at a fictitious temperature  $\alpha^{-1}$ .

This correspondence gives us a new way of thinking about the MEM solution. We know that even though a path integral contains jagged, discontinuous field configurations, its saddle point solution is always a smooth, continuous function. This highlights the main deficiency of the MEM—that it fails to model well spectral functions that are not sufficiently smooth—and makes clear why the stochastic method does not suffer from the same limitation.

Another advantage of the stochastic approach is that it helps us to talk about the analytic continuation problem using a more physical language. Having identified the regularization parameter as a temperature, we can ask how the system behaves thermodynamically. The answer, we have suggested, is that the system exhibits ordered and disordered phases that can be interpreted as the good-fitting and ill-fitting regimes. We believe that this gives a much more intuitive picture than does the somewhat obscure probability analysis of the MEM.

We close with a recapitulation of the main results. We have presented a new variant of the stochastic analytic continuation method that differs from Sandvik's original prescription as follows: as a matter of mathematical formulation, it includes an additional internal freedom that turns out to be equivalent to specifying a default model; as a matter of practical implementation, it is built on a delta function walker scheme and takes advantage of parallel tempering. We have proved that the mean field version of this stochastic method is equivalent to the MEM. Our tests suggest that it outperforms the MEM for spectra with sharp features and fine structure.

## Chapter 7

# Conclusions

We have investigated the effect of an applied magnetic field on the Kondo insulator ground state, using mean field calculations (in the thermodynamic limit) and QMC simulations (on small lattices). From these numerical results, a consistent picture emerges:

1. In the  $J > J_c$  local singlet phase, the spin up and spin down quasiparticle bands respond to a small applied field by shifting with respect to one another, thus reducing the charge gap.
2. When  $|B| \sim 2\Delta_K$  (Kondo energy scale), the spin gap closes, and the system undergoes a continuous transition to a canted antiferromagnetic state. Initially, the local spins cant *with* and the electron moments cant *against* the applied field. The charge gap, which had nearly closed, reinflates, driven now by the magnetic order.
3. When the antiferromagnetism first appears, there are still low-weight heavy-fermion peaks close to the gap in the single-particle spectral function. As these peaks are Zeeman shifted, their spectral weight is rearranged so as to hop over the gap. In this way, the antiferromagnetism protects the charge gap and delays its closing.
4. For  $|B| \sim \sqrt{2\Delta_K W}$  (hybridization energy scale), the staggered moment and charge gap collapse to exponentially small values. The persistence of antiferromagnetic order in the square-lattice case is an artifact of perfect nesting. In a less idealized system, the state would be a true metal. The appearance of the metallic state at high fields is related to the quenching of the local moments and their decoupling from the conduction electrons.

A large part of the work for this thesis involved the development and refinement of numerical methods for QMC simulation. Some of these advances are widely applicable and not necessarily limited to the KLM. Indeed, while the the Kondo lattice problem was often motivation for those efforts, it was sometimes simply a convenient test case for new ideas.

1. We have shown that lattice fermion systems subject to a broad class of constraints can be simulated using the BSS or other determinant quantum Monte Carlo methods simply by introducing an additional set of gauge fields that live on the links between the time slices.
2. We have presented a modified version of the BSS algorithm that alternately updates the interaction and constraint fields as it steps through the time slices.
3. Some of the matrix multiplications in the BSS algorithm introduce sizeable rounding errors and degrade the stability of the simulation. This becomes a serious problem at low temperatures. We have presented a numerical stabilization method, based on some rather simple matrix manipulations, that is as fast as the methods currently in use but significantly less difficult to implement.
4. The maximum entropy method is often unable to extract spectral information reliably if the input data is too noisy or the spectrum contains sharp features. We have argued that the stochastic analytic continuation method does a better job in these circumstances. We have shown that it can be understood as a dynamic generalization of the maximum entropy method.
5. We have also described two minor technical innovations. First, our implementation of the stochastic analytic continuation method makes use of arbitrarily-positioned delta-function walkers that have no intrinsic discretization error. Second, adding parallel tempering updates leads to a more reliable traversal of the phase space. Convergence is improved and false minima are generally avoided.

# Appendix A

## Appendices

### A.1 Effective Spin Hamiltonian

It is useful to express the Hamiltonian as a sum  $\hat{H} = \hat{H}_t + \hat{H}_{JB}$  of its inter-site and onsite parts:

$$\begin{aligned}\hat{H}_t &= - \sum_{ij} t_{ij} c_i^\dagger c_j, \\ \hat{H}_{JB} &= J \sum_i \frac{1}{2} c_i^\dagger \boldsymbol{\sigma} c_i \cdot \hat{\mathbf{S}}_i - B \sum_i \left( \frac{1}{2} c_i^\dagger \sigma^3 c_i + \hat{S}_i^3 \right).\end{aligned}\tag{A.1}$$

The hopping matrix is defined so that  $t_{ij} = t$  when sites  $i$  and  $j$  are adjacent and  $t_{ij} = 0$  otherwise.

The Hamiltonian operator acts in the space  $\mathcal{F}$ , which is a product of the Fock space of the conduction electrons and the  $SU(2)$  space of the fixed spins. The states  $|\{n_{i\uparrow}, n_{i\downarrow}\}\rangle \otimes |\{s_j\}\rangle$  in the number/spin-projection representation serves as a convenient basis. This Hilbert space admits a decomposition  $\mathcal{F} = \mathcal{F}_1 \cup \mathcal{F}_2$ , where  $\mathcal{F}_1$  contains all the states with exactly one electron per site (*viz.*, those satisfying  $\forall i, n_{i\uparrow} + n_{i\downarrow} = 1$ ) and  $\mathcal{F}_2$  the rest (those satisfying  $\exists i$  such that  $n_{i\uparrow} + n_{i\downarrow} \neq 1$ ). The first subspace is spin only, whereas the second contains all possible charge excitations.

We introduce projection operators  $\hat{P}_1^2 = \hat{P}_1$  and  $\hat{P}_2^2 = \hat{P}_2$  that map onto the  $\mathcal{F}_1$  and  $\mathcal{F}_2$  subspaces. Since  $\mathcal{F}_1$  and  $\mathcal{F}_2$  are disjoint but cover  $\mathcal{F}$ , the projection operators are orthogonal ( $\hat{P}_1 \hat{P}_2 = 0$ ) and complete ( $\hat{1} = \hat{P}_1 + \hat{P}_2$ ). Note that only  $\hat{H}_t : \mathcal{F}_1 \rightarrow \mathcal{F}_2$  takes states *between* the two subspaces. ( $\hat{H}_{JB}$  maps  $\mathcal{F}_1 \rightarrow \mathcal{F}_1$  and  $\mathcal{F}_2 \rightarrow \mathcal{F}_2$ .) Accordingly,  $\hat{P}_1 \hat{H}_t \hat{P}_1 = \hat{P}_1 \hat{H}_{JB} \hat{P}_2 = 0$ , which implies that

$$\begin{aligned}\hat{H} &= \hat{1} \hat{H} \hat{1} = \hat{P}_1 \hat{H}_{JB} \hat{P}_1 + \hat{P}_1 \hat{H}_t \hat{P}_2 \\ &\quad + \hat{P}_2 \hat{H}_t \hat{P}_1 + \hat{P}_2 (\hat{H}_t + \hat{H}_{JB}) \hat{P}_2.\end{aligned}\tag{A.2}$$

The resolvent operator  $\hat{G}(E) = (E - \hat{H})^{-1}$ , when restricted to  $\mathcal{F}_1$ , can

be cast into the same functional form by making the identification

$$\hat{P}_1 G(E) \hat{P}_1 = (E - \hat{\mathcal{H}}(E))^{-1}. \quad (\text{A.3})$$

Here,  $\hat{\mathcal{H}}(E)$  is some energy-dependent Hamiltonian-like operator. Using a  $2 \times 2$  matrix notation to denote its action in the  $\mathcal{F}_1$  and  $\mathcal{F}_2$  subspaces, we can write the resolvent operator as

$$\hat{G}(E) = \begin{pmatrix} E - \hat{H}_{JB} & -\hat{H}_t \\ -\hat{H}_t & E - \hat{H}_t - \hat{H}_{JB} \end{pmatrix}^{-1}. \quad (\text{A.4})$$

Making use of the identity

$$\begin{pmatrix} A & B \\ C & D \end{pmatrix}_{11}^{-1} = (A - BD^{-1}C)^{-1}, \quad (\text{A.5})$$

we find that

$$\hat{G}(E)_{11} = \left[ E - \hat{H}_{JB} - \hat{H}_t (E - \hat{H}_t - \hat{H}_{JB})^{-1} \hat{H}_t \right]^{-1} \quad (\text{A.6})$$

and thus, via Eq. (A.3),

$$\hat{\mathcal{H}}(E) = \hat{P}_1 \left[ \hat{H}_{JB} + \hat{H}_t (E - \hat{H})^{-1} \hat{H}_t \right] \hat{P}_1. \quad (\text{A.7})$$

Associated with  $\hat{\mathcal{H}}(E)$  is a one-parameter family of lowest eigenstates  $\{|\psi(E)\rangle \in \mathcal{F}_1\}$ . The true ground state is given by  $|\psi_1\rangle = |\psi(E_1)\rangle$ , where  $E_1 = \langle \psi(E_1) | \hat{\mathcal{H}}(E_1) | \psi(E_1) \rangle$  is simultaneously the lowest energy level in the  $\mathcal{F}_1$  subspace and the overall ground state energy. The lowest state in the  $\mathcal{F}_2$  sector is  $|\psi_2\rangle$ , having energy  $E_2 = E_1 + \Delta$ . [Figure A-1 shows how to compute the value of the energy separation  $\Delta$  in the atomic limit ( $J \gg t$ ).] For small excitation energies  $\epsilon$  above the ground state,

$$\hat{\mathcal{H}}(E_1 + \epsilon) = \hat{\mathcal{H}}(E_1) (1 + \mathcal{O}(\epsilon/\Delta)). \quad (\text{A.8})$$

Hence, we can identify  $\hat{\mathcal{H}}^{\text{eff}} = \hat{\mathcal{H}}(E_1)$  as the effective low-energy Hamiltonian in the spin sector:

$$\begin{aligned} \hat{\mathcal{H}}^{\text{eff}} &= \hat{P}_1 \left[ \hat{H}_{JB} + \hat{H}_t (E_1 - \hat{H})^{-1} \hat{H}_t \right] \hat{P}_1 \\ &= \hat{P}_1 \left[ \hat{H}_{JB} - \frac{1}{\Delta} \hat{H}_t \left( 1 + \frac{1}{\Delta} (\hat{H} - E_2) \right)^{-1} \hat{H}_t \right] \hat{P}_1 \\ &= \hat{P}_1 \hat{H}_{JB} \hat{P}_1 - \frac{1}{\Delta} \hat{P}_1 \hat{H}_t^2 \hat{P}_1 \\ &\quad + \sum_{n=1}^{\infty} \frac{1}{\Delta^{n+1}} \hat{P}_1 \hat{H}_t (\hat{H} - E_2)^n \hat{H}_t \hat{P}_1. \end{aligned} \quad (\text{A.9})$$

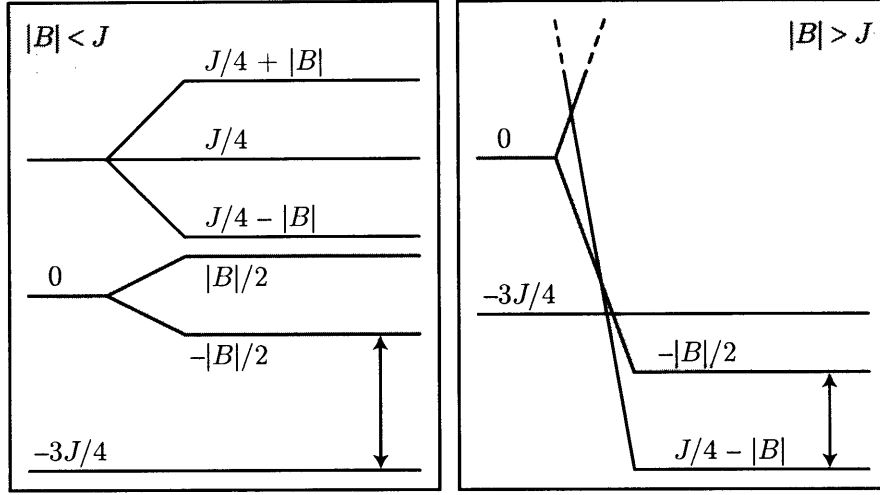


Figure A-1: In the atomic limit, the kinetic energy of the electrons is negligible. Accordingly, the spectrum at each site is a function of the net magnetic moment only. When there is a single electron on a site ( $n = 1$ ), it pairs with the localized spin to form a spin-0 singlet or spin-1 triplet state. At an unoccupied or doubly occupied site ( $n = 0, 2$ , highlighted), only the localized spin-1/2 contributes. Perturbing the ground state ( $\{n_i = 1\}$ ) by moving one electron to an adjacent site ( $\{n'_i\} = \{1, \dots, 1, 0, 2, 1, \dots, 1\}$ ) costs twice the energy indicated (with arrows) in the figure. Hence, the energy difference between the  $\mathcal{F}_1$  ground state and the lowest  $\mathcal{F}_2$  state is  $\frac{1}{2}(3J - 2|B|)$  if  $|B| < J$  and  $\frac{1}{2}(2|B| - J)$  if  $|B| > J$ .

The first term in  $\hat{\mathcal{H}}^{\text{eff}}$  can be dealt with easily. In the  $\mathcal{F}_1$  subspace, the local moment of the conduction electrons behaves as a spin-1/2 degree of freedom. Writing  $\hat{P}_1 \frac{1}{2} c^\dagger \sigma c \hat{P}_1 = \hat{T}$ , we get

$$\hat{P}_1 \hat{H}_{JB} \hat{P}_1 = J \sum_i \hat{T}_i \cdot \hat{S}_i - B \sum_i (\hat{T}_i^3 + \hat{S}_i^3). \quad (\text{A.10})$$

In the second term, the restriction to the  $\mathcal{F}_1$  subspace means that all additional charges must be created and annihilated in pairs. Therefore,

$$\begin{aligned} \hat{P}_1 \hat{H}_t^2 \hat{P}_1 &= \hat{P}_1 \sum_{ij} t_{ij} c_i^\dagger c_j \sum_{mn} t_{mn} c_m^\dagger c_n \hat{P}_1 \\ &= \hat{P}_1 \sum_{ij} |t_{ij}|^2 c_i^\dagger c_j c_j^\dagger c_i \hat{P}_1. \end{aligned} \quad (\text{A.11})$$

Employing the identity

$$2c_i^\dagger c_j c_j^\dagger c_i = \hat{n}_i(2 - \hat{n}_j) - c_i^\dagger \boldsymbol{\sigma} c_i \cdot c_j^\dagger \boldsymbol{\sigma} c_j \quad (i \neq j), \quad (\text{A.12})$$

we find that  $2\hat{P}_1 c_i^\dagger c_j c_j^\dagger c_i \hat{P}_1 = 1 - 4\hat{\mathbf{T}}_i \cdot \hat{\mathbf{T}}_j$  and hence

$$\begin{aligned} -\frac{1}{\Delta} \hat{P}_1 \hat{H}_t^2 \hat{P}_1 &= \frac{2}{\Delta} \sum_{ij} |t_{ij}|^2 \left( \hat{\mathbf{T}}_i \cdot \hat{\mathbf{T}}_j - \frac{1}{4} \right) \\ &= \frac{4t^2}{\Delta} \sum_{\langle ij \rangle} \hat{\mathbf{T}}_i \cdot \hat{\mathbf{T}}_j + \text{constant}. \end{aligned} \quad (\text{A.13})$$

In the last line above, we have taken advantage of the fact that  $t_{ij}$  connects only nearest neighbour sites.

Collecting these results and neglecting the remaining higher order terms in Eq. (A.9) yields

$$\hat{\mathcal{H}}^{\text{eff}} = \sum_i \left[ J \hat{\mathbf{T}}_i \cdot \hat{\mathbf{S}}_i - B(\hat{\mathbf{T}}_i^3 + \hat{\mathbf{S}}_i^3) \right] + J' \sum_{\langle ij \rangle} \hat{\mathbf{T}}_i \cdot \hat{\mathbf{T}}_j. \quad (\text{A.14})$$

Spins on neighbouring sites experience an antiferromagnetic exchange interaction of strength  $J' = 4t^2/\Delta > 0$ . In the atomic limit,

$$J' = \frac{4t^2}{\Delta} \sim \begin{cases} \frac{8t^2}{3J-2|B|} & \text{if } |B| < J, \\ \frac{8t^2}{2|B|-J} & \text{if } |B| > J. \end{cases} \quad (\text{A.15})$$

## A.2 Hubbard-Stratonovich Transformation

Suppose the Hamiltonian  $\hat{H} = \hat{H}_0 + \hat{H}_1$  can be broken into two- and four-fermion terms:

$$\begin{aligned} \hat{H}_0 &= \sum_{ij} \hat{\eta}_i^\dagger T_{ij} \hat{\eta}_j \\ \hat{H}_1 &= \frac{1}{2} \sum_{ii'jj'} \hat{\eta}_i^\dagger \hat{\eta}_j v_{ij;i'j'} \hat{\eta}_{i'}^\dagger \hat{\eta}_{j'}. \end{aligned} \quad (\text{A.16})$$

The purpose of the Hubbard-Stratonovich procedure is to find a purely bilinear (but field-dependent) Hamiltonian  $\hat{h}(\chi)$  such that the equality

$$e^{-\epsilon \hat{H}} = \int d\chi e^{-\epsilon \hat{h}(\chi)} \quad (\text{A.17})$$

is satisfied in the limit  $\epsilon \rightarrow 0$ . If  $\hat{h}(\chi)$  has the form given in Eq. (5.4), we can expand in powers of  $\epsilon$ :

$$e^{-\epsilon \hat{h}(\chi)} = e^{-\alpha \epsilon |\chi|^2} \left[ 1 - \epsilon \sum_{ij} \hat{\eta}_i^\dagger h(\chi)_{ij} \hat{\eta}_j - \frac{\epsilon^2}{2} \sum_{ii'jj'} \hat{\eta}_i^\dagger h(\chi)_{ij} \hat{\eta}_j \hat{\eta}_{i'}^\dagger h(\chi)_{i'j'} \hat{\eta}_{j'} + \dots \right]. \quad (\text{A.18})$$

We now integrate over the auxiliary fields and identify the right-hand side above with  $1 - \epsilon \hat{H}$ . Comparison with Eqs. (A.16) and (A.17) makes clear that we need to choose the coefficient matrix  $h(\chi)_{ij}$  such that

$$\begin{aligned} \int d\chi h(\chi)_{ij} e^{-\alpha \epsilon |\chi|^2} &= T_{ij} \\ \int d\chi \epsilon h(\chi)_{ij} h(\chi)_{i'j'} e^{-\alpha \epsilon |\chi|^2} &= v_{ij,i'j'}. \end{aligned} \quad (\text{A.19})$$

There is often some flexibility in the choice of the measure of integration.

$$\text{Real } \frac{1}{\sqrt{2\pi}} \int d\chi, \quad \text{complex } \frac{1}{2\pi i} \int d\chi' d\chi'', \quad \text{and finite } \frac{1}{2} \sum_{\chi=\pm 1} \quad (\text{A.20})$$

measures are commonly used. Note that the factor  $e^{-\alpha \epsilon |\chi|^2}$  in Eqs. (A.19) may not be necessary if the measure is compact.

### A.3 Coherent State Representation of Operators

As a basis of the fermion Hilbert space, the set of coherent states is overcomplete and non-orthonormal:  $\langle \eta | \eta' \rangle = e^{\bar{\eta} \eta'}$ . In this basis, the identity operator has the form

$$\hat{1} = \int d\bar{\eta} d\eta |\eta\rangle e^{-\bar{\eta} \eta} \langle \eta|. \quad (\text{A.21})$$

The usual procedure for casting an operator into the coherent state representation is to sandwich it between two representations of unity,  $\hat{O} = \hat{1} \hat{O} \hat{1}$ . The result is

$$\int d\bar{\eta} d\eta d\bar{\eta}' d\eta' |\eta\rangle e^{-\bar{\eta} \eta} O^+(\bar{\eta}, \eta') e^{-\bar{\eta}' \eta'} \langle \eta'|, \quad (\text{A.22})$$

where the matrix element  $O^+(\bar{\eta}, \eta') = \langle \eta | \hat{O} | \eta' \rangle$  is computed by normal-ordering the operator (via repeated application of the anticommutation relations) and then replacing creation and annihilation operators with Grassman variables:

$$O^+(\bar{\eta}, \eta') = N[\hat{O}] \Big|_{\hat{\eta}^\dagger \rightarrow \bar{\eta}, \hat{\eta} \rightarrow \eta'}. \quad (\text{A.23})$$

A somewhat more economical (but little-known) scheme is to insert a *single* representation of unity into the middle of the anti-normal-ordered

operator form. In that case,

$$\hat{O} = \int d\bar{\eta}d\eta |\eta\rangle e^{\eta\bar{\eta}} O^-(\eta, \bar{\eta}) \langle \eta|, \quad (\text{A.24})$$

where  $\hat{O}^-(\eta, \bar{\eta})$  is defined as in Eq. (A.23) but using the anti-normal-ordered form of the operator and the replacement  $\hat{\eta}^\dagger \rightarrow \bar{\eta}, \hat{\eta} \rightarrow \eta$ . Equation (A.24) requires half as many Grassman integrations as Eq. (A.22).

The most important operator for our purposes in the infinitesimal evolution operator. To find its coherent state representation, we recast it in the form

$$\begin{aligned} e^{-\epsilon\hat{h}} &= e^{-\epsilon(\alpha|\chi|^2 + \sum_{ij} h_{ij} \hat{\eta}_i^\dagger \hat{\eta}_j)} \\ &= e^{-\epsilon\mathcal{L}_0} e^{-\epsilon \sum_{ij} h_{ij} \hat{\eta}_j \hat{\eta}_i^\dagger}. \end{aligned} \quad (\text{A.25})$$

In the last line, we have defined  $\mathcal{L}_0 = \alpha|\chi|^2 + \text{tr } h$ . The Pauli exclusion principle ensures that the power series expansion of Eq. (A.25) is itself quadratic in the creation and annihilation operators:

$$e^{-\epsilon\hat{h}} = e^{-\epsilon\mathcal{L}_0} \left[ \hat{1} + \sum_{ij} (e^{\epsilon h} - \mathbb{1})_{ij} \hat{\eta}_j \hat{\eta}_i^\dagger \right]. \quad (\text{A.26})$$

Moreover, since the operator is expressed here in its anti-normal-ordered form, we can immediately write

$$\begin{aligned} e^{\sum_i \eta_i \bar{\eta}_i} (e^{-\epsilon\hat{h}})^-(\eta, \bar{\eta}) &= e^{-\epsilon\mathcal{L}_0} \left[ 1 + \sum_i \eta_i \bar{\eta}_i \right] \left[ 1 + \sum_{ij} (e^{\epsilon h} - 1)_{ij} \eta_j \bar{\eta}_i \right] \\ &= e^{-\epsilon\mathcal{L}_0} \left[ 1 + \sum_{ij} (e^{\epsilon h})_{ij} \eta_j \bar{\eta}_i \right] \\ &= e^{-\epsilon\mathcal{L}_0} \exp \sum_{ij} (e^{\epsilon h})_{ij} \eta_j \bar{\eta}_i. \end{aligned} \quad (\text{A.27})$$

Putting this result into Eq. (A.24) yields

$$e^{-\epsilon\hat{h}} = e^{-\epsilon\mathcal{L}_0} \int d\bar{\eta}d\eta |\eta\rangle e^{-\bar{\eta}(e^{\epsilon h})\eta} \langle \eta|. \quad (\text{A.28})$$

Having a coherent state representation of the infinitesimal evolution operator allows us to write

$$\begin{aligned} \langle \eta | (\hat{P} e^{\epsilon\hat{h}})^L | -\eta \rangle &\sim \int \prod_{l=1}^L d\bar{\eta}_l d\eta_l \langle \eta | \hat{P} | \eta_1 \rangle e^{-\bar{\eta}_1 (e^{\epsilon h}) \eta_1} \langle \eta_1 | \hat{P} | \eta_2 \rangle \times \dots \\ &\quad \times \langle \eta_{L-1} | \hat{P} | \eta_L \rangle e^{-\bar{\eta}_L (e^{\epsilon h}) \eta_L} \langle \eta_L | -\eta \rangle. \end{aligned} \quad (\text{A.29})$$

Here, we have introduced only  $L$  new Grassman variables. The traditional

way to evaluate an expectation value of this form is to insert  $2L - 1$  representations of unity between the  $2L$  operators:

$$\langle \eta | (\hat{P} e^{\epsilon \hat{h}})^L | - \eta \rangle = \langle \eta | \hat{P} \hat{1} e^{\epsilon \hat{h}} \hat{1} \hat{P} \hat{1} e^{\epsilon \hat{h}} \hat{1} \dots \hat{P} \hat{1} e^{\epsilon \hat{h}} | - \eta \rangle. \quad (\text{A.30})$$

According to Eq. (A.21), this leads to the (more cumbersome) expression

$$\int \prod_{l=1}^{2L-1} d\bar{\eta}_l d\eta_l \langle \eta | \hat{P} | \eta_1 \rangle e^{-\bar{\eta}_1 \eta_1} \langle \eta_1 | e^{\epsilon \hat{h}} | \eta_2 \rangle e^{-\bar{\eta}_2 \eta_2} \langle \eta_2 | \hat{P} | \eta_3 \rangle \times \dots \\ \times \langle \eta_{2L-2} | \hat{P} | \eta_{2L-1} \rangle e^{-\bar{\eta}_{2L-1} \eta_{2L-1}} \langle \eta_{2L-1} | e^{\epsilon \hat{h}} | - \eta \rangle. \quad (\text{A.31})$$

## A.4 Even-occupation Constraint Field

An arbitrary matrix  $U$  satisfies

$$e^{\bar{\eta} U \eta'} = \left( 1 + \bar{\eta} U \eta' + \frac{1}{2} (\bar{\eta} \eta')^2 \det U \right). \quad (\text{A.32})$$

The anticommuting nature of the Grassman variables eliminates all terms in the exponential expansion beyond second order. Restricting  $U \in \text{SU}(2)$  ensures that the first and last terms have the same (*i.e.*, unit) weight. The middle term is odd in  $U$  and can be eliminated by integration:

$$\int dU = 1 \quad \text{and} \quad \int dU U = 0. \quad (\text{A.33})$$

For example, we might choose the family of matrices  $U(\theta) = \begin{pmatrix} e^{i\theta} & 0 \\ 0 & e^{-i\theta} \end{pmatrix}$  so that

$$\int_0^{2\pi} \frac{d\theta}{2\pi} = 1 \quad \text{and} \quad \int_0^{2\pi} \frac{d\theta}{2\pi} \begin{pmatrix} e^{i\theta} & 0 \\ 0 & e^{-i\theta} \end{pmatrix} = 0. \quad (\text{A.34})$$

Such an integration amounts to filtering out the states with odd occupation:

$$\int dU e^{\bar{\eta} U \eta'} = 1 + \frac{1}{2} (\bar{\eta} \eta')^2 = 1 + \bar{\eta}_1 \bar{\eta}_2 \eta'_2 \eta'_1 = \langle \eta | \hat{P} | \eta' \rangle \quad (\text{A.35})$$

The operator

$$\hat{P} = |0\rangle \langle 0| + \hat{\eta}_1^\dagger \hat{\eta}_2^\dagger |0\rangle \langle 0| \hat{\eta}_2 \hat{\eta}_1 \quad (\text{A.36})$$

projects onto the space of even (*i.e.*, zero and double) occupancy.

## A.5 Continuous-time Limit of the Action

Recall that  $T_l = \exp(\epsilon h(\chi_l))$ . The constraint field also has an exponential representation  $U_l = \exp(-i\epsilon \lambda_l^\mu \Gamma^\mu)$  in terms of its generators  $\Gamma^\mu$ . Thus, in

the limit  $\epsilon \rightarrow 0$ ,

$$T_l \rightarrow 1 + \epsilon h(\chi_l) \quad \text{and} \quad U_l \rightarrow 1 - i\epsilon \lambda_l^\mu \Gamma^\mu. \quad (\text{A.37})$$

The discrete action becomes

$$\begin{aligned} S \rightarrow & \bar{\eta}_1 (1 + i\epsilon \lambda_1^\mu \Gamma^\mu) \eta_L - \sum_{l=2}^L \bar{\eta}_l (1 + i\epsilon \lambda_l^\mu \Gamma^\mu) \eta_{l-1} \\ & + \sum_{l=1}^L \left[ \epsilon \mathcal{L}_l^0 + \bar{\eta}_l (1 + \epsilon h(\chi_l)) \eta_l \right] \end{aligned} \quad (\text{A.38})$$

or, more suggestively,

$$\begin{aligned} S \rightarrow & \epsilon \bar{\eta}_1 \frac{\eta_1 + \eta_L}{\epsilon} + \sum_{l=2}^L \epsilon \bar{\eta}_l \frac{\eta_l - \eta_{l-1}}{\epsilon} + i\epsilon \lambda_1^\mu \bar{\eta}_1 \Gamma^\mu \eta_L \\ & - i\lambda_l^\mu \sum_{l=2}^L \epsilon \bar{\eta}_l \Gamma^\mu \eta_{l-1} + \sum_{l=1}^L \epsilon \mathcal{L}_l^0 + \sum_{l=1}^L \epsilon \bar{\eta}_l h(\chi_l) \eta_l. \end{aligned} \quad (\text{A.39})$$

In the continuum limit, the action takes the form of an imaginary time integral

$$S = \oint_{\eta(0)=-\eta(\beta)}^{\beta} d\tau \mathcal{L}(\tau) \quad (\text{A.40})$$

over the Lagrangian

$$\mathcal{L} = \mathcal{L}^0 + \bar{\eta}(\tau) \left[ \partial_\tau - i\lambda^\mu(\tau) \Gamma^\mu + h(\chi(\tau)) \right] \eta(\tau), \quad (\text{A.41})$$

which describes a set of noninteracting fermions coupled to a gauge field.

## A.6 Statistical Error and Discretization

In Eq. (6.11), we have used notational shorthand to gloss over two subtle issues. First, we have ignored the fact that the statistical errors between  $\bar{G}(\tau)$  and  $\bar{G}(\tau')$  are not independent for  $\tau \neq \tau'$ . In general, the errors will be positively correlated whenever  $|\tau - \tau'|$  is sufficiently small. There is also a tendency for them to be negatively (positively) correlated over long-separated times since  $G(0^-) = \mp G(\beta)$  is built in to the definition of the correlation function. Thus, one should more properly write the goodness-of-fit measure as

$$\chi^2[A] = \frac{1}{\beta^2} \int d\tau d\tau' \Delta(\tau) C^{-1}(\tau, \tau') \Delta(\tau'), \quad (\text{A.42})$$

where  $\Delta(\tau) = \int d\omega K(\tau, \omega)A(\omega) - \bar{G}(\tau)$  and  $C(\tau, \tau')$  is the covariance function for  $\bar{G}(\tau)$ .

Second, we have ignored the discrete nature of the known input data. A Quantum Monte Carlo algorithm, for example, is used to generate stochastically a sequence of independent measurements  $\{G^{(1)}, G^{(2)}, \dots, G^{(M)}\}$ , where each  $G^{(m)}$  is an  $(L+1)$ -vector holding the values of the single-particle propagator at imaginary times  $\tau_l = \beta l/L$  for  $l = 0, 1, \dots, L$ .

The numerical measurement of the Green's function is accomplished by taking the average

$$\begin{aligned}\bar{G}_l &= \frac{1}{M} \sum_{m=1}^M G_l^{(m)}. \\ \overline{G_l G_{l'}} &= \frac{1}{M} \sum_{m=1}^M G_l^{(m)} G_{l'}^{(m)}.\end{aligned}\tag{A.43}$$

The corresponding covariance matrix is given by

$$\begin{aligned}C_{ll'} &= \frac{1}{M(M-1)} \sum_{m=1}^M (G_l^{(m)} - \bar{G}_l)(G_{l'}^{(m)} - \bar{G}_{l'}). \\ &= \frac{1}{M-1} \sum_{m=1}^M \left[ \overline{G_l G_{l'}} - \bar{G}_l \bar{G}_{l'} \right]\end{aligned}\tag{A.44}$$

Equation (A.42) must now be discretized in order to make use of Eqs. (A.43) and (A.44). The imaginary time integrals are carried out numerically on a uniform mesh of  $L$  time slices (spaced by  $\Delta\tau = \beta/L$ ) according to the formula

$$\int_0^\beta d\tau f(\tau) \approx \sum_{l=0}^L \Delta\tau w_l f_l,\tag{A.45}$$

where  $f_l = f(\Delta\tau \cdot l)$  and the Bode's rule weights  $w_l$  satisfy  $\sum_{l=0}^L w_l = L$ . Equation (A.42) becomes

$$\chi^2 = \frac{1}{L^2} \sum_{l, l'=0}^L w_l \Delta_l C_{ll'}^{-1} w_{l'} \Delta_{l'}.\tag{A.46}$$

Since  $\Delta(0) = \pm\Delta(\beta)$ ,

$$\chi^2 = \frac{1}{L^2} \sum_{l, l'=0}^{L-1} \tilde{w}_l \Delta_l C_{ll'}^{-1} \tilde{w}_{l'} \Delta_{l'}.\tag{A.47}$$

Here,  $\tilde{w}_l = w_l + \delta_{l,0} w_L$  for  $l = 0, 1, \dots, L-1$ .

We now want to solve for the unitary transformation  $U$  that diagonalizes the covariance matrix. This allows us to write  $C = U^t \Sigma U$  in terms of a set

of *statistically independent* variances  $\Sigma = \text{diag}(\sigma_1^2, \sigma_2^2, \dots, \sigma_L^2)$ . The inverse matrix is  $C^{-1} = U^t \Sigma^{-1} U$ .

Putting  $C_{ll'}^{-1} = \sum_{k=0}^L \frac{1}{\sigma_k^2} U_{kl} U_{kl'}$  into Eq. (A.47) yields

$$\begin{aligned} \chi^2 &= \sum_{k=0}^L \frac{1}{\sigma_k^2} \left( \frac{1}{L} \sum_{l=0}^L U_{kl} w_l \Delta_l \right)^2 \\ &= \sum_{k=0}^L \frac{1}{\sigma_k^2} \left| (VK)[A]_k - (VG)_k \right|^2 \end{aligned} \quad (\text{A.48})$$

where we have defined the matrix  $V_{kl} = U_{kl} w_l / L$ .

To recapitulate, the discretization of the  $\tau$  integration is implicit in Eq. (6.11); it also presumes that we are working in the  $V$  basis in which the covariance matrix is diagonal.

## A.7 Maximum Entropy Formal Solution

We want to examine the changes in  $\mathcal{S}$  with variations in  $A(\omega)$ . Since the spectral function is subject to the normalization constraint  $\int d\omega A(\omega) = \mathcal{N}$ , variations in  $A(x)$  and  $A(y)$  for  $x \neq y$  are not independent. We can enforce the constraint by introducing a lagrange multiplier  $\Gamma = 1 + \alpha\mu$ . Let us define

$$\mathcal{S}[A, \Gamma] \equiv - \int d\omega A \ln(A/D) + \Gamma \int d\omega (A - D). \quad (\text{A.49})$$

We have assumed here that  $D(\omega)$  and  $A(\omega)$  have the same normalization.

Variations of the extended functional, Eq. (A.49), look like

$$\begin{aligned} \frac{\delta \mathcal{S}}{\delta A(x)} &= - \ln \left( \frac{A(x)}{D(x)} \right) + \alpha\mu \\ \frac{d\mathcal{S}}{d\mu} &= \alpha \int d\omega (A(\omega) - D(\omega)) \end{aligned} \quad (\text{A.50})$$

There is a unique solution that causes these two equations to vanish:  $A(x) = D(x)$ ,  $\mu = 0$ . This implies that  $\mathcal{S} = 0$  and  $\delta \mathcal{S} = 0$ .

Also, since

$$\frac{\delta^2 \mathcal{S}}{\delta A(x) \delta A(y)} = - \frac{\delta(x-y)}{A(x)} \quad (\text{A.51})$$

we find that  $\delta^2 \mathcal{S} \leq 0$ . This means that the entropy functional is strictly non-positive and takes its maximum  $\mathcal{S} = 0$  when  $A$  is equal to the default model.

Similar considerations for  $\chi^2[A]$  allow us to construct the total variation

in  $Q = \chi^2 - \alpha^{-1}\mathcal{S}$ . We find that

$$0 = \frac{\delta Q[A, \mu]}{\delta A(\omega)} = 2 \int_0^\beta d\tau K(\tau, x) \psi(\tau) - \alpha^{-1} \left[ -\ln \left( \frac{A(\omega)}{D(\omega)} \right) + \alpha \mu \right] \quad (\text{A.52})$$

where

$$\psi(\tau) = \int d\nu K(\tau, \nu) A(\nu) - \bar{G}(\tau). \quad (\text{A.53})$$

## A.8 Configurational Entropy

Consider a system of  $N$  energy levels with degeneracies  $m_p$  ( $p = 1, 2, \dots, N$ ). Suppose that each level is filled with  $n_p$  indistinguishable particles. The state of the system is unchanged by the rearrangement of particles within a given level. Thus, given a set of occupancies  $\{0 \leq n_p \leq m_p\}$ , the number of equivalent configurations is  $\Omega(\{n_p\}) = \prod_p \binom{m_p}{n_p}$  and the entropy due to this configuration is

$$\ln \Omega(\{n_p\}) = \frac{1}{N} \sum_p \ln \binom{m_p}{n_p}. \quad (\text{A.54})$$

The binomial coefficient  $\binom{m}{n} = m!/(m-n)!/n!$  can be approximated using Stirling's formula  $m! \approx m \ln m$ . In the limit of small relative occupancy, this gives

$$\ln \binom{m}{n} = m \ln m - (m-n) \ln(m-n) - n \ln n \quad (\text{A.55})$$

$\xrightarrow{m \gg n} -n \ln n.$

Going over to the continuum, we make the identification

$$\begin{aligned} \frac{1}{N} \sum_p &\rightarrow \int dx \\ m_p &\rightarrow \infty \\ n_p &\rightarrow n(x) \end{aligned} \quad (\text{A.56})$$

and use the counting arguments above to write the entropy associated with each field configuration:

$$\ln \Omega[n] = - \int_0^1 dx n(x) \ln n(x). \quad (\text{A.57})$$

The total entropy is

$$S = \int \mathcal{D}n \ln \Omega[n] \approx \ln \Omega[\bar{n}]. \quad (\text{A.58})$$

## A.9 Discretization over a Logarithmic Mesh

Suppose that we want to integrate a function  $f(\alpha)$  known only at the points  $\alpha_n = R^n \alpha_0$  for  $n = 0, 1, \dots, N$ . The integral identity

$$\int d\alpha f(\alpha) = \int d\tilde{\alpha} e^{\tilde{\alpha}} f(e^{\tilde{\alpha}}) \quad (\text{A.59})$$

follows from the change of variables  $\alpha = \exp(\tilde{\alpha})$ . In this basis, the known points describe a uniform mesh

$$\tilde{\alpha}_n = \ln \alpha_n = \ln \alpha_0 + n \ln R \quad (\text{A.60})$$

with spacing  $\Delta\tilde{\alpha} = \tilde{\alpha}_{n+1} - \tilde{\alpha}_n = \ln R$ . Accordingly,

$$\begin{aligned} \int d\alpha f(\alpha) &\approx \sum_{n=0}^N \Delta\tilde{\alpha} e^{\tilde{\alpha}_n} f(e^{\tilde{\alpha}_n}) \\ &= \sum_{n=0}^N (\ln R) \alpha_n f(\alpha_n). \end{aligned} \quad (\text{A.61})$$

When the integrand is of the form

$$\frac{dU}{d\alpha} = \frac{1}{e^{\tilde{\alpha}}} \frac{dU}{d\tilde{\alpha}} \quad (\text{A.62})$$

we must first discretize the derivative

$$\begin{aligned} \left. \frac{dU}{d\alpha} \right|_{\alpha=\alpha_n} &\approx \frac{1}{e^{\tilde{\alpha}_n}} \frac{U(\alpha_{n+1}) - U(\alpha_n)}{\Delta\tilde{\alpha}} \\ &= \frac{U(\alpha_{n+1}) - U(\alpha_n)}{\alpha_n \ln R}, \end{aligned} \quad (\text{A.63})$$

which leads to the integrals

$$\int_{\alpha_p}^{\alpha_{N-1}} d\alpha \left( -\frac{dU}{d\alpha} \right) \langle n(x) \rangle_\alpha \approx \sum_{n=p}^{N-1} [U(\alpha_n) - U(\alpha_{n+1})] \langle n(x) \rangle_{\alpha_n} \quad (\text{A.64})$$

and

$$\int_{\alpha_p}^{\alpha_{N-1}} d\alpha \left( -\frac{dU}{d\alpha} \right) \approx \sum_{n=p}^{N-1} [U(\alpha_n) - U(\alpha_{n+1})] \quad (\text{A.65})$$
$$= U(\alpha_p) - U(\alpha_N).$$

Equation (6.52) is simply the ratio of these two results.



# Bibliography

- [1] J. Kondo, *Prog. Theor. Phys.* **32**, 37 (1964).
- [2] P. W. Anderson, *Phys. Rev.* **164**, 352 (1967).
- [3] K. G. Wilson, *Rev. Mod. Phys.* **47**, 773 (1975).
- [4] N. Andrei, *Phys. Rev. Lett.* **87A**, 299 (1980).
- [5] P. B. Wiegman, *Sov. Phys. JETP Lett.* **31**, 392 (1980).
- [6] P. Nozières, *Ann. de Phys.* **10**, 19 (1985).
- [7] M. A. Ruderman and C. Kittel, *Phys. Rev.* **96**, 99 (1954).
- [8] T. Kasuya, *Prog. Theor. Phys.* **16**, 45 (1956).
- [9] K. Yosida, *Phys. Rev.* **106**, 893 (1957).
- [10] G. R. Stewart, *Rev. Mod. Phys.* **56**, 755 (1984).
- [11] M. Lavagna and C. Pepin, *Acta Phys. Pol. B* **29**, 3753 (1998).
- [12] P. W. Anderson, *Phys. Rev.* **124**, 41 (1961).
- [13] J. R. Schrieffer and P. A. Wolff, *Phys. Rev.* **149**, 491 (1966).
- [14] B. Bogenberger and H. V. Lohneysen, *Phys. Rev. Lett.* **74**, 1016 (1995).
- [15] M. Jaime, R. Mocshovich, G. R. Stewart, W. P. Beyermann, M. G. Berisso, M. F. Hundley, P. C. Canfield, and J. L. Sarrao, *Nature* **405**, 160 (2000).
- [16] G. S. Boebinger, A. Passner, P. C. Canfield, and Z. Fisk, *Physica B* **211**, 227 (1995).
- [17] K. S. D. Beach, P. A. Lee, and P. Monthoux, *Phys. Rev. Lett.* **92**, 026401 (2004).
- [18] P. Coleman, *Phys. Rev. B* **35**, 5072 (1987).
- [19] S. Doniach, *Physica B* **91**, 231 (1977).

- [20] S. Capponi and F. F. Assaad, Phys. Rev. B **63**, 155114 (2001).
- [21] G.-M. Zhang and L. Yu, Phys. Rev. B **62**, 76 (2000).
- [22] N. Metropolis, A. W. Rosenbluth, M. N. Rosenbluth, A. H. Teller, and E. Teller, J. Chem. Phys. **21**, 1087 (1953).
- [23] R. Blankenbecler, D. J. Scalapino, and R. L. Sugar, Phys. Rev. D **24**, 2278 (1981).
- [24] M. Jarrell and J. E. Gubernatis, Phys. Rep. **269**, 133 (1996).
- [25] A. W. Sandvik, Phys. Rev. B **57**, 10287 (1998).
- [26] W. von der Linden, Phys. Rep. **220**, 53 (1992).
- [27] D. M. Ceperley, Rev. Mod. Phys. **67**, 279 (1995).
- [28] R. M. Fye and D. J. Scalapino, Phys. Rev. B **44**, 7486 (1991).
- [29] J. E. Hirsch and R. M. Frye, Phys. Rev. Lett. **56**, 2521 (1986).
- [30] A. W. Sandvik and J. Kurkijärvi, Phys. Rev. B **43**, 5950 (1991).
- [31] N. V. Prokof'ev, B. V. Svistunov, and I. S. Tupitsyn, Phys. Lett. A **238**, 253 (1998).
- [32] M. Suzuki, Phys. Lett. A **146**, 319 (1991).
- [33] J. Hubbard, Phys. Rev. Lett. **3**, 77 (1959).
- [34] R. D. Stratonovich, Dokl. Akad. Nauk. SSR **115**, 1907 (1957).
- [35] R. Blankenbecler, D. J. Scalapino, and R. L. Sugar, Phys. Rev. D **24**, 2278 (1981).
- [36] D. J. Scalapino and R. L. Sugar, Phys. Rev. Lett. **46**, 519 (1981).
- [37] J. W. Negele and H. Orland, *Quantum Many-Particle Systems*, vol. 68 of *Frontiers in Physics* (Addison-Wesley, 1987).
- [38] K. Binder and D. W. Heermann, *Monte Carlo Simulation in Statistical Physics* (Springer-Verlag, 2002), 4th ed.
- [39] J. E. Hirsch, Phys. Rev. Lett. **28**, 4059 (1983).
- [40] J. E. Hirsch, Phys. Rev. Lett. **38**, 12023 (1988).
- [41] J. E. Hirsch and S. Tang, Phys. Rev. Lett. **62**, 591 (1989).
- [42] D. J. Scalapino, S. R. White, and S. C. Zhang, Phys. Rev. Lett. **68**, 2830 (1992).

- [43] D. J. Scalapino, S. R. White, and S. C. Zhang, *Phys. Rev. B* **47**, 7995 (1993).
- [44] R. M. Fye and J. E. Hirsch, *Phys. Rev. B* **38**, 433 (1988).
- [45] S. R. White, D. J. Scalapino, R. L. Sugar, N. E. Bickers, and R. T. Scalettar, *Phys. Rev. B* **39**, 839 (1989).
- [46] P. Monthoux, private communication.
- [47] S. F. Gull and J. Skilling, *IEE Proc.* **131**, 646 (1984).
- [48] R. N. Silver, D. S. Sivia, and J. E. Gubernatis, *Phys. Rev. B* **41**, 2380 (1990).
- [49] J. E. Gubernatis, M. Jarell, R. N. Silver, and D. S. Sivia, *Phys. Rev. B* **44**, 6011 (1991).
- [50] A. S. Mishchenko, N. V. Prokof'ev, A. Sakamoto, and B. V. Svistunov, *Phys. Rev. B* **62**, 6317 (2000).
- [51] K. S. D. Beach and R. J. Gooding, *Phys. Rev. B* **61**, 5147 (2000).
- [52] E. Marinari, cond-mat/9612010.
- [53] R. K. Bryan, *Eur. Biophys. J.* **18**, 165 (1990).